BRNO UNIVERSITY OF TECHNOLOGY

VYSOKÉ UČENÍ TECHNICKÉ V BRNĚ

FACULTY OF MECHANICAL ENGINEERING

FAKULTA STROJNÍHO INŽENÝRSTVÍ

INSTITUTE OF AEROSPACE ENGINEERING

LETECKÝ ÚSTAV

AERODYNAMIC ANALYSIS OF MORPHING GEOMETRY APPLICATION TO SAILPLANE WINGLET DESIGN

AERODYNAMICKÁ ANALÝZA MĚNITELNÉ GEOMETRIE WINGLETU PRO APLIKACI NA VÝKONNÉM KLUZÁKU

MASTER'S THESIS

DIPLOMOVÁ PRÁCE

AUTHOR — Bc. Matěj Malinowski

AUTOR PRÁCE

SUPERVISOR — Ing. Robert Popela, Ph.D.

VEDOUCÍ PRÁCE

BRNO 2017

BRNO UNIVERSITY OF TECHNOLOGY
FACULTY OF MECHANICAL ENGINEERING

Specification Master's Thesis

Department:	Institute of Aerospace Engineering
Student:	**Bc. Matěj Malinowski**
Study programme:	Mechanical Engineering
Study field:	Aircraft Design
Leader:	**Ing. Robert Popela, Ph.D.**
Academic year:	2016/17

Pursuant to Act no. 111/1998 concerning universities and the BUT study and examination rules, you have been assigned the following topic by the institute director Master's Thesis:

Aerodynamic analysis of morphing geometry application to sailplane winglet design

Concise characteristic of the task:

Space for aircraft performance improvements is getting smaller during last decades. Aircraft design concepts and design methods are matured and space for development is limited. One of modern viable possibilities for considerable improvement which is currently widely studied is geometry change of aircraft shape during flight – shape morphing. Winglet is typical devices designed for one particular flight regime with many disadvantages in other regimes. Hence the geometry morphing can bring new space for winglet design. The goal of proposed work is analysis of such a winglet influence on glider performance increase, analysis and selection of key design parameters, design of baseline geometry and proposal for shape change dependence on flight regime.

Goals Master's Thesis:

Aerodynamic analysis of possible improvement in glider performance by winglet in–flight geometry change. Analysis of requirements for winglet geometry changes based on different flight regimes. Identification of main geometrical characteristics and performance improvement.

Recommended bibliography:

THOMAS, F., MILGRAM, J., Fundamentals of Sailplane Design, College Park Press, 1999, ISBN 978-0966955309.

IHS ESDU 98013 Aerodynamic principles of winglets, 2003, ISBN 978 1 86246 050 8.

Deadline for submission Master's Thesis is given by the Schedule of the Academic year 2016/17

In Brno,

L. S.

doc. Ing. Jaroslav Juračka, Ph.D. Director of the Institute	doc. Ing. Jaroslav Katolický, Ph.D. FME dean

ABSTRACT

This master's thesis deals with aerodynamic analysis and optimisation of sailplane winglet. Winglet is considered with ability of in-flight shape changing and optimisation process is focused to revealing of optimal shapes for different flight regimes. First part of thesis describes current efforts in the field of design and development of winglets with variable geometry. Second part is focused on the description of winglet function, followed by third part which describing optimisation methods, which may be used for the winglet optimisation. Description of the aircraft fitted with winglet chosen for the optimisation process is next part of thesis followed by airworthiness requirements for the category of chosen aircraft. Model of typical flight of this aircraft is next part. Rest of the thesis is organized according to the process of searching optimum winglet shapes. Wing and winglet parametric CAD model description is followed by CFD model creation process and CFD simulation pre-processing description. Optimisation process details are revealed in the penultimate chapter. The final part of the thesis contains evaluation of the optimisation process results.

KEY WORDS

Winglet, optimisation, CFD, Computational Fluid Dynamics, adaptive, morphing, sailplane, glider, design, analysis, performance

ABSTRAKT

Diplomová práce se zabývá aerodynamickou analýzou a optimalizací wingletu kluzáku. Winglet je uvažován s možností změny tvaru v průběhu letu a optimalizační proces je zaměřen na odhalení optimálních tvarů v odlišných letových režimech. První část práce popisuje současné snahy v oblasti návrhu a vývoje wingletů s měnitelnou geometrií. Druhá část je zaměřena na popis funkce wingletu, následována třetí částí, která popisuje optimalizační metody, které mohou být použity během optimalizace. Další částí práce je popis letadla vybaveného wingletem, který byl vybrán pro optimalizaci. Tato část je následována požadavky stavebního předpisu kategorie letadla, které bylo vybráno. Následuje model typického letu tohoto letadla. Zbytek práce je organizován dle procesu hledání optimálních tvarů wingletu. Popis tvorby CAD modelu je následován popisem tvorby CFD modelu a popisem přípravy CDF simulací. V předposlední kapitole jsou odhaleny detaily optimalizačního procesu. Závěrečná část práce obsahuje vyhodnocení výsledků optimalizačního procesu.

KLÍČOVÁ SLOVA

winglet, optimalizace, CFD, Computational Fluid Dynamics, adaptivní, kluzák, návrh, analýza, výkon

BIBLIOGRAPHIC CITATION

MALINOWSKI, M. *Aerodynamic analysis of morphing geometry application to sailplane winglet design.* Brno: Brno University of Technology, Faculty of Mechanical Engineering, 2017. 119 p. Supervised by Ing. Robert Popela, Ph.D.

STATEMENT OF AUTHENTICITY

I, Matěj Malinowski, hereby declare that I worked out this master's thesis independently under the supervision of this master's thesis supervisor Ing. Robert Popela PhD. I also hereby declare that all professional literature and other information sources, which were used during the creation of this thesis are properly cited and listed in the bibliography.

In Brno:_____ Author's signature:_____

ACKNOWLEDGMENT

At this point, I would like to thank my master's thesis supervisor Ing. Robert Popela, Ph.D. for all valuable advices during work on this thesis. I would like to thank him also for opportunity to increase my experience in the field of computational fluid dynamics and for deepening of my knowledge of optimization processes. I would also like to thank to Ing. Lukáš Popelka, Ph.D for advices in the field of optimisation process.

CONTENTS

1 INTRODUCTION

This masters's thesis describes the process of the morphing winglet geometry optimisation for different flight conditions. Aircraft chosen for the study is high performance sailplane Ventus 2ax. Flight conditions which undergoes the investigation are specified as low speed horizontal flight at speed of 85 km/h with wing flap in positive deflection position +2 and high speed horizontal flight at speed of 210 km/s with flap in negative deflection position -2.

The goal of thesis is to find possible advantages of the morphing winglet aerodynamic performance over the fixed geometry winglet. Main pitfall of the fixed geometry winglets is that geometry is result of multicriterial and multiregime optimization that leads to compromises in the winglet performance in extreme conditions. High speed and low speed flight could be understood as these extreme conditions. The morphing geometry winglet has potential to improve aerodynamic performance of sailplane in the above-mentioned flight regimes.

2 CURRENT STATE OF KNOWLEDGE

Up to date, many investigations was made in the field of morphing aircraft structures as well as in the field of variable geometry winglets. Main factors which decelerates the progress in above mentioned fields are the conservativeness in the certification processes in aviation industry as well as the advanced materials research. However, winglets are ideal for the first morphing structures application mainly because of its abilities from improving performance of sport aircrafts like gliders up to lower the fuel consumption and improving climb performance of large airliners. Above mentioned aspects made the morphing winglet very interesting from the design companies and their customers point of view.

2.1 Activities in the field of morphing winglets technology

There were very intensive investigations in the fields of aircraft aerodynamic performance and wing loads active control by usage of active winglets in many embodiments within recent years.

As very good example, the part of SARISTU (Smart Intelligent Aircraft Structures) program focused on adaptive winglet could be mentioned. In this particular case, winglet could be described as classic fixed geometry winglet fitted with flap and elastic elements/element placed between flap and fixed part of winglet. Despite this embodiment of active winglet contain simple flap without smooth transitioning surfaces, its fitting to the aircraft wing could result in reduction of fuel consumption 2,5% higher than in the case of classic fixed winglet. [17]

Further drag reduction is result of the winglet capability of geometry changing and thus thrust optimisation under its breaking point.

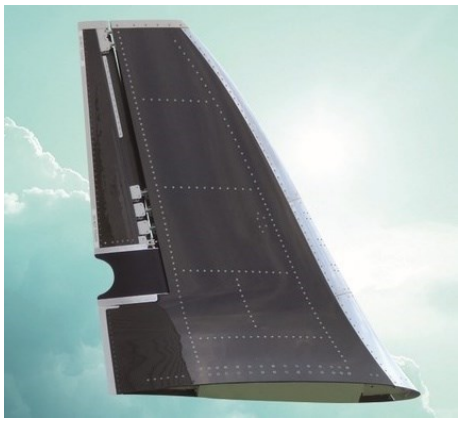

Fig. 2.1 FACC Active Morphing Winglet [17]

2.2 Patent search

Up to date, many patent applications were received and approved. Most of them relates to the civilian airliners and business jets field, but basic principles would be adapted to small aircrafts like gliders and single engine sport and touristic aircrafts.

Few of the most important patents will be mentioned below to describe possible principles of in-flight changes of winglet geometry.

The Boeing Company is holder of the patent US 7,744,038 B2 -Controlabe Winglets. This patent describes controllable winglets, which uses Shape Memory Alloys (further described as SMA) in their construction. This kind of actively controllable winglets would be fitted to newly designed aircraft as well as aircrafts already in use. Winglets would be used for aerodynamic optimization as well as for load alleviation when higher G-loads are expected. For example, in case of transit through wind gust. This load alleviation could lead to the lower structural loads and thus to the lighter airframe structure weight, which could result to lower fuel burn, or in higher aircraft transport capacity.

SMA elements used in structure of winglet has prescribed shape – thermal dependency, which lead to the winglet shape transition when SMA elements are heated or cooled. SMA elements could be used for example in tubular form and could be placed in the winglet to wing junction, which may be made of superelastic material. This embodiment would lead to the capability of changing winglet cant angle. Resulting motion could be seen in the figure 2.2. Another possibility of winglet shape change by use of SMA could be change of toe-in and twist. Motion like that could be achieved by usage of SMA torsion tubes. Torsion motion could be seen in the figure 2.2.

Next example of shape adaptive winglet is European Patent Application EP 2 233 395 A1 – Winglet with autonomously actuated tab. This patent application, which belongs to EADS Deutchland GmbH and Airbus Operations Limited, describes another possible embodiment of winglet capable of shape change. In this particular embodiment, the winglet adapts to the actual state of flow autonomously and independently of the aircraft flight control system. This is highly desirable, as retrofit of winglet, which has connection to existing flight control system of aircraft will lead to the requirement of flight control system recertification. Because of the possible costs of doing so, better solution is above mentioned autonomous winglet control system.

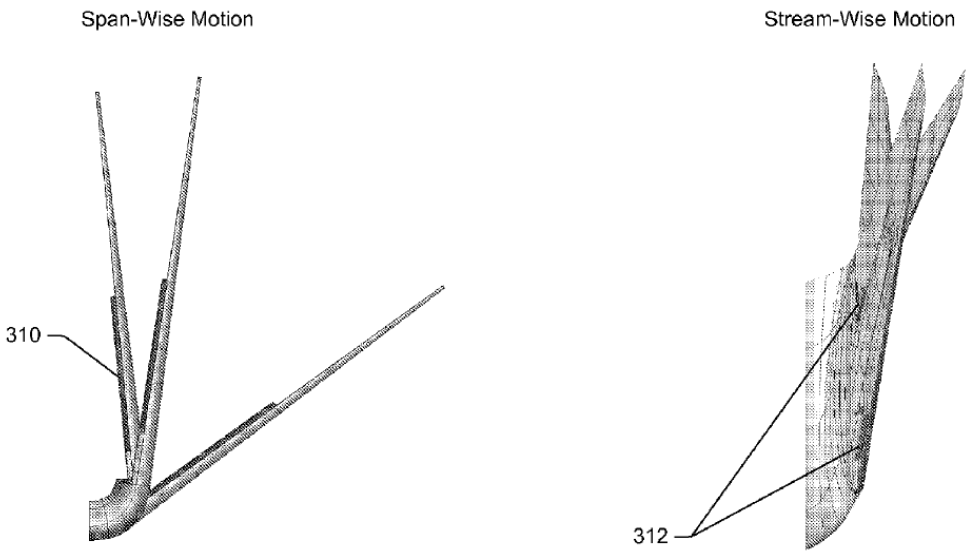

Fig. 2.2 Shape Memory Alloy Controllable Winglet [22]

Principle of Winglet with autonomously actuated tab lays in the employment of pressure sensing units placed on the surface of winglet (upper and lower). Pressure sensing units sends information about pressures on surfaces of the winglet to the winglet control system. When pressure difference between lower and upper winglet surface reaches some predefined value, winglet control system sends signal to the actuators, which deflects flap(s) at the trailing edge of the winglet. Basic principle description above is well supplemented by figure 2.3.

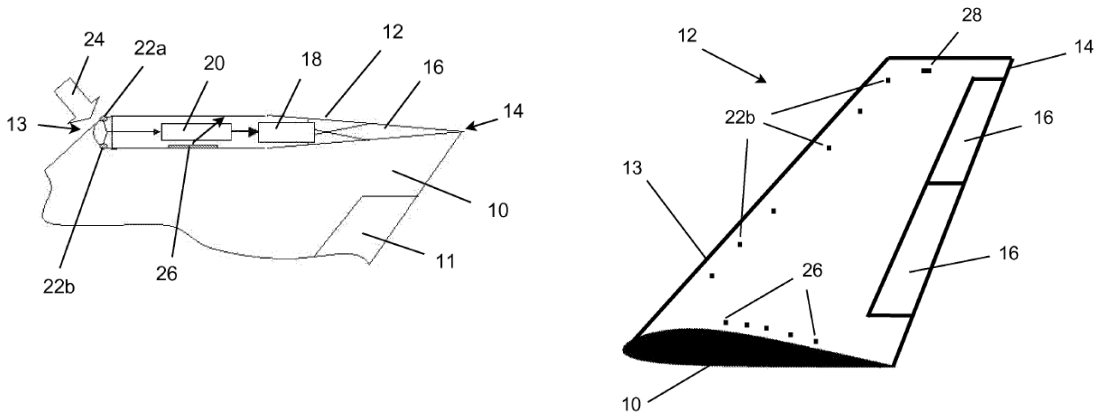

Fig. 2.3 Winglet with autonomously actuated tab [16]

Another possible solution to the problems of fixed geometry winglet is mentioned in European Patent Application EP 2 881 322 A1 – Adjustable lift modification wingtip of Tamarack Aerospace Group, Inc. This solution goes further than just to the modification of winglet itself, but rather also incorporates horizontal parts, which follow the shape of the wing. Horizontal part incorporates control surfaces that could be described as similar to the ailerons. These surfaces allow further modification of the flow and optimization of lift distribution to achieve better aerodynamic performance of winglet, or load alleviation when situation requires. Same company also owns United States Patent US 7,900,877 B1 – Active winglet. Principle of function is very similar to that of Adjustable lift modification wingtip. Major difference lies in fact that Active winglet doesn't changes toe-in angle but rather uses flap at its vertical portion. The principle of Adjustable lift modification wingtip and Active winglet is best described by figure 2.3 on the next page.

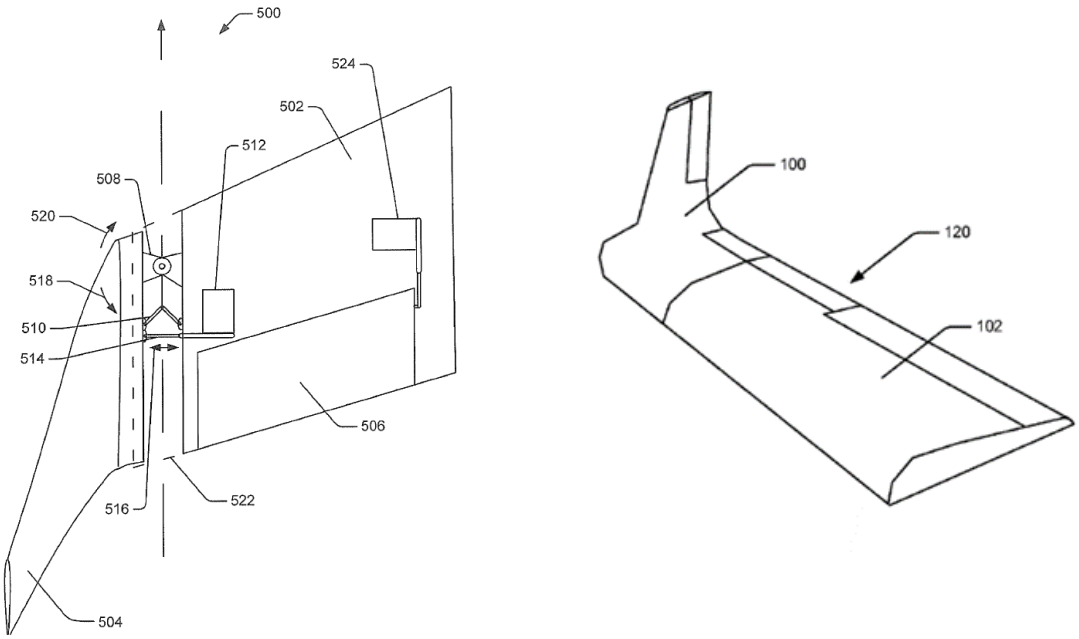

Fig. 2.4 Adjustable lift modification wingtip (left) and Active winglet (right) [15]

3 DESCRIPTION OF WINGLET FUNCTION

Winglet is nonplanar aerodynamic modification of aircraft wing and could be described as usually upwards pointing aerodynamic surface localized at the tip of the aircraft wing. Its main function is improvement of the aircraft performance by reducing drag force. Winglet function is strongly dependent on its geometry and wing lift distribution.

3.1 Winglet geometry definition

There is various shape of nowadays winglets, but trapezoidal shape was chosen for the basic description of the winglet geometry. Description of essential winglet geometry parameters is presented in the table 3.1.

Name	Designation	Unit
Winglet span	l_w	mm
Winglet height	h_w	mm
Wing tip chord	c_t	mm
Winglet root chord	c_{wr}	mm
Winglet tip chord	c_{wt}	mm
Cant angle	Φ	°
Toe-in angle	γ_{wr}	°
Winglet twist	γ_{wlt}	°
Tip-in angle	$\gamma_{wt} = \gamma_{wr} + \gamma_{wlt}$	°
Sweep angle (at T.E.)	Λ_{TE}	°

Tab. 3.1 Designation of winglet geometry parameters

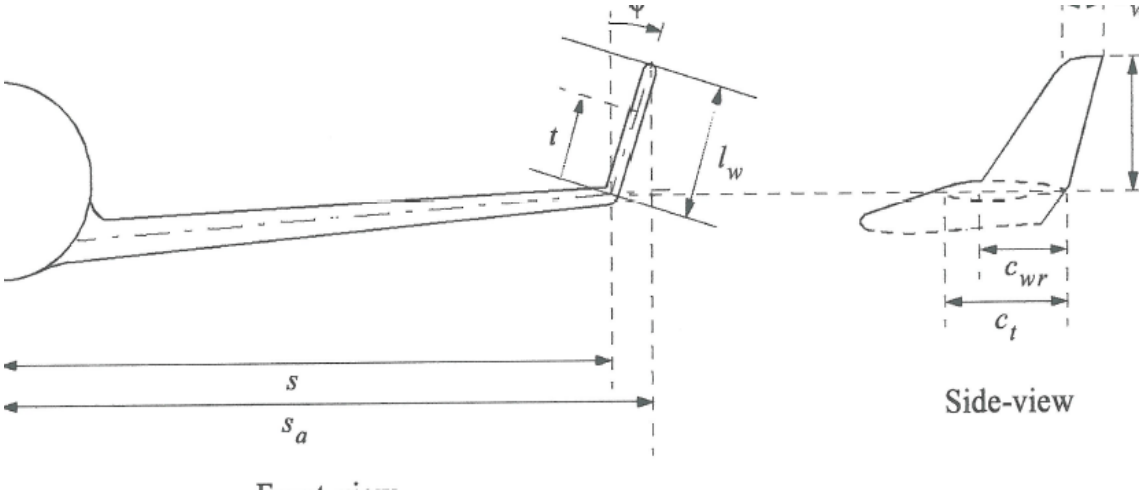

Fig. 3.1 Graphic description of winglet geometry [2]

Essential winglet geometry parameters are winglet cant angle, toe-in angle and winglet twist or tip-in angle respectively. Toe-in angle is negative when winglet root airfoil leading edge point lays on higher wingspan than trailing edge point. Same statement applies to the tip-in angle. Another important geometry parameter is winglet sweep angle, which is usually expressed in form of trailing edge sweep angle measured from vertical plane. Above mentioned geometry parameters is described in figure 3.2.

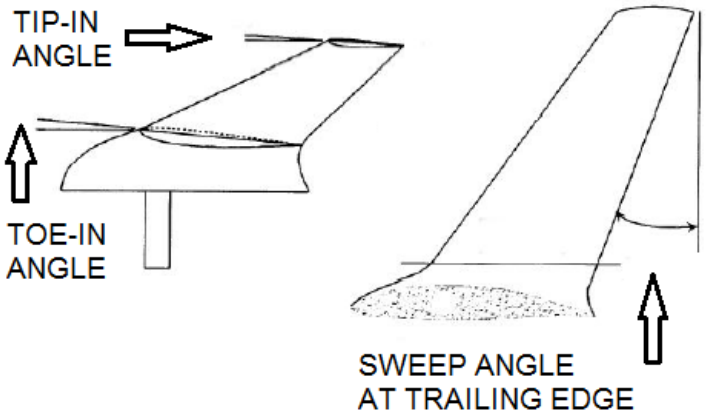

Fig. 3.2 Description of winglet toe-in, tip-in and sweep angle. [6]

3.2 Winglet function principle

Winglet, as device intended for aircraft drag reduction, uses secondary flow of the wing to generate additional forces. Well-designed winglet is able to generates negative drag force (i.e. thrust). During the flight with positive lift force, it can be seen, that air on the wing lower surface doesn't flow only in chord-wise direction, but also in the span-wise direction. Span-wise direction of the flow at the bottom side of the wing is in the root to tip direction. Opposite to that, on the wing upper surface, tip to root span wise flow could be observed. This flow is the direct consequence of the pressure distribution around the wing. As the lift force is result of different static pressure on the wing upper and lower surfaces, static pressure on the wing lower surface is higher than that on the upper surface. In the case of wing with infinite span, there is no other way how the pressure on the lower and upper surface could equalize, than far after the trailing edge. In case of finite span wing, situation is different. Pressure field at the vicinity of

the wing tip tends to equalize the pressure difference between lower and upper wing surface. This effect leads to above mentioned span wise motion of the air and finally to forming of the wing-tip vortices. Wing-tip vortex has velocity profile which is described in figure 3.3. Air flow on different span stations of the winglet has different direction. This leads to the effort of choosing right twist values along the winglet span for achieving maximum performance by optimal flow around airfoils along the winglet.

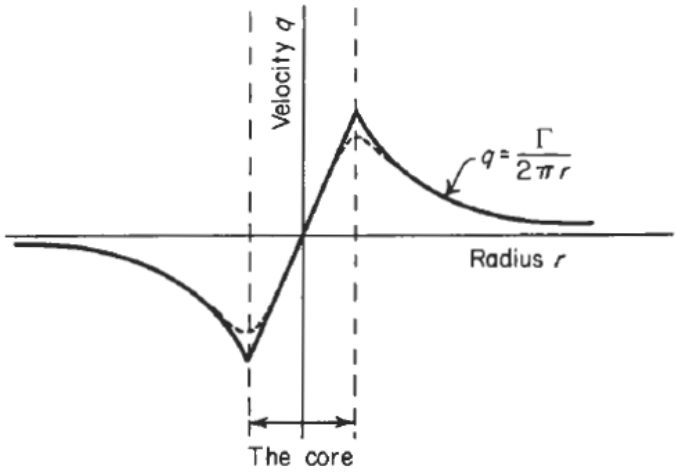

Fig. 3.3 Wingtip vortex velocity profile [3]

Winglets uses wing tip flow to generate lift and drag force. In case when winglet lift force component in the fight direction is higher than drag force component against the flight direction, net force in longitudinal direction points forward in the flight direction and thus, winglet is generating thrust force. Simple explanation of thrust force generation is evident from figure 3.4.

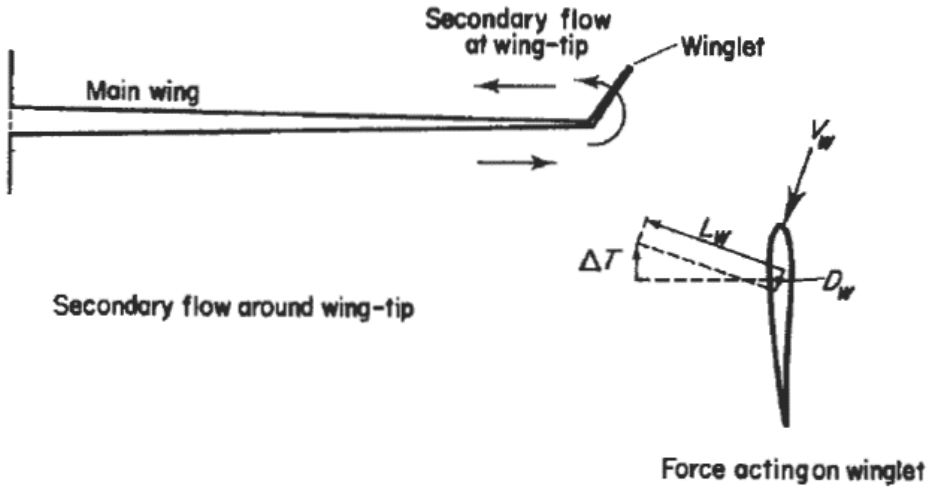

Fig. 3.4 Wing secondary flow and forces acting on winglet [3]

However, this is only one aspect of the winglet function. Unfortunately, lift and drag force of the winglet has also span wise components which are pointing in the wing tip to wing root direction. These forces are not negligible and causes additional bending load of the wing structure. Thrust force of winglet itself causes additional torsional load of the wing structure. These additional loads lead to the higher mass of wing structure.

By above mentioned principle, winglet reduces the induced drag of the aircraft wing and reduces intensity of wing tip vortices. However, winglet function is strongly dependent on the

wing tendency to generate span-wise flows. This tendency is proportional to the actual lift coefficient of the wing. It is apparent that winglet will generate highest thrust force when the lift coefficient of the wing is high. This situation corresponds to the low speed flight in case of sailplanes, to the climb condition and high-altitude cruise condition in case of business jets and airliners and finally to the relatively high portion of flight of the agricultural aircrafts. At higher speeds, winglet thrust will decrease due to the decrease of the local angles of attack along the winglet span and winglet skin friction drag will equal to the winglet thrust generated by pressure distribution along the winglet. Further increase of the speed and decrease of the local angles of attack will lead to situation when winglet generates additional drag force to the aircraft. This phenomenon is well described in figure 3.5.

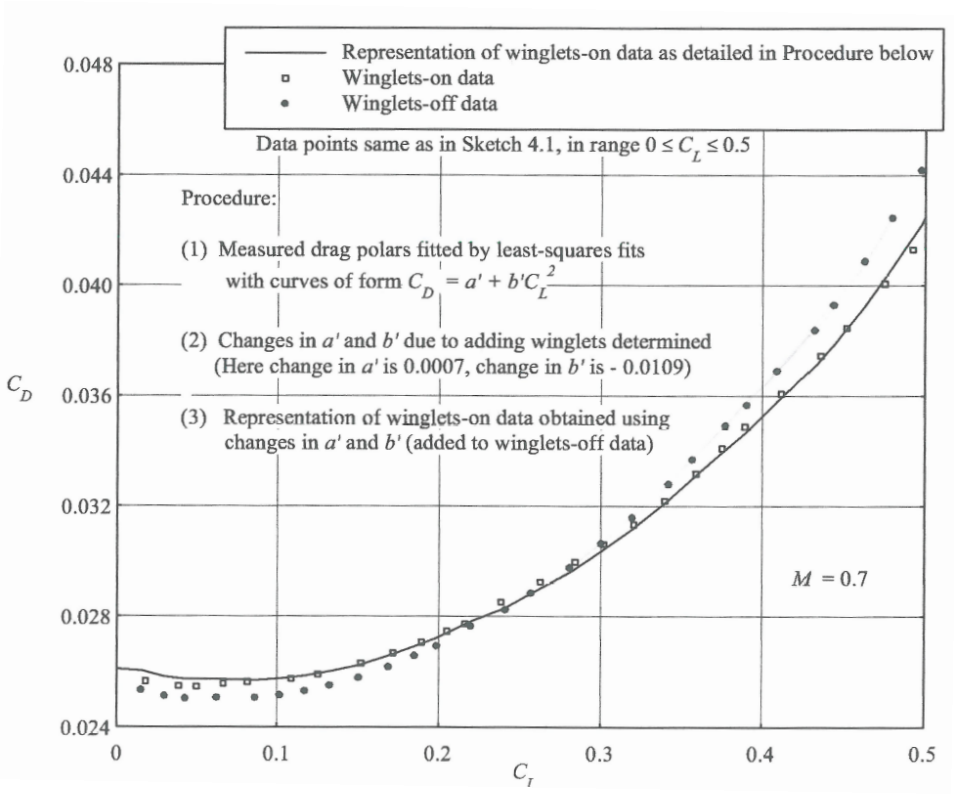

Fig. 3.5 Comparison of aircraft drag polar with and without winglets [2]

Point at which the contribution of winglet to the aircraft overall drag is equal to zero is often called the breaking point. There is effort to obtain braking point at speeds as high as possible. This means, that winglet should generate thrust even at relatively low lift coefficients of the wing. This could be achieved by changing of the winglet twist and toe-in angle during the flight. Example of comparison of two different winglets breaking points is mentioned in figure 3.6.

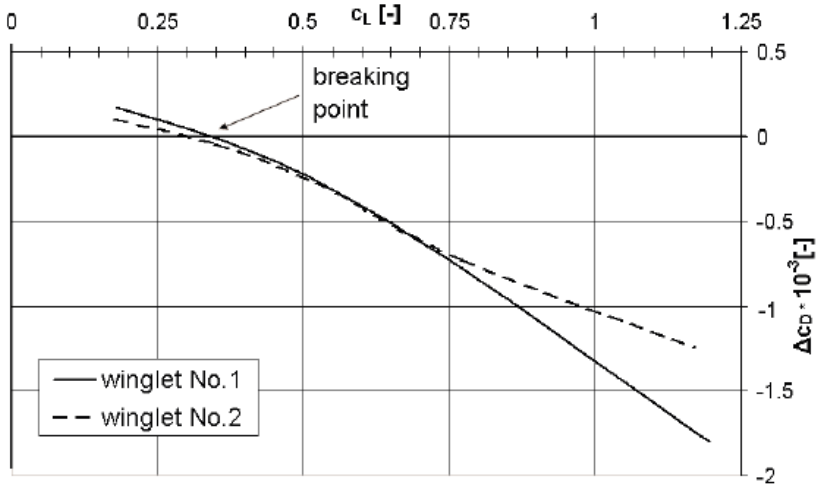

Fig. 3.6 Comparison of two different winglets breaking points [6]

3.3 Influence of winglet geometry on performance

Some of geometrical parameters of winglet have major influence on the winglet performance and thus on reduction of trailing vortex drag of the wing. Winglet cant angle and ratio of winglet span to the wing semi-span without winglet can be considered as the significant design parameters. Next parameters in the term of importance are the tip-in and winglet twist along its span. Influence of the winglet span l_w to semi-span of wing without winglet s and cant angle influence is apparent from figure 3.7 and 3.8 respectively. Parameter D_{TV}/D_{ob} is ratio of trailing vortex drag of wing with winglet to the trailing vortex drag of elliptically loaded wing without tip extension or winglet.

Trailing vortex drag of elliptically loaded wing with span b or semi-span s corresponding to wing without wing extension or winglet could be expressed by equation 3.1. Semi-span s is shown in figure 3.1.

$$D_{ob} = \frac{L^2}{\pi q b^2} = \frac{L^2}{4\pi q s^2} \tag{3.1}$$

Trailing vortex drag of elliptically loaded wing with span b_a or semi-span s_a corresponding to wing with wing extension or winglet could be expressed by equation 3.2. Semi-span s_a is shown in figure 3.1.

$$D_{oa} = \frac{L^2}{\pi q {b_a}^2} = \frac{L^2}{4\pi q {s_a}^2} \tag{3.2}$$

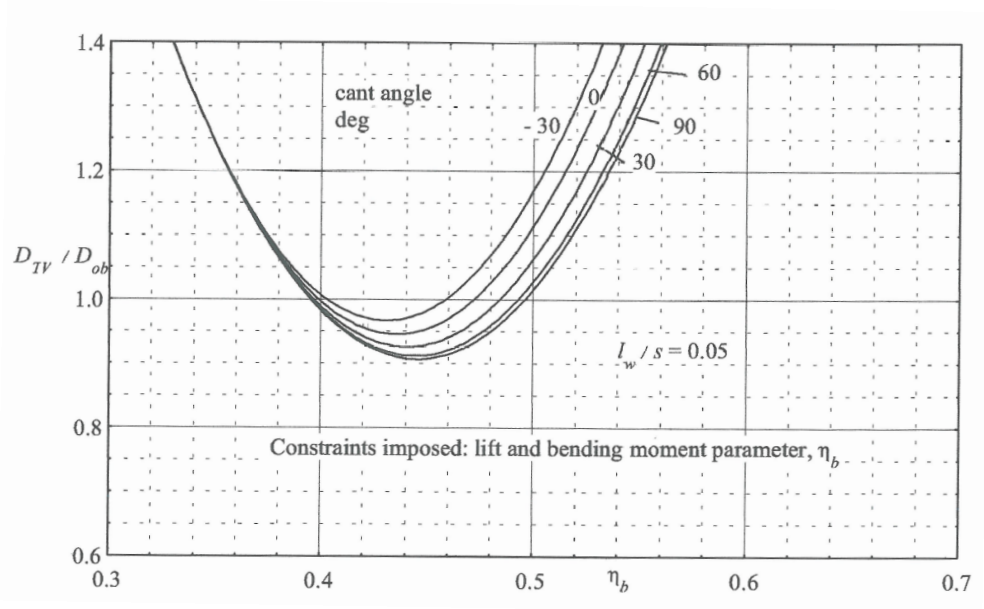

Fig. 3.7 Influence of winglet span and cant angle on trailing vortex drag ($l_w/s = 0.05$) [2]

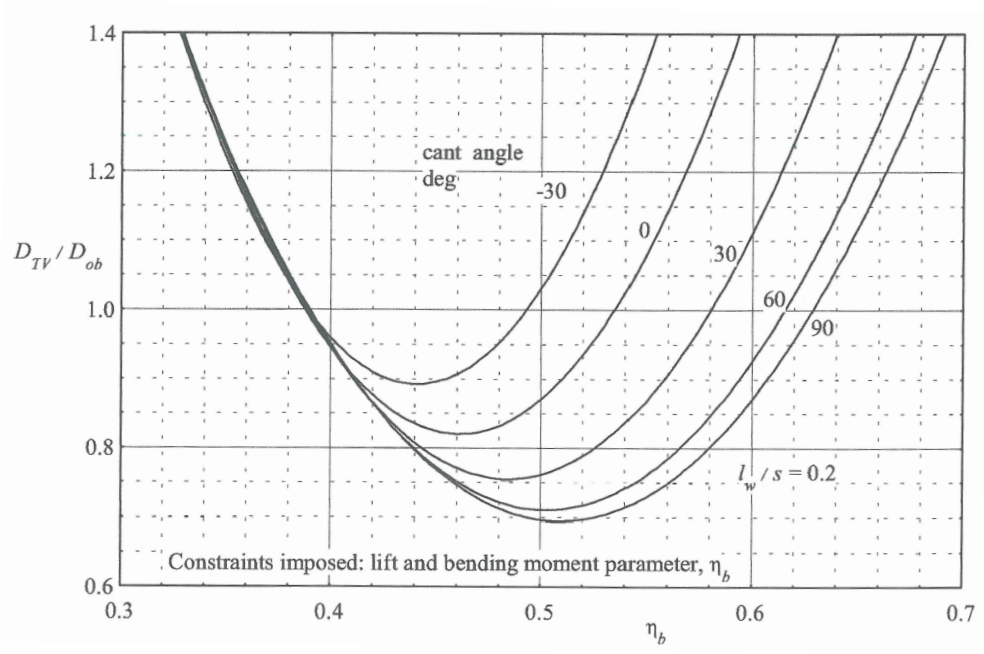

Fig. 3.8 Influence of winglet span and cant angle on trailing vortex drag (lw/s = 0.2) [2]

Parameter η_b corresponding to the non-dimensional bending moment arm and can be defined by equation 3.3.

$$\eta_b = \frac{y_b}{s} \tag{3.3}$$

Where y_b is effective bending moment arm defined by equation 3.4.

$$y_b = \frac{2M_r}{L} \tag{3.4}$$

Where M_r is wing bending moment measured in the plane of symmetry and L is wing lift force.

It is apparent, that for unconstrained wingspan case minimum trailing vortex drag can be obtained for cant angle of 90 degrees, which is in fact wing extension. This minimum trailing vortex drag is obtained at higher non-dimensional bending moment arm. However in case of constrained wingspan, simple consideration should be made, that increasing of cant angle for constrained span b_a will lead to the increasing of the winglet length if position of the winglet root station is not fixed (i.e. l_w/s increasing), which applies to ab initio designs. In case of fixed winglet root position in the span-wise direction of the wing, cant angle decrease leads to the increase of the winglet length and opposite. Variation of D_{TV}/D_{oa} for different cant angles and ratio of structural wingspan b_s to aerodynamic wingspan b_a could be seen in figure 3.9.

Structural wingspan could be expressed as mentioned in equation 3.5.

$$b_s = b + 2l_w \tag{3.5}$$

Trailing vortex drag D_{oa} is drag of wing without tip extension or winglets and span b_a in case when it has elliptic lift distribution.

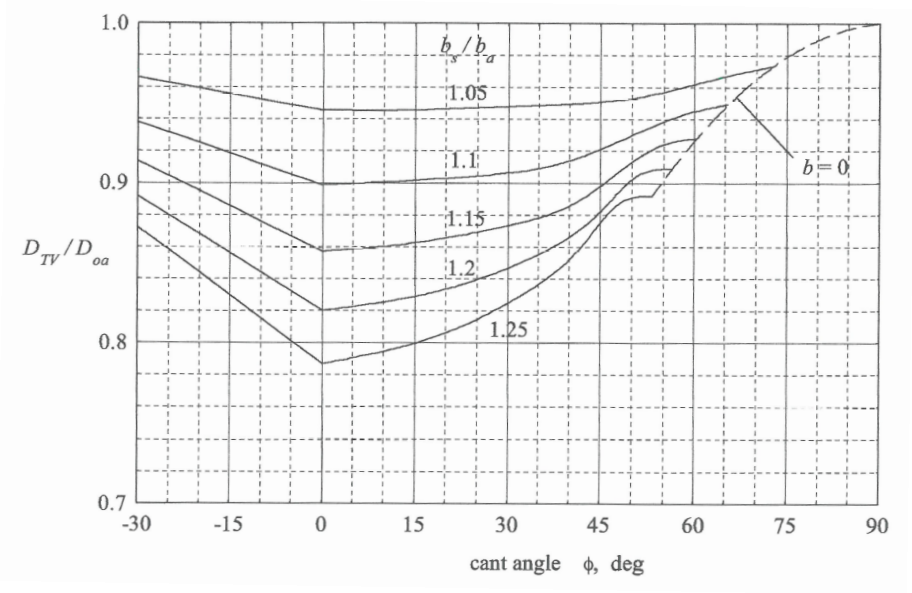

Fig. 3.9 Influence of b_s/b_a ratio and ϕ to D_{TV}/D_{oa} ratio [2]

Influence of the tip-in angle and winglet twist is strongly dependent on the winglet airfoil selection and other aspects as actual operating point of wing corresponding to actual lift coefficient and is hard to easily express as it is in the case of above mentioned winglet span and cant angle influence.

4 OPTIMIZATION METHOD

As the objective of this master's thesis is optimization of the winglet shape for two significant flight regimes, first step is right choice of optimization method to be implemented into process.

4.1 Considered optimization methods

In case of isolated wing optimisation, optimization is often performed using genetic algorithm method, variation principles including sensitivity analysis and optimal control theory and finally also response surface method (RSM).

In this optimization case, the genetic algorithm and RSM methods were considered.

- **Genetic algorithm:**

Genetic algorithm method is part of so-called evolutionary methods. These methods are based on stochastic approach. Design which should be optimised is under constrained and some of the design parameters values are randomly changed during process. Main advantage of these methods is, that they naturally supress the tendency to focus on small area of parameters values. Thus, wide area could be explored and optimum which could be overlooked when other methods are used, may be found. Genetic algorithms imitate process of natural selection, which is successful in adapting living organism to their environment. [4]

Genetic algorithms are based on models of Darwinian evolution, that is, survival of the fittest. Basic idea is that firstly the initial population is built and analysed. After this step, the former population is used to build new generation by combining ideas from multiple (usually two) parents in the population. This procedure provides mechanism for exploring search space and improving designs generation by generation. There are various ways of selection of the fittest and of the choice of parents for generation of their descendants which should be better than parents. As the choice of parents are random, there must be implemented some apparatus to improve the chance of the selection of the parents with highest fitness to increase the probability of better new generation creation. [4]

In summary, in terms of genetic algorithm methods. Advantage of the method is wide exploration of deign space. Main disadvantage is high computational resources requirement as each evolution of design is based on evaluation of predeceasing generation of designs.

- **Response surface method:**

Response surface method is more straightforward. Method algorithm is well described by figure 4.1.

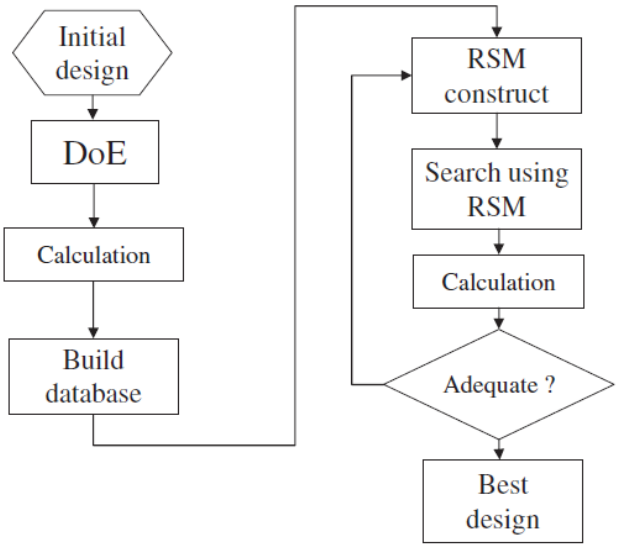

Fig. 4.1 Response surface method optimization algorithm [4]

RSM optimisation process is divided into few key steps. First, the initial design must be known, which can be also described as neutral design or reference design. Next step is Design of Experiments (DoE). In this phase of process, variants of design with adjusted parameters of interest is created. Parameters adjustment isn´t arbitrary. There are ways how to systematically determine parameters values. This phase of process will be described later in this thesis. After necessary design variants are determined, calculation of all design variants characteristics follows. Under the term calculation, also simulation or experiment could be imagined. This calculations or simulations lead to the build of database with characteristics of each design variant. This database is than used together with cost function(s) for creation of response surface. Depending on the form of cost function(s), the maximum or the minimum value of response surface function is then determined. Finally, after encoding of the coded variables used in response surface function, the natural variables are obtained, which determines the optimal, or near optimal design. Coded variables are used during DoE. Coding and decoding of natural variables for DoE and RSM will be described later in the text. Optimal design is then verified by another calculation, simulation or experiment and in case, that target criteria was met, for example in the manner of improvement of performance, then the design is finally considered as optimal.

RSM optimization requires less computational resources in comparison to the genetic algorithm method, which could be considered as advantage of the method. Main disadvantage of method is relatively narrow explored design space in comparison to the genetic algorithm method. This disadvantage could be to some extend eliminated by addition of next design variants, in other words by extending natural variables range. Possibility of extending explored design space step by step is great advantage of this method.

- **Optimisation method choice:**

Initial design of the wing and winglet of Ventus 2ax sailplane is already known and number of parameters intended for winglet geometry optimisation is not high. This together with less computational requirements and possibility of extending explored design space by extending natural variables range leads to the choice of RSM as optimization method for the case of Ventus 2ax winglet shape optimisation for low and high speed flight.

5 DESCRIPTION OF AIRCRAFT

Aircraft which wing and winglet assembly was subjected to the optimization process during work on this master's thesis is FAI 15m class sailplane Ventus 2ax manufactured by German based company Schempp-Hirth. Aircraft three view drawing could be seen in the appendix 1.

Choice of this aircraft is supported by effort of the improvement in performance of restricted span wing of the competition sailplane and possibility to explore potential gains of the morphing geometry winglet. Ventus 2ax already uses winglets designed by Dr. Maughmer, Ph.D. from The University of Pennsylvania, USA. Some of parameters of these winglets was chosen as the base for the optimization process. Reason, which lead to the effort of redesigning winglets is potential improvement of performance in flight regimes where fixed geometry winglet doesn't perform well as discussed in chapter 1.

Basic technical data of Ventus 2ax aircraft is mentioned in table 5.1.

Parameter	Designation	Value	Unit
Wing span	b_a	15,0	m
Wing area	S_w	9,67	m^2
Aspect ratio	AR_w	23,3	-
Empty weight	W_E	230	kg
Maximum take-off weight	W_{TO}	525	kg
Wing loading	W/S	30,9 – 54,3	kg/m^2
Max. water ballast	W_{WB}	200	kg

Tab. 5.1 Basic technical data of Ventus 2ax sailplane [21]

5.1 Ventus 2ax wing planform geometry

Wing planform with dimensions could be seen in figure 5.1.

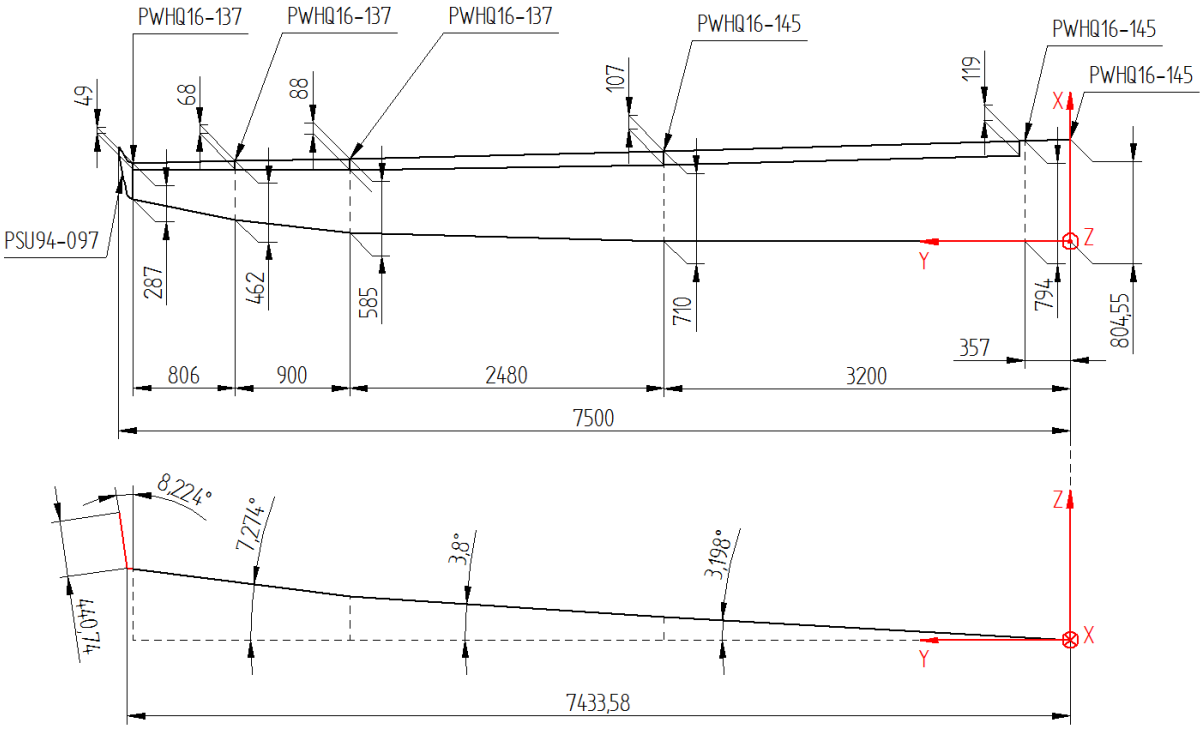

Fig. 5.1 Ventus 2ax wing geometry

Chord length and position of mean aerodynamic chord leading edge point of the wing is following:

Chord length	Span-wise position	Stream-wise position	Vertical position
c_{MAC}	y_{MAC}	x_{MAC}	z_{MAC}
673,340	3320,068	38,925	203,432
mm	mm	mm	mm

Tab. 5.2 Mean aerodynamic chord data

Location of the coordinate system origin is on the leading edge of the airfoil in the symmetry plane of the wing. X axis is heading from leading to trailing edge, y axis direction is from the

symmetry pane of the wing towards the wing-tip and finally z axis is perpendicular to the x and y axes.

In the upper part of the figure 5.1, the planform view of wing including winglet is shown. Wing is consisting of four trapezoidal sections. Geometrical twist of wing is equal to zero at all sections. Inner most trapezoid section airfoils are PWHQ 16-145. Two outer trapezoid sections uses PWHQ 16 – 137 airfoils and finally trapezoid section number two counted from the plane of symmetry of wing uses PWHQ 16-145 airfoil at its root and PWHQ 16-137 at tip. Winglet airfoil is PSU 94-097 along its whole span. Dimensions of flaps are also included. Flap consist of three sections. First section is placed at the trailing edge of first trapezoid section of the wing. Second section is placed at the trailing edge of second trapezoid section and finally third section is part of the trailing edge of third and fourth trapezoidal section of the wing (all measured from plane of symmetry of wing).

In the lower part of figure 5.1, dihedral angles of individual trapezoidal section are shown. All dihedral angles are measured in the planes running through sections airfoils chord lines. In the case of winglet, cant angle is measured from vertical to projection of line connecting winglet airfoil quarter chord points to the front plane. Winglet, which is connected to the wing is displayed in red colour and its geometry corresponds to the reference winglet geometry (i.e. neutral position without any deflection).

Deflection of the flaps are considered to be constant at whole wingspan. Deflections of flaps are mentioned in table 5.2. All deflection are measured as distance between trailing edge of fix part of wing and trailing edge of flap at root of the flap innermost section. Only deflections at flap position -2 and +2 are mentioned also as angle value, because these are positions of interest in the optimisation process described later in this thesis.

Flap position	Deflection at root of flap	Deflection of flap
[-]	[mm]	[°]
S1	-27	-
S	-23	-
-2	-18	-8,609
-1	-9	-
0	0	-
1	9	-
2	15	7,172
L	22	-

Tab. 5.2 Deflection of flaps of Ventus 2ax sailplane

5.2 Ventus 2ax wing and winglet airfoils

Airfoils used at the Ventus 2ax wing are mentioned in section 5.1. Airfoils PWHQ 16-137 and PWHQ 16-145 are laminar airfoils optimized for use at high performance sailplanes.

PWHQ 16-137 airfoil has maximum thickness of 13,7 percent at 43,43 percent of chord with maximum camber 4,42 percent at 47,47 percent of chord.

PWHQ 16-145 airfoil has maximum thickness of 14,5 percent at 43,43 percent of chord with maximum camber 4,47 percent at 43,43 percent of chord.

Winglet airfoil PSU 94-097 is shown in figure 5.3.

PSU 94-097 airfoil is airfoil optimized for use at sailplane winglets and has maximum thickness of 9,7 percent at 32,32 percent of airfoil chord and maximum camber of 4,10 percent at 46,47 percent of airfoil chord.

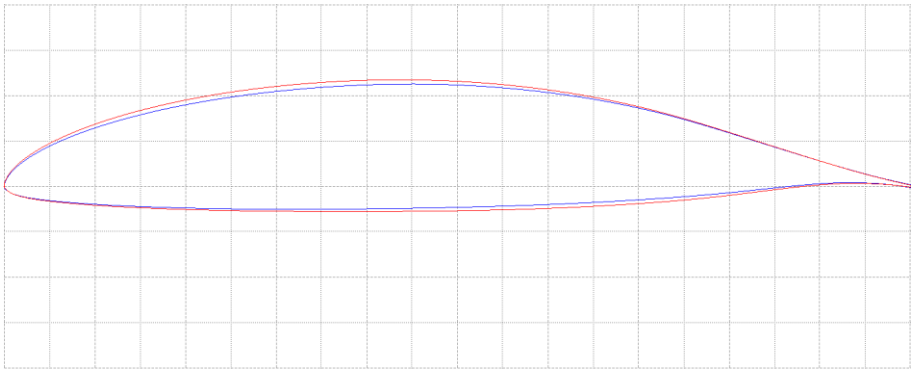

Fig. 5.2 PWHQ 16-137 (blue) and PWHQ 16-145 (red) airfoil

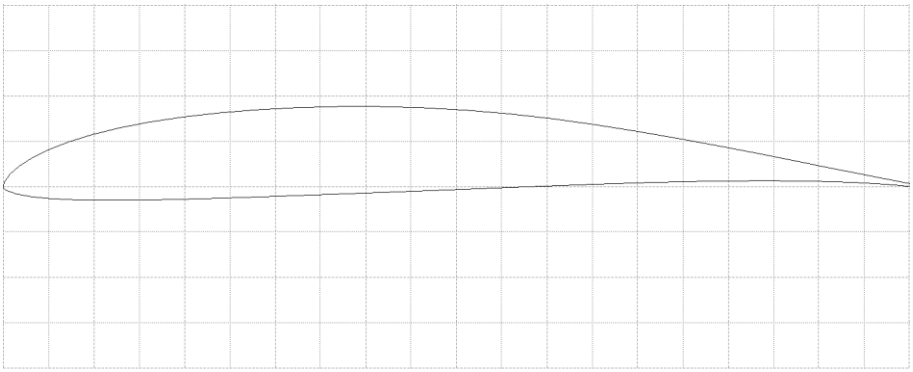

Fig. 5.3 PSU 94-097 winglet airfoil

5.3 Ventus 2ax original winglet geometry

Winglet of Ventus 2ax, designed by Dr. Maughmer, Ph.D. has scimitar-like planform shape. Shape of winglet together with airfoil selection and twist distribution is the result of effort to obtain as smooth lift distribution along the wing, winglet junction to wing and winglet as possible. This leads to the optimal solution from the additional profile drag and from the induced drag reduction point of view. Winglet design mustn´t be focused only on the reduction of induced drag, as addition of the winglet causes additional profile drag to the wing. In general, the profit of wing induced drag reduction must overcome the penalty of additional profile drag. Finally, the shape of the winglet of Dr. Maughmer is showed in figure 5.4.

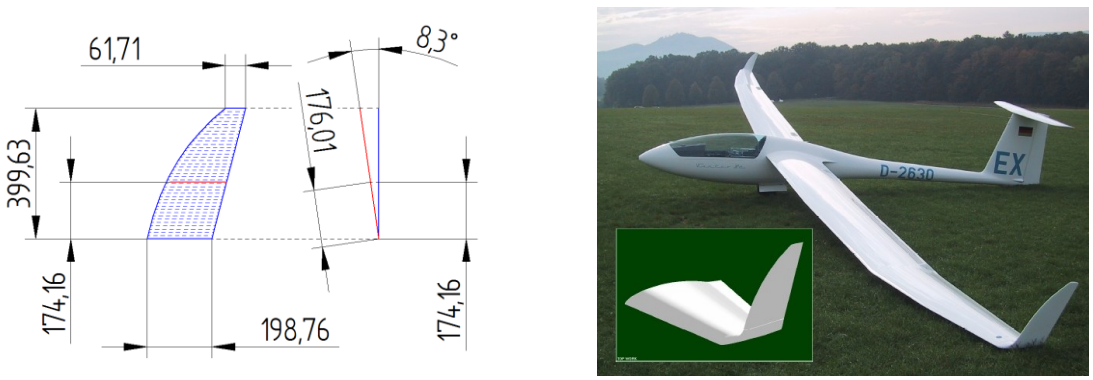

Fig. 5.4 Original Ventus 2ax winglet geometry [9]

In the left portion of figure 5.4, approximate geometry of winglet is mentioned including dimensions and position of c_{MAC}. In the right portion of figure 5.4, 3D cad model of winglet and winglet installed on Ventus 2ax sailplane is shown.

In the optimisation process, which is subject of this thesis, new winglet geometry was proposed in the term of simplification of winglet planform geometry to the trapezoidal shape. New trapezoidal winglet has same value of mean aerodynamic chord and same position of mean aerodynamic chord on the winglet span.

6 AIRWORTHINESS REQUIREMENTS

As the winglet is structural part of the sailplane, the compliance with applicable paragraphs of airworthiness regulations must be met. These requirements are mentioned for completeness of the winglet design process description.

Airworthiness regulation applicable to the sailplane winglets design within European union is mentioned in the regulation CS-22 Certification Specification for Sailplanes and Powered Sailplanes.

Paragraph, which describes design requirements for winglet is CS 22.375 Winglets. Full version of CS-22 airworthiness regulation is placed at the European Aviation Safety Agency website. At this place, only the most important aspect will be mentioned. Exact wording of CS 22.375 is below.

When winglets are installed the sailplane must be designed for side loads due to maximum sideslip angle of the winglet at design manoeuvring speed V_A, loads resulting from gust acting perpendicularly to the surface of winglet at design gust speed V_B and design dive speed V_D, mutual interaction effects of winglets and wing on aerodynamic loads, hand forces on the

winglets and loads due to wingtip landing as specified in CS 22.501, if the winglet can touch the ground. [11]

In the absence of more logical rational analysis the loads must be computed as follows:

The lift at the winglets due to sideslip at V_A:

$$L_{Wm} = 1{,}25 \cdot C_{L_{max}} \cdot S_{WL} \cdot \frac{\rho_0}{2} \cdot {V_A}^2 \qquad \text{[11] (6.1)}$$

Where: $C_{L_{max}}$ is maximum lift coefficient of winglet profile

S_{WL} is area of winglet

ρ_0 is air density at sea level (ISA)

V_A is design manoeuvring speed

The lift at the winglets due to lateral gust at V_B and V_D:

$$L_{Wg} = a_W \, S_{WL} \, \frac{\rho_0}{2} \, V \, U \, k \qquad \text{[11] (6.2)}$$

Where:

a_W is slope of winglet lift curve per radian

k is gust alleviation factor as defined in CS 22.443 (b)

U is lateral gust velocity at the values as described in CS 22.333 (c)

The above-described load L_{Wg} need not to exceed the value:

$$L_{Wmax} = 1{,}25 \cdot C_{L_{max}} \cdot S_{WL} \cdot \frac{\rho_0}{2} \cdot {V_{max}}^2 \qquad [11]\ (6.3)$$

Hand forces of 15 daN must be assumed to act at the tip of the winglet in horizontal inboard and outboard direction parallel to the span-wise axis of the wing and in horizontal forward and backward direction parallel to the longitudinal axis of the fuselage. [11]

In addition, the rigging loads as specified in paragraph CS 22.591 must be applied if the winglet plane is not normal to the plane of the wing. [11]

Wing-tip landing which is described in paragraph CS 22.501 considering maximum load of 40 daN in the rearward direction parallel to the longitudinal axis of the fuselage at the point of contact of wing with the ground.

Rigging and de-rigging loads is described by paragraph CS 22.591 as follows.

A rigging limit load of plus and minus twice the wing-tip reaction, determined when either a semi-span wing is simply supported at root and tip or when the complete wing is simply supported at the tips, where this would be representative of the rigging procedure, must be assumed to be applied at the wing tip and reacted by the wing when supported by a reaction and couple at the wing root. [11]

All above mentioned requirements of the CS-22 Certification Specification must be met by the final design of the winglet. It would be very challenging to meet these requirements in case of morphing winglet design. However, meeting the requirements of the CS-22 is only one part of the potential problems from practical point of view. Another problem would probably lay in the manipulation with the aircraft on the ground for example in the situation of initial phase of the take-off where end of the glider wing must be supported by the wing runner. Wing to winglet junction trailing edge is often used as the wing runner grip point, which would be problematic in case of flexible structure.

7 SAILPLANE CROSS-COUNTRY FLIGHT MODEL

One of the basic steps of the sailplane design process is description of the typical flight profile. Qualitative description is not enough from the point of design optimization process and because of that, mathematical models are applied. Sailplane flight usually comprise of two different segments. Sailplane is increasing its altitude by circling flight in thermals which is formed by the ascending air hotter than air in its vicinity. Second segment of flight is called interthermal flight. Sailplane pilot puts maximum effort to achieve maximum possible average speed during cross country flight. Many different and more or less complex cross country flight models were crated to describe typical weather conditions during these flights. For example, the Quast´s model of 300 km cross country flight will be mentioned. Fig. 7.1 shows Quast´s weather model.

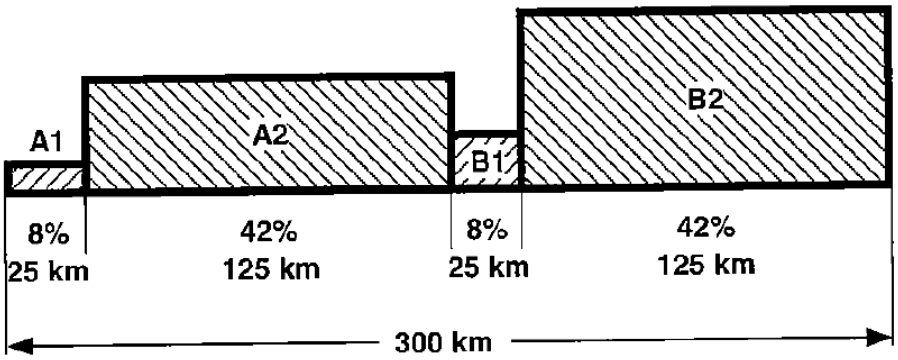

Fig. 7.1 Quast´s weather model applied to typical 300 km flight [5]

Quast's weather model utilizes four different thermal models defined by Horstmann. The Quast's model is relatively insensitive to the changes in the portions of individual thermal types. [5]

K. Horstmann proposed thermal model proved as relatively realistic, particularly in modeling of typical European weather conditions. Thermal model consists of four different typical thermals, varying in strength, width and radial distribution of lift. Standard thermal profiles of Horstmann model are shown in figure 7.2.

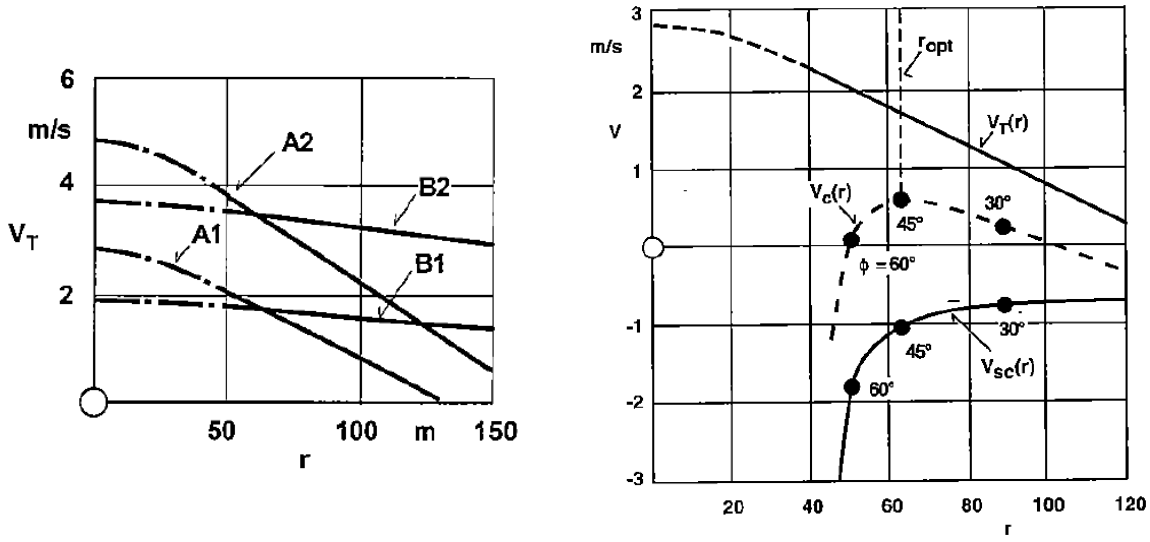

Fig. 7.2 Horstmann standard thermal profiles (left) and rate of climb of ASW-19 in A1 model (right) [5]

During the circling in thermal, target of the glider pilot is to achieve maximum possible climb speed. During the sailplane design, the thermal profile models are used together with circling polar of sailplane to determine optimal bank angle and speed in the thermal. Example of the thermal profile and circling polar combination of ASW-19 glider in A1 type thermal model is shown in figure 7.2. It is obvious, that speed of descent V_{sc} is dependent on the turn radius, or in another word on the bank angle and speed. As the bank angle increases and turn radius tightens, centrifugal force increases and required lift coefficient increases too. This causes shift of the sailplane operating point to the higher portion of the drag polar and to lower glide ratio area where V_{sc} is higher. Opposite to the above-mentioned increase of V_{sc} as the turn radius decrease, the thermal strength increase. These considerations lead to the conclusion that

some optimal turn radius exist at which climb speed of the sailplane is highest what is apparent from the figure 7.2.

After decision to exit thermal and move to another one, next phase of sailplane flight occurs. This phase is interthermal flight. As in the case of the circling flight in the thermal, also interthermal flight should be optimized in the way of choosing right interthermal glide speed. However, it is difficult to tell what airspeed is the right one. Interthermal glide speed is strongly dependent on the next thermal strength which could be only predicted in real environment. This is not the case, when the weather model is applied during the sailplane design. Description of the interthermal glide problematics follows.

As the interthermal glide speed has major influence on the average cross-country speed, some more detail has to be putted on this flight phase. If the interthermal glide speed is defined by maximum glide ratio of the aircraft K_{max}, then next thermal is reached at highest altitude (case A). If higher airspeed (case B and C) than in case A, is chosen, than next thermal is reached at lower altitude than in case A , but in shorter time. If the thermal is strong enough so the sailplane (in case B or C) could climb to altitude higher than the altitude where thermal is reached in case A within time difference between the thermal is reached in case A and other cases (B or C), than it is beneficial to choose interthermal glide speed higher than in case A. Cases A, B and C are shown in the figure 7.3. [5]

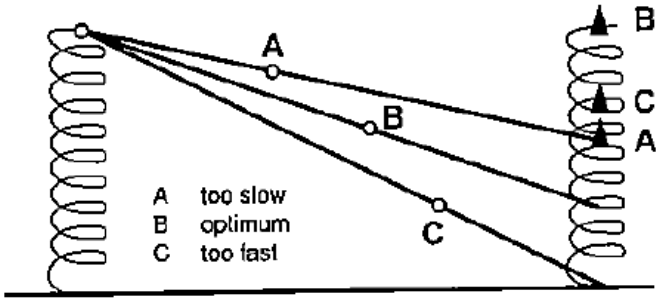

Fig. 7.3 Interthermal glide with different airspeeds [5]

As was mentioned above. Optimal interthermal glide speed is function of the thermal strength. From the sailplane designer point of view, strength of thermal is known and defined by the thermal model. This means, that it is possible to evaluate influence of the thermal strength on some of the design parameters of the aircraft. This is clearly visible in the figure 7.4 which shows influence of the aspect ratio, wing loading and thermal strength on the optimum interthermal glide speed.

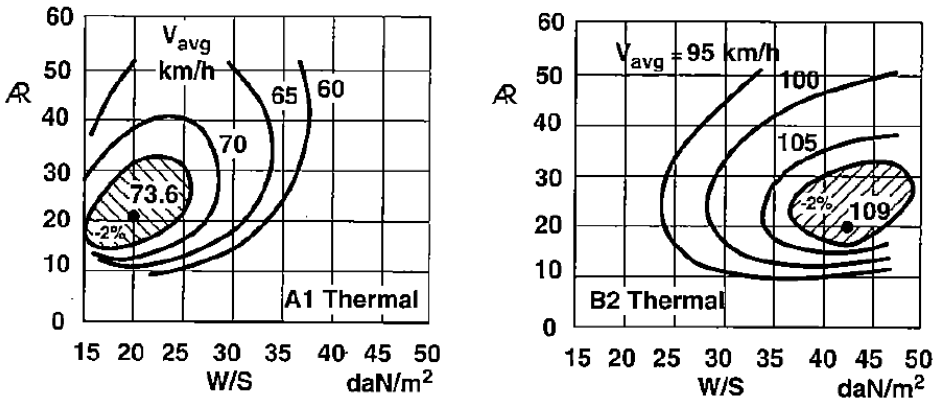

Fig. 7.4 Interthermal glide airspeed dependence on design parameters [5]

The wing, that was used for the figure 7.4 creation has fixed wingspan of 20m and airfoil FX 67-K-150. [5]

It is obvious, that profile of the cross-country sailplane flight leads to number of conflict design requirements. Wing loading should be high for interthermal glide, but low while thermaling. To ensure good performance in climb and in the interthermal glide, drag coefficients must be low as possible over wide range of lift coefficients, or speeds respectively. Finally, the circulation distribution should be close to the elliptical whether thermaling or gliding between thermals.

Regarding to the above-mentioned conflict requirements, the following notes should be given. In practice, the wing loading of the sailplane is influenced by use of the water ballast. Another two conflicts are interests of this master's thesis. Especially the request of low drag coefficient over the wide speed range. Morphing winglet could contribute to the lowering of drag in low speed thermal flight and in high speed interthermal glide by maximizing of winglet thrust at low speeds and high lift coefficients and by moving breaking point to the higher flight speed.

8 VENTUS 2AX WING AND WINGLET CAD MODEL

Ventus 2ax wing CAD model is created without any internal structure as it is intended for further use as the base for CFD model. All outer surfaces of the wing and winglet was created, however some simplifications were made. Fuselage and tail CAD model wasn't created whereas the complexity of the further CFD model should be excessive and contribution to the optimisation process would not justify increased computational requirements. However, optimization of winglets using CFD model of whole sailplane would be beneficial if performed in the future.

8.1 Wing CAD model

Wing CAD model was created to represent real wing geometry as closely as it is possible. However, some simplifications were made to obtain model, which could be used for computational mesh creation during the CFD pre-processing. Wing planform geometry and airfoils are described in chapters 5.1 and 5.2 of this thesis. Some of the characteristic steps of wing CAD model creation will be mentioned.

First step of CAD model design was the wireframe model creation. First of all, airfoil sections was positioned into right places within design space. Each trapezoidal segment of the wing has its own pair of airfoils positioned with right dihedral angle as shown in figure 8.1 and 8.2.

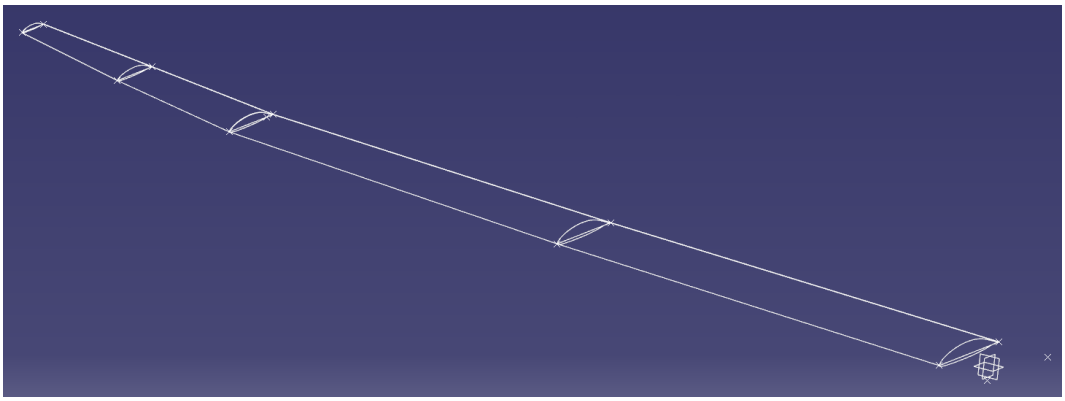

Fig. 8.1 Wing CAD model wireframe

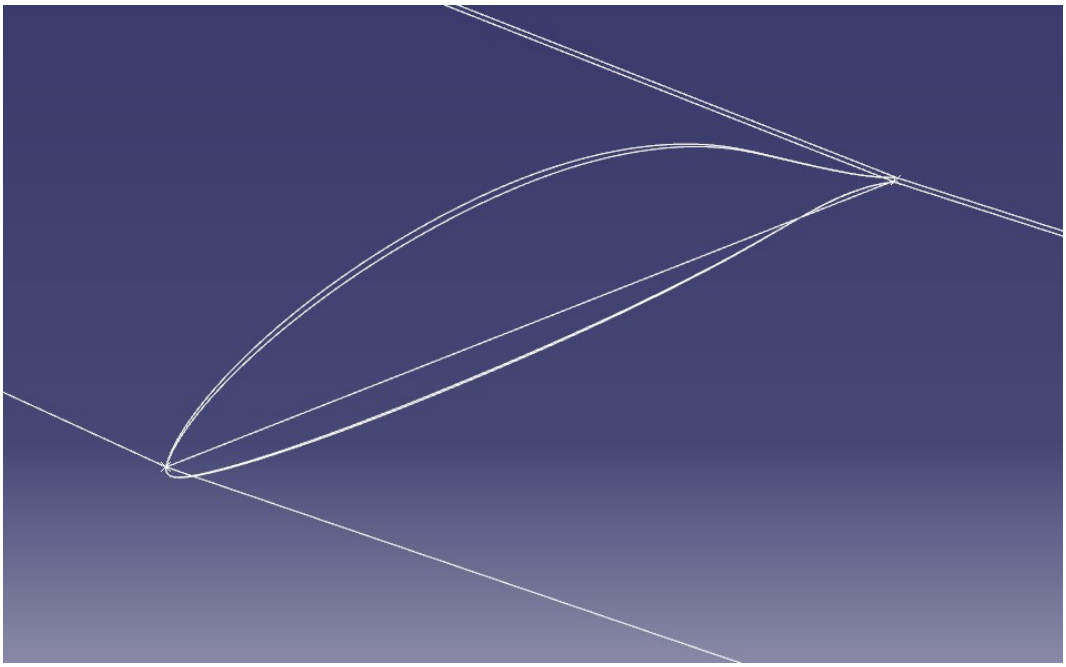

Fig. 8.2 Detail of the change in the dihedral angle of airfoil between section 2 and 3 of the wing.

After completion of the wing wireframe, the surface model was created. Transition between trapezoidal sections at upper and lower surface of the wing was created as smooth surfaces with tangency to the adjacent surfaces. Transition surface was created 3 mm wide.

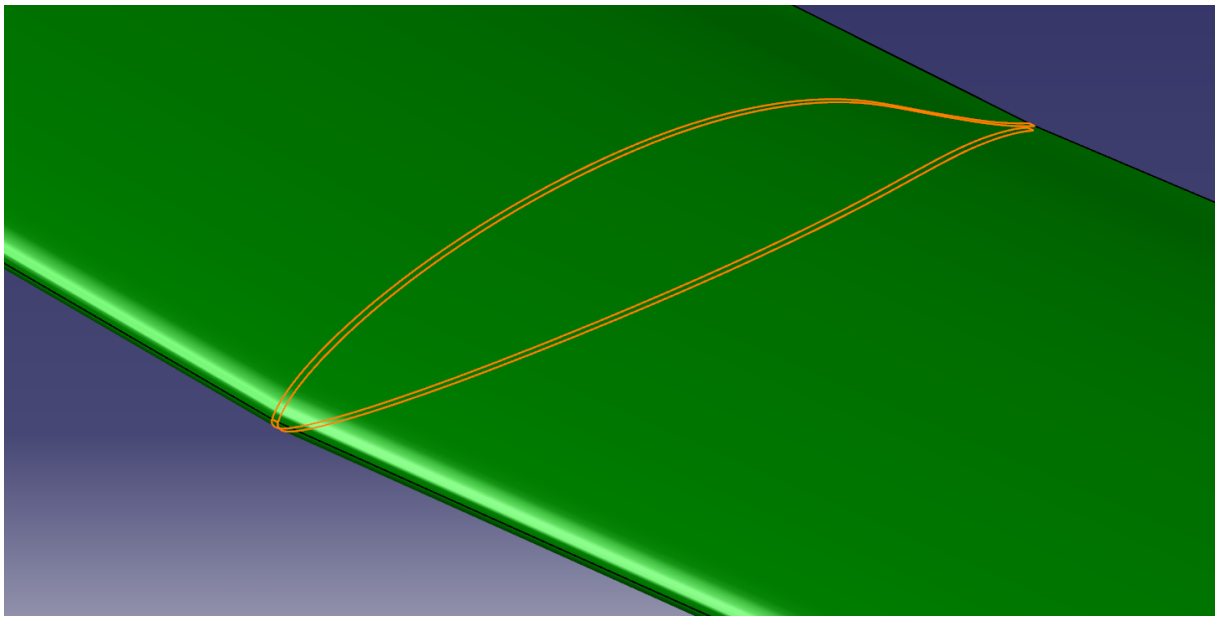

Fig. 8.3 Transition surface (highlighted) between surfaces of section 2 and 3 of the wing

Another important aspect of the wing CAD model in respect to the further CFD model creation was right choice of the trailing edge thickness along the wingspan. Best practice for the CFD models of sailplane wings in respect to the real sailplane wing trailing edge thickness is thickness value of around 2 mm, which was also chosen for the CAD model created during the work on this master's thesis. To ensure, if the value of 2 mm is close enough to the reality, thickness of the trailing edge of Ventus 2cm airplane with registration OK-0070 was measured on the multiple locations of the trailing edge and average value of 1,5 mm was measured.

As the CFD simulations, which will be described within section 9 of this thesis are focused on the low speed and high-speed flight regimes it is not possible to perform this simulations with wing flaps in the neutral position. Flap positions of +2 and -2 was chosen as representative for low speed and high-speed flight regime respectively. After decision was taken to perform simulations with these flap positions, CAD model must be adjusted and simplified model of flaps was created. Planform geometry of flaps are described in the figure 5.1 in section 5.1. Flaps hinge location is in the 50% of the local thickness of the wing.

Simplified flaps geometry was created by splitting the flap surfaces apart of the wing and deflecting the flap to the desired deflection angle of 7,172 degrees and -8,609 degrees for low speed and high-speed flight regimes respectively. Transition between fixed geometry of the wing and deflected flap was created by adding of conical tangent surfaces. For better description, geometry of the flap to wing fixed portion transition surface of flap in +2 position is highlighted in the figure 8.4.

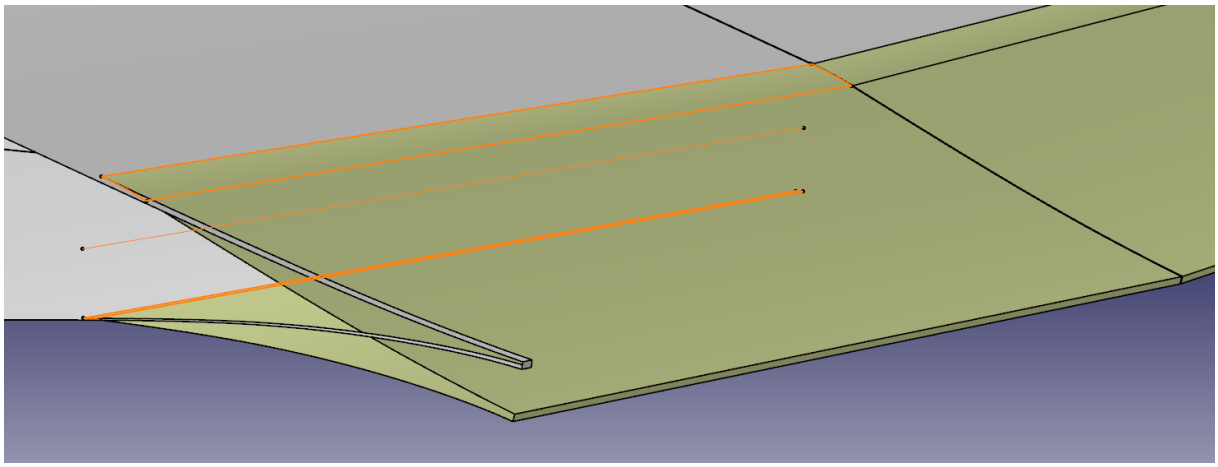

Fig. 8.4 Wing to flap transition surfaces and axis location for innermost flap section

Another simplification within the wing CAD model is omitting of the gaps between segments of flaps and also between the innermost segment of flap and fixed wing portion and between outermost flap segment and winglet inboard airfoil section.

8.2 Winglet CAD model

First step, even before the CAD model design was transformation of the original Ventus 2ax winglet planform shape to the trapezoidal shape. The baseline idea was to achieve the same position and length of winglet mean aerodynamic chord c_{MACwlt} . Dimensions of the new trapezoidal planform winglet is described by figure 8.5.

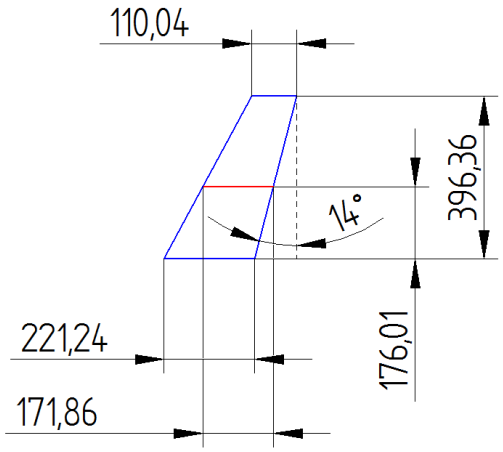

Fig. 8.5 Trapezoidal winglet dimensions

CAD model of winglet was created with the ability of easy change of geometric parameters, which are the subject of the optimisation process. These parameters are toe-in, twist and cant angles. As in the case of the wing, first step was the creation of the wireframe model of winglet. However, parametrization of winglet geometry made this step different in the point of necessity of reference point and reference winglet chord position definition. Firstly, winglet platform was created in the plane, which was placed at the winglet cant angle and run through the cant angle change axis of the winglet (figure 8.6).

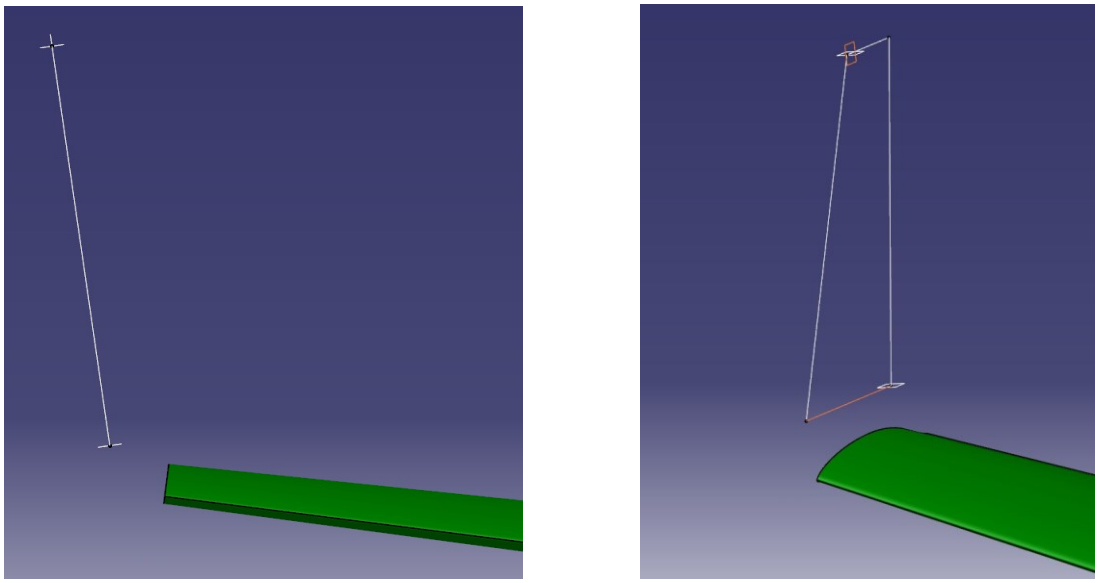

Fig. 8.6 Winglet planform (winglet plane and cant axis highlighted – right)

After right alignment of the winglet reference planform, quarter chord points were created on the upper and lower winglet airfoil chord reference lines. Then, airfoils PSU 94-097 of the winglet was placed into the wireframe and leading edge and trailing edge lines were added. At this phase, airfoils was rotated so the winglet has right toe-in and tip-in angle values of -3 and -1 degrees respectively (figure 8.7).

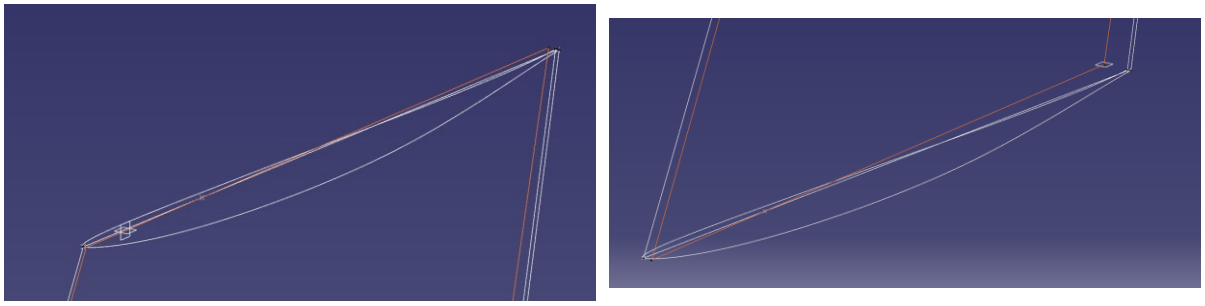

Fig. 8.7 Winglet airfoils (winglet plane highlighted)

When winglet wireframe was finished, basic surfaces of the winglet were created. Important part of the parametric model is wing winglet junction surfaces, which must be designed to allow rotation of the winglet root airfoil around the quarter chord point and the rotation of the whole winglet surface around the cant change axis highlighted in the right portion of the figure 8.6. Winglet to wing junction upper and lower surfaces is shown in the figure 8.8.

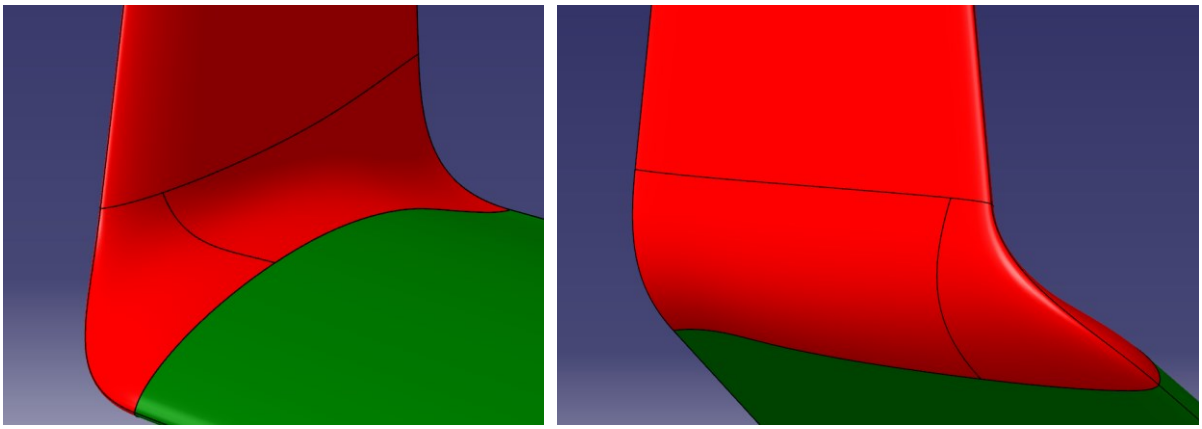

Fig. 8.8 Winglet to wing junction geometry

Deformation of the wing to winglet junction due to the cant angle change is shown in the figure 8.9. Deformation due to toe-in angle change is shown in the figure 8.10.

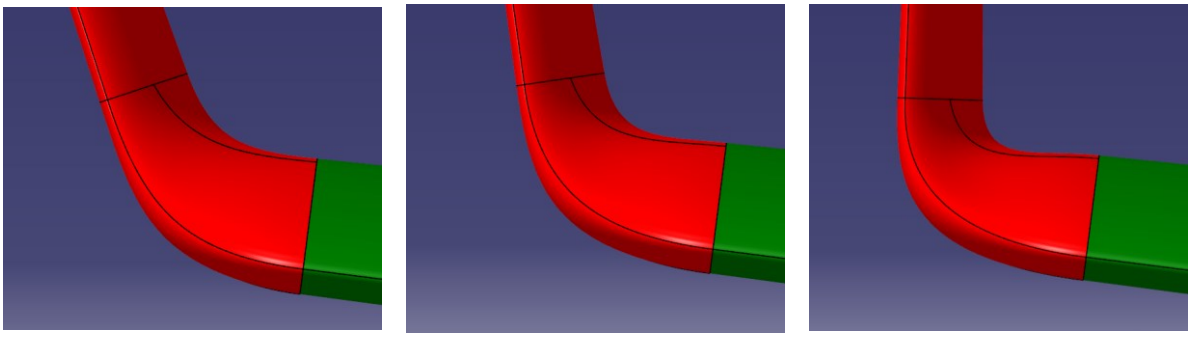

Fig. 8.9 Winglet to wing junction geometry deformation due to cant angle change

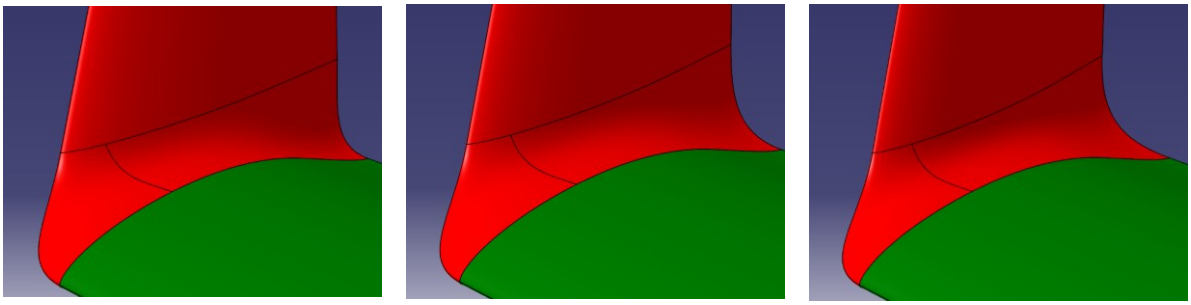

Fig. 8.10 Winglet to wing junction geometry deformation due to toe-in angle change

Deformations of the junction would have limited, but not negligible impact on the airflow over this portion of the geometry. Influence of the wing to winglet transition surface shape on the airflow in this area would be briefly described in the CFD section of this thesis.

For the completeness of the winglet geometry description, the trailing edge thickness was defined as 1 mm, which corresponds to the tendency of achieving winglets trailing edge as thin as possible in practice. However, thickness below 1mm is hard to achieve due to technological reasons.

9 VENTUS 2AX WING AND WINGLET CFD MODEL

After completing CAD model, steps were taken to create high quality CFD model of the wing and winglet geometry. Both major steps of the CFD model creation, mesh generation and solver settings, are important as they have major influence on the final solution and optimised shapes. Whole process of the CFD model design and evaluation of CFD solutions for reference geometry of winglet will be described within this chapter.

9.1 Geometry import

Firstly, CAD geometry must be imported to create mesh. Geometry was exported form CATIA CAD software in IGES export format. Few steps must be taken before export to achieve CAD surfaces without holes at the surfaces borders and without other geometry defects like overlaying surfaces et cetera.

One of the key steps before importing geometry to the meshing software ICEM CFD was stitching all surfaces together to minimize probability of above mentioned holes in the geometry.

Another step, which should be taken was creation of small additional geometry elements, that are used to avoid problems, which may occur during the prism layers creation, which will be described in the chapter 9.3. Problem in relation with prism layers extrusion lays in the probability of the pyramid elements creation during prism layers extrusion. Problems are most probable in the more complex areas of geometry, where multiple, and also differently oriented surfaces meet. In particular case of CAD geometry used within this thesis, above mentioned complex areas are the root and the tip area of the wing flap. Flap root and tip areas of the reference case with flap deflected to position +2 are shown in the figure 9.1 and 9.2 including additional geometry elements.

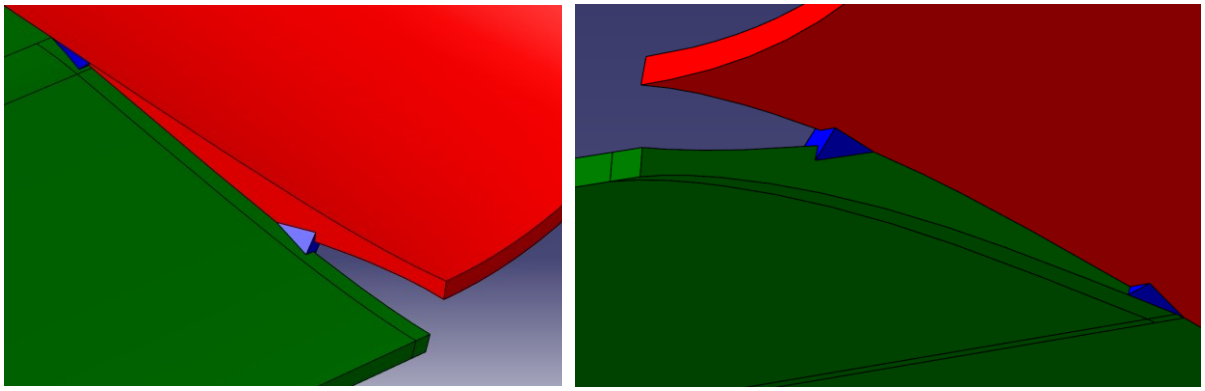

Fig. 9.1 Flap tip area with additional geometry (blue)

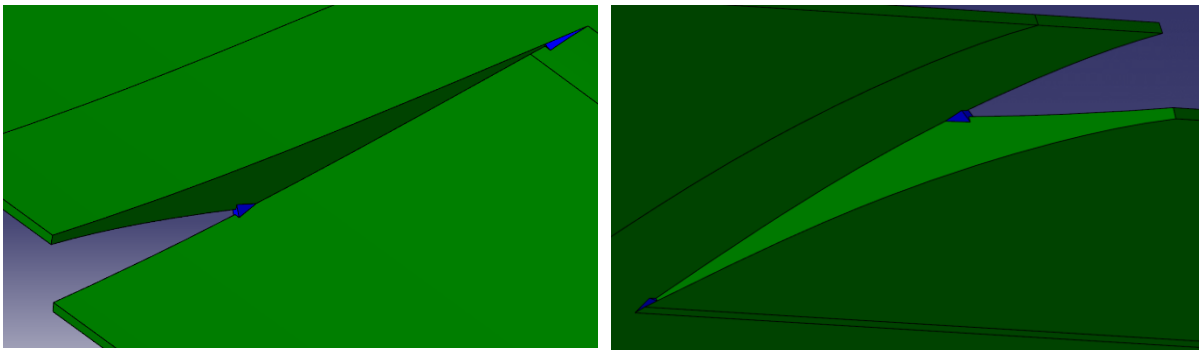

Fig. 9.2 Flap root area with additional geometry (blue)

When the surfaces were prepared within CAD software and exported to IGES format, the import to ICEM CFD follows. Model is imported with the same orientation and placed to the same position within the coordinate system as the original in the CAD system. After import of the model, new topology was created and checked for possible problems. Topology created right after import to ICEM CFD could be seen in the figure 9.3.

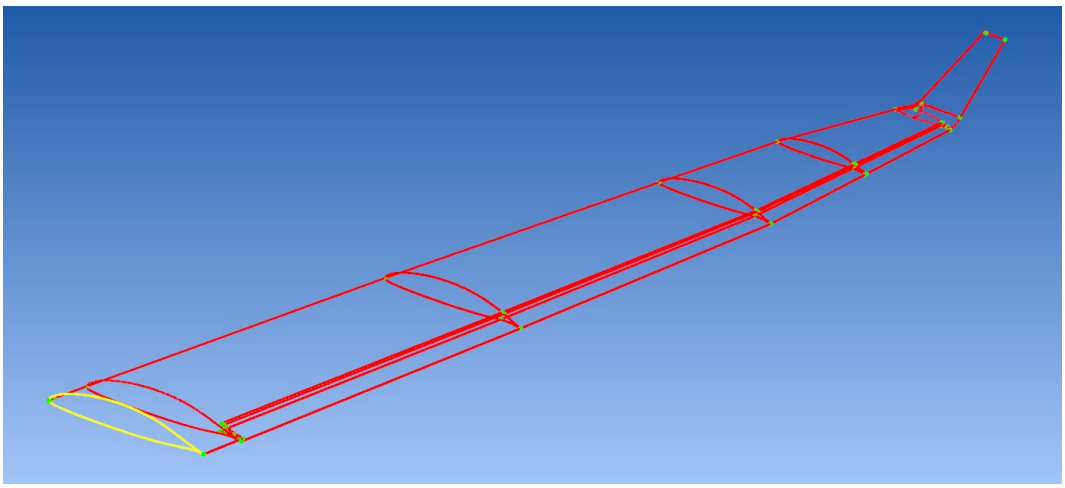

Fig. 9.3 Topology of the wing and winglet after automatic creation

Topology is used within the ICEM CFD during the surface meshing as the reference for the elements points and borders. It is not necessary to use all of the topology, and it could be said, it is better to use the topology only at the physical edges and corners of the object intended for meshing. Otherwise, desperate change in the surface tri elements size would occur and this change would transfer to the volume tetrahedra elements, which could lead to the low quality of mesh. Because of that, the best practice is to manually clean the created topology. Topology after removal of unnecessary lines and points could be seen in the figure 9.4.

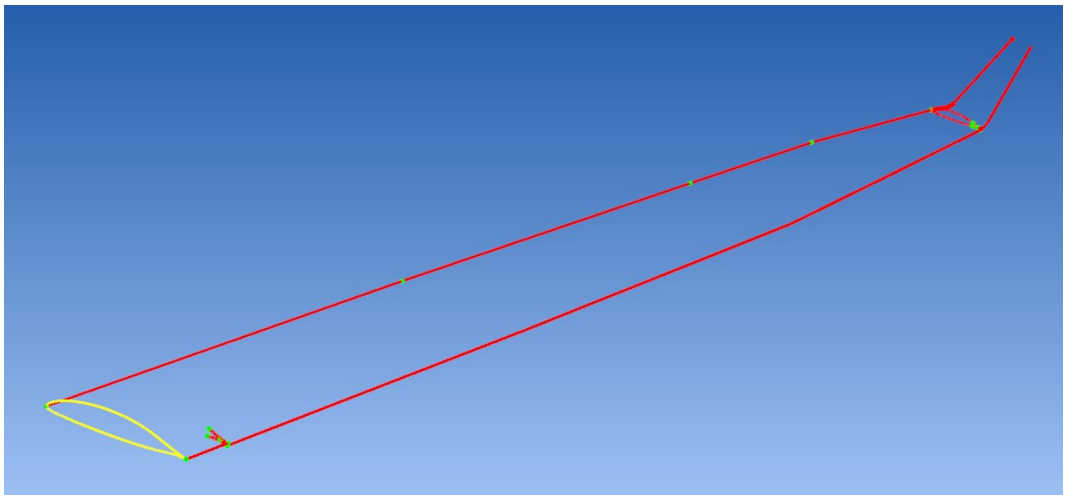

Fig. 9.4 Topology of the wing and winglet after manual cleaning

9.2 Fluid domain design

Fluid domain is of the major importance when it comes to CFD simulations. For this particular case, the semi-hemisphere fluid domain with pressure-far-field boundary condition was used. This type of domain is very useful in case, when the angle of attack for which the problem should be solved is unknown before the first computations, so the assumption is made, that easy change of angle of attack will be beneficious.

Another aspect after the domain shape is the dimensions of the domain. Domain must not be excessively small when the pressure-far-field boundary condition is applied, because of the probability of strong interaction between pressure far field boundary and the object undergoing CFD investigation. On the other hand, excessively large domain may lead to the excessively high number of the volume elements inside domain. Finally, the hemisphere radius was defined as 30 times the half-span of the wing:

$$R_{domain} = 30 \cdot s_a \tag{9.1}$$

Where half-span of the wing is defined as:

$$s_a = 7500\ mm \tag{9.2}$$

And finally, domain radius is:

$$R_{domain} = 225\ 000\ mm \tag{9.3}$$

Centre of the hemisphere is located at the quarter chord point of the airfoil in the plane of wing symmetry. Centre point coordinates in mm units are displayed in the figure on the following page.

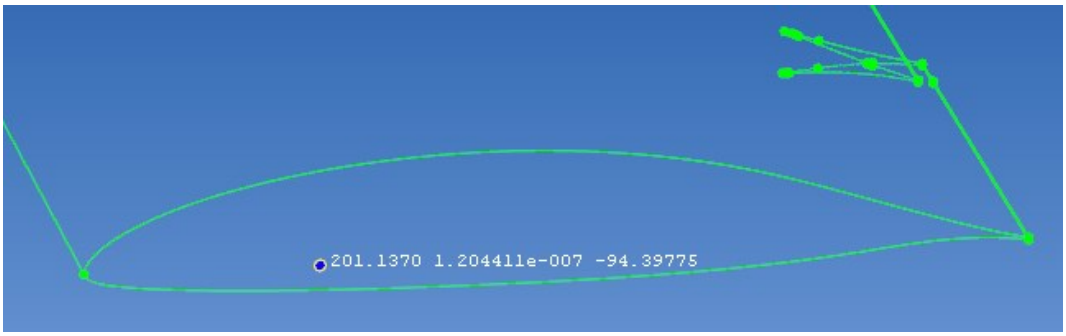

Fig. 9.5 Domain centre point

Relation of the fluid domain radius to the half-span of the wing was chosen based on experiences of Institute of Aerospace Engineering at Brno University of Technology.

Fluid domain hemisphere surface defined by centre point coordinates (fig. 9.5) and radius (eqn. 9.3) uses boundary condition pressure-far-field. The circular area in the plane of symmetry uses symmetry boundary condition, which is useful from the computational resources point of view. Only half of the geometry is modelled, which lead to the significant reduction of the mesh elements count and computational time. Domain is displayed at the figure 9.6 below.

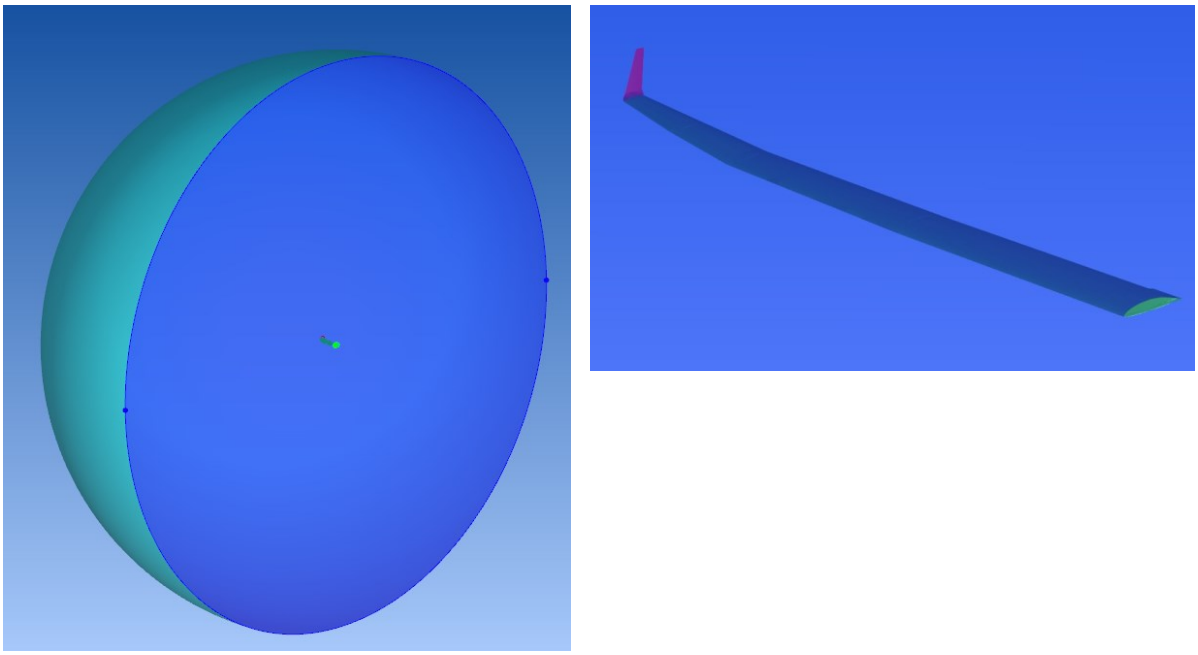

Fig. 9.6 Domain symmetry plane (left – dark blue) and pressure-far-field (left – light blue)

Fluid is located inside the fluid domain and fills the space circumscribed by the symmetry plane, pressure-far-field, winglet surface and wing surface. This means that all fluid is outside the wing. Fluid used during wing and winglet CFD simulations is air with properties corresponding to 0m altitude of international standard atmosphere (ISA).

9.3 Meshing parameters

When fluid domain design was finished, the parameters of the mesh must be defined. The mesh setup should be divided to wing and winglet surface mesh maximum size definition, mesh densities definition and global mesh parameters definition.

Surface mesh of the wing and winglet have different maximum element size defined for individual surfaces. This is mainly because the different curvature of the surfaces. Rule of thumb is larger maximum element size may be used on the surfaces with low curvature and opposite to that small elements should be used when curvature is high. This will ensure, that shape of the surface mesh will be close enough to the exact surfaces shape of the CAD model. For better understanding of the maximum element sizes on the different surfaces, wing upper and lower surfaces are displayed at the figures 9.7 and 9.8 with designation of the individual surfaces and maximum element size used is mentioned in the table 9.1.

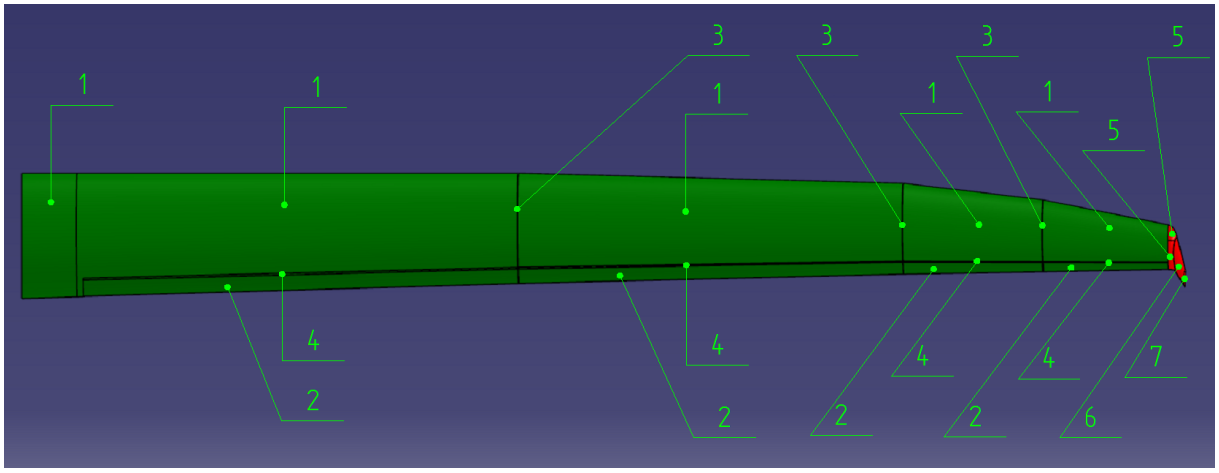

Fig. 9.7 Individual surfaces of the wing and winglet upper side

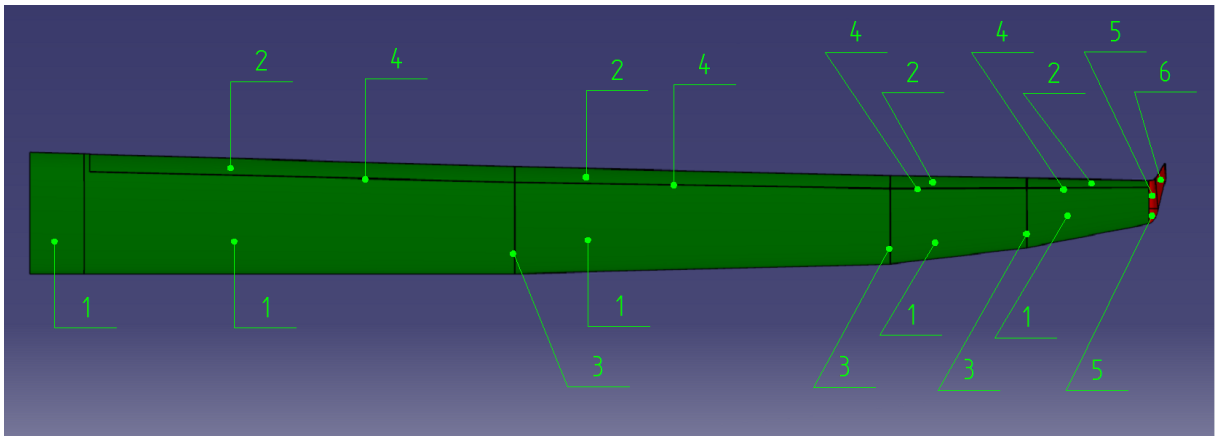

Fig. 9.8 Individual surfaces of the wing and winglet lower side

Surface number	Description	Max element size value
1	Wing upper and lower surface	30
2	Flaps upper and lower surface	22.5
3	Surfaces of dihedral angle change	15
4	Wing to flap transition surfaces	9
5	Wing to winglet junction	7.5
6	Winglet upper and lower surface	15
7	Tip surface of the winglet	3
-	Winglet trailing edge	1
-	Wing trailing edge	2
-	End surfaces of the flaps	2
-	Additional geometry elements (fig. 9.1, 9.2)	0.5

Tab. 9.1 Maximum elements sizes of the wing surface mesh

To obtain smaller elements on the wing and winglet leading edge in order to maintain surfaces curvature in that regions, the mesh densities had to be defined. Densities was defined on the linear segments on the wing and winglet leading edge. On the wing to winglet junction, densities run through additional points created especially for leading edge densities definition. Wing to winglet junction mesh densities is shown on figure 9.9.

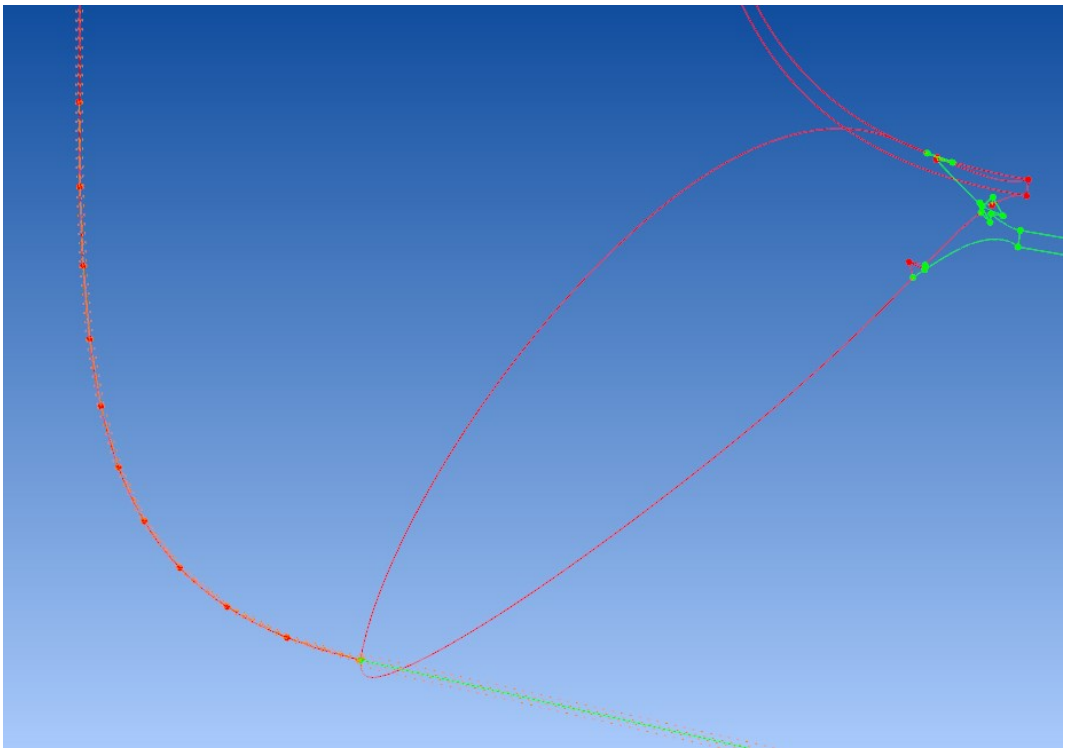

Fig. 9.9 Leading edge densities on the wing to winglet junction (orange)

Leading edge mesh densities was defined as follows.

Region	Size	Ratio	Width
Wing leading edge	0.3	0	1
Winglet leading edge	0.6	0	1

Tab. 9.2 Mesh densities parameters definition

Parameters of the mesh densities definition will be explained in this paragraph. Size parameter define maximum element size allowed in the region of mesh density. Ratio parameter defines the tetra parameters growth ratio in the direction away from the mesh density. And finally, Width parameter defines number of layers of the specified element size away from the boundary of the density region, that should have a constant expansion ratio. The layer N+1 will have a tetra size of the Size value multiplied by the Ratio. [12].

Global mesh parameters are defined for the whole domain and their definition is divided into following segments. Segments of global mesh parameters definition are Global Mesh Size, Shell Meshing Parameters, Volume Meshing Parameters and Prism Mesh Parameters. Settings of all parameters are mentioned in the tables 9.3 through 9.6, below.

Global Mesh Size	
Global Element Scale Factor	Scale factor: 1.25
Global Element Seed Size	Mex element: 4096.0
Curvature / Proximity Based Refinement	Enabled
	Min size limit: 0.2
	Elements in gap: 1
	Refinement: 12

Tab. 9.3 Global Mesh Size parameters definition

Shell Meshing Parameters	
Mesh type	All Tri
Mesh method	Patch independent
Section	Patch independent

Tab. 9.4 Shell Meshing Parameters definition

Volume Meshing Parameters	
Mesh Type	Tetra / Mixed
Tetra / Mixed Meshing	Robust (Octree)
	Edge criterion: 0.2
	Smooth mesh: Enabled
	Smooth Iterations: 5
	Min quality: 0.4
	Fix Non-manifold: Enabled
	Fix Holes: Enabled

Tab. 9.5 Volume Meshing Parameters definition

Prism Mesh Parameters	
Growth law	Exponential
Initial height	60
Height ratio	1
Number of layers	2
Total height	120
Min prism quality	1e-006
Orto weight	0.5
Fillet ratio	1
Max prism angle	180
Prism height limit factor	0.4
Smoothing Options	Number of surface smoothing steps: 10
	Triangle quality type: Laplace
	Number of volume smoothing steps: 10
	Max directional smoothing steps: 10
	First layer smoothing steps: 10

Tab. 9.6 Prism Mesh Parameters definition

9.4 Meshing process

Creation of the computational mesh is defined by 12 steps. An overview of the meshing process steps is mentioned in the table 9.7 below. More detailed description of the meshing steps is below table 9.7.

Step number	Step description
1	Compute Mesh - Volume meshing – Robust (Octree)
2	Smooth Mesh Globally
3	Check Mesh
4	Compute Mesh – Prism mesh
5	Split Mesh – Split layer 0 to 5 layers
6	Split Mesh – Split layer 5 to 5 layers
7	Move Nodes – Redistribute Prism Edge – Fixed Initial Height
8	Smooth Mesh Globally – Tetra (Smooth), Tri (Freeze), Penta (Freeze), Quad (Freeze)
9	Check Mesh
10	Smooth Mesh Globally – Tetra (Smooth), Tri (Smooth), Penta (Smooth), Quad (Smooth)
11	Check Mesh
12	Output – Boundary Conditions
13	Output – Write Input

Tab. 9.7 Prism Mesh Parameters definition

Step 1: Global mesh was created including surface mesh of the Wing, Winglet, Pressure-Far-Field and Symmetry Plane and volume mesh inside the fluid domain.

Surface mesh of the part of wing and winglet is displayed in figure 9.10.

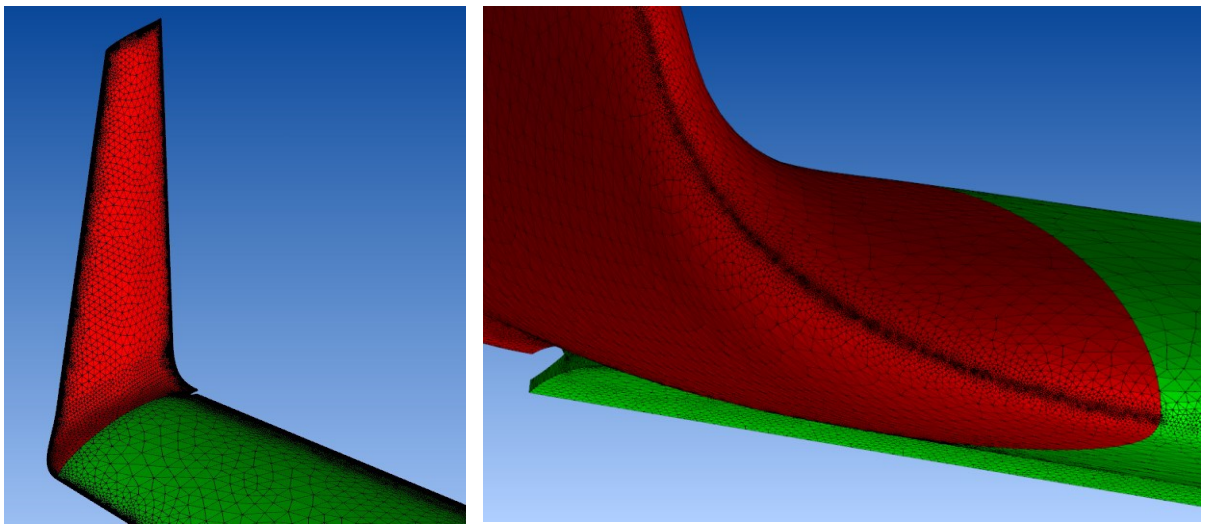

Fig. 9.10 Surface mesh of the wing and winglet

Step 2: After basic mesh creation, it was necessary to improve mesh quality. This step was done by global mesh smoothing with following parameters.

Smooth Mesh Globally	
Smoothing iterations	15
Up to value	0.5
Criterion	Quality
Smooth Mesh Type	TETRA_4: Smooth
	TRI_3: Smooth
Smooth Parts / Subset	All parts
Advanced Options	Not just worst 1%: Enabled
	Allow node merging: Enabled
	Prism Warpage Ratio: 0.5

Tab. 9.8 Meshing process step 2 parameters

Step 3: Mesh was checked for defects using default settings of ICEM CFD.

Step 4: Prism mesh was created to obtain mesh for boundary layer simulation. In this step, two prismatic layers with settings defined in tab. 9.6 was extruded. Existing mesh was defined as the input mesh and Wing and Winglet parts was defined as the parts for prismatic layers extrusion.

Step 5: In this step, the innermost layer (numbered as 0) was split to 5 layers with equal height. Settings in the ICEM CFD software was following.

Split Mesh	
Prism Surface Parts	Wing, Winglet
Prism Volume Parts	Live
Split Prisms	Method: Fix ratio
	Prism ratio: 1.0
	Number of layers: 5
	Split only specified layers: Enabled
	Layer numbers: 0
	Allow node merging: Enabled
	Prism Warpage Ratio: 0.5

Tab. 9.9 Meshing process step 5 parameters

Step 6: Identical to the step 5 excluding the number of layer for split operation. In this step, layer number 5 was split. Number of layers parameter was also 5 as in the step 5. After completion of step 6, total number of prism layers was 10 and they were equally thick.

Step 7: To properly simulate boundary layer, the prism layers height has to be redistributed to enable proper simulation of velocity gradient near the surfaces of the wing and winglet. For the proper height redistribution, the dimensionless wall distance value, also designated as Y+ value has to be properly chosen and initial layer height has to be computed. Value of the dimensionless wall distance could be determined using following equations.

$$Y^+ = \frac{u_* \cdot y}{\nu} \qquad \text{[13] (9.1)}$$

Where u_* is friction velocity at the nearest wall, y is the distance to the nearest wall and ν is the local kinematic viscosity of the fluid. Friction velocity at the nearest wall could be calculated using: [13]

$$u_* = \sqrt{\frac{\tau_w}{\rho}} \qquad \text{[20] (9.2)}$$

Where τ_w is the wall shear stress and ρ is the fluid density at the wall. [20]

For the purposes of the initial layer height calculation, the online tool was used. [23]. Input parameters for low speed flight case and high speed case were:

Input parameter	Designation	Value	Unit
Reynolds number	Re_{+2}	1 088 403,785	-
Reference length	c_{MAC}	0,673340	m
Desired y+ value	y^+_{+2}	1	-

Tab. 9.10 Parameters for initial layer height calculation for low speed flight case

Input parameter	Designation	Value	Unit
Reynolds number	Re_{-2}	2 688 996,143	-
Reference length	c_{MAC}	0,673340	m
Desired y+ value	y^{+}_{-2}	1	-

Tab. 9.11 Parameters for initial layer height calculation for high speed flight case

Reynolds number in tables 9.10 a 9.11 was calculated based on ISA properties at sea level, c_{MAC} value and reference flight speeds which was defined by flight manual of the Ventus 2ax sailplane and which was used for all simulations.

Wingspan 15m, G = 525 kg	
Flap position [-]	Speed range [km/h]
L	75 – 90
+2, +1	85 – 105
0	110 – 140
-1	130 – 170
-2	155 – 210
S	210 – 230
S1	230 – 270

Tab. 9.12 Dependency of the recommended flight speed range on the flap position

Speeds which was chosen for the further CFD investigations are:

$$V_{+2} = 85\ km/h \tag{9.3}$$

For the low speed flight case with flap deflected to +2 position. And:

$$V_{-2} = 210\ km/h \tag{9.4}$$

For the high speed flight case with flap deflected to -2 position.

Finally, after the calculation was finished, initial layer heights of the first prism layers has following values:

$$ds_{+2} = 0{,}0145\ mm \tag{9.5}$$

For the low speed flight case with flap deflected to +2 position. And:

$$ds_{-2} = 0{,}0063\ mm \tag{9.6}$$

For the high speed flight case with flap deflected to -2 position.

Shape of the prism layers distribution could be seen in the figure 9.10 below:

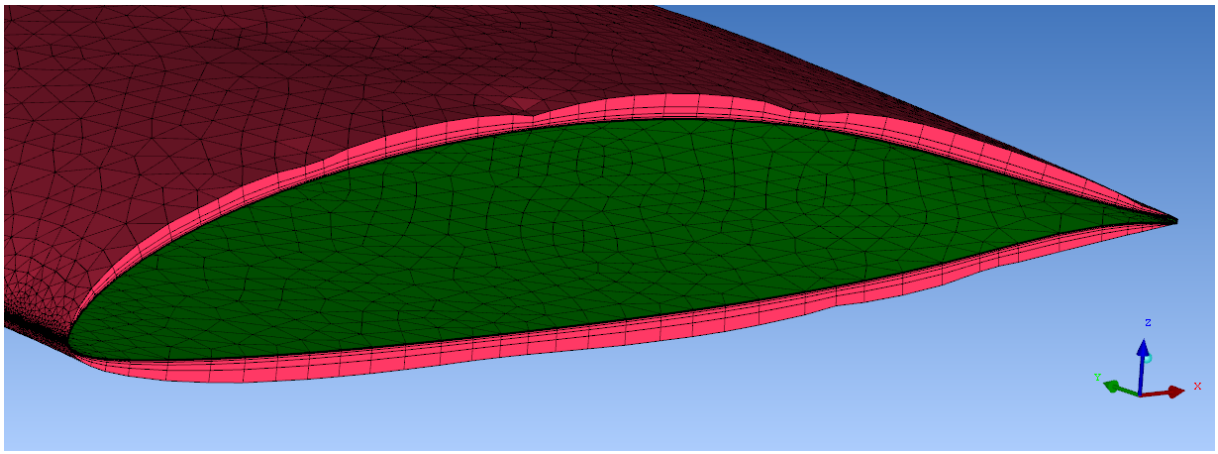

Fig. 9.10 Prism layers (red) height distribution

Step 8: Global smoothing of mesh with following parameters.

Smooth Mesh Globally	
Smoothing iterations	10
Up to value	0.5
Criterion	Quality
Smooth Mesh Type	TETRA_4: Smooth
	TRI_3: Freeze
	PENTA_5: Freeze
	QUAD_4: Freeze
Smooth Parts / Subset	All parts
Advanced Options	Not just worst 1%: Enabled
	Allow node merging: Enabled
	Prism Warpage Ratio: 0.5

Tab. 9.13 Mesh process step 8 parameters

Step 9: Mesh was checked for defects and unconnected vertices

Step 10: Global smoothing of the mesh with following parameters.

Smooth Mesh Globally	
Smoothing iterations	2
Up to value	0.01
Criterion	Quality
Smooth Mesh Type	TETRA_4: Smooth
	TRI_3: Smooth
	PENTA_5: Smooth
	QUAD_4: Smooth
Smooth Parts / Subset	All parts
Advanced Options	Not just worst 1%: Enabled
	Allow node merging: Enabled
	Prism Warpage Ratio: 0.5

Tab. 9.14 Mesh process step 10 parameters

Step 11: Final mesh check after last global smoothing.

Step 12: After all above mentioned steps, the mesh is almost ready to export to the Fluent format. Few additional parameters must be defined. Especially, the solver type was set to the Fluent type. Boundary conditions were set to the following values.

Boundary Conditions	
Part Name	Boundary Condition
Wing	Wall
Winglet	Wall
Symmetry Plane	Symmetry
Pressure Far Field	Pressure-far-field
Live	Fluid

Tab. 9.14 Meshing process Step 12 parameters

9.5 Solver settings

Important part of the CFD pre-processing is the solver settings. CFD solver used during work on this thesis was ANSYS Fluent. This chapter describes, step by step, the settings used for the simulations. For the clarity, an overview of the solver settings is showed in the table 9.15 and detailed description is below it.

Solution setup		
Solver	Type: Density-Based	
	Velocity formulation: Absolute	
	Time: Steady	
Models	Multiphase: Off	
	Energy: On	
	Viscous: Spalart-Allmaras	Vorticity-Based
	Radiation: Off	
	Heat Exchanger: Off	
	Species: Off	
	Discrete Phase: Off	
	Acoustics: Off	
Materials	Fluid: Air	Density: Ideal-gas
		Cp: 1006.43 $Jkg^{-1}K^{-1}$
		Thermal Conductivity: 0.0242 $Wm^{-1}K^{-1}$
		Viscosity: Sutherland – Three coefficient method
		Molecular Weight: 28.966
	Solid: Aluminium	
Cell Zone Conditions	live	Operating Conditions → Operating Pressure: 0 Pa
Boundary Conditions	int_live	Type: Interior
	pressure_far_field	Type: pressure-far-field
		Gauge Pressure: 101325 Pa
		Mach number: 0.06938526 (+2) / 0.1714224 (-2)
		Coordinate system: Cartesian (X, Y, Z)
		X-component of Flow Direction: 0.9876883 (+2) / 0.9998415 (-2)
		Y-component of Flow Direction: 0
		Z-component of Flow Direction: 0.1564345 (+2) / 0.01780142 (-2)
		Turbulence Specification Method: Intensity and Length Scale
		Turbulent Intensity (%): 0.1
		Turbulent Length Scale: 0.02
		Temperature: 288.15 K
	symmetry_plane	Type: symmetry

	wing	Type: wall
	winglet	Type: wall
Reference Values	Compute from: pressure_far_field	Area: 4.827081 m^2
		Density: 1.225 $kg \cdot m^{-3}$
		Enthalpy: 290281 $J \cdot kg^{-1}$
		Length: 0.6733404 m
		Pressure: 101325 Pa
		Temperature: 288.15 K
		Velocity: 23.611 $m \cdot s^{-1}$ (+2) / 58.333 $m \cdot s^{-1}$ (-2)
		Viscosity: $1.7894 \cdot 10^{-5}$ $kg \cdot m^{-1} \cdot s^{-1}$
		Ratio of Specific Heats: 1.4

Tab. 9.15 ANSYS Fluent settings – Solution Setup

Solution		
Solution Methods	Formulation: Implicit	
	Flux Type: Roe-FDS	
	Spatial Discretization	Gradient: Least Squares Cell Based
		Flow: Second Order Upwind
		Modified Turbulent Viscosity: Second Order Upwind
Solution Controls	Courant Number: 5	
	Under-Relaxation Factors	Modified Turbulent Viscosity: 0.8
		Turbulent Viscosity: 1
		Solid: 1
Solution Initialization	Initialization Methods: Standard Initialization	
	Compute from: pressure_far_field	
	Reference Frame: Relative to Cell Zone	
	Initial Values	Gauge Pressure: 101325 Pa
		X Vleocity: 23.31174m/s (+2) / 58.30267m/s (-2)
		Y Velocity: 0 m/s (+2) / 0 m/s (-2)
		Z Velocity: 3.692212m/s (+2) / 1.038029m/s (-2)
		Modified Turbulent Viscosity: 0.0005781364 m^2/s (+2) / 0.001428343 m^2/s (-2)
		Temperature: 288.15 K

Tab. 9.16 ANSYS Fluent settings – Solution

One of the main parameters, which was chosen during Ansys Fluent settings was the model. In this case, Spalart-Allmaras viscous model was chosen.

Usage of Spalart-Allmaras model is beneficious for multiple reasons. Firstly, the Spalart-Allmaras model does not use wall function and solves the entire flow field, which means higher precision boundary layer modelling in case, the prismatic layers was created properly during meshing process. Another advantage of the model is, that it utilizes only one transport equation and adding one variable called modified turbulent kinematic viscosity designated $\tilde{\nu}$. This makes the model relatively low memory-intensive. All above mentioned aspects speaks for the usage of this turbulent model. From the low computational requirement point of view, the model is well suited for the initial exploration in the field of the winglet optimisation as numerous cases must be simulated as could be seen in the chapter 10 of this thesis.

Operating pressure was set to the value of 0 Pa and gauge pressure to the value of 101325 Pa, which corresponds to the atmospheric pressure at the sea level in the ISA model. Absolute pressure in the flow is calculated as the sum of the operating and gauge pressure as given by eqn. 9.7.

$$p_{abs} = p_{op} + p_{gauge} \qquad [19]\ (9.6)$$

Where p_{abs} is the absolute pressure of the flow, p_{op} is the actual operating pressure and p_{gauge} is the gauge pressure.

Mach numbers of the flow for the low speed case with positive flap at +2 deflection and high speed case with -2 flap deflection was calculated based on the actual flight speed mentioned in the table 9.15 and the speed of sound at the sea level of the ISA.

$$M = \frac{\mathrm{v}}{a} \qquad (9.7)$$

Where the speed of sound is:

$$a = 340{,}29\ ms^{-1} \qquad (9.8)$$

ANSYS Fluent is unable to use input of angle of attack in the angular value. Angle of attack input is done by the transforming flow to the directions of the coordinate system axes. X component of velocity is defined as:

$$V_x = V \cdot \cos\alpha \qquad (9.9)$$

And Z component is defined by:

$$V_z = V \cdot \sin\alpha \qquad (9.10)$$

Angle of attack for the low speed case was defined as:

$$\alpha_{+2} = 9° \qquad (9.11)$$

Angle of attack for the high speed case was defined as:

$$\alpha_{-2} = 1{,}02° \qquad (9.12)$$

Angle of attack for both cases was determined by the analysis of the wing at given speeds in the XFLR 5 software. Detailed description of the process is not part of this thesis. However, principle of angle of attack determination puts emphasis on the achieving of lift corresponding to the maximum gross weight of 525 kg.

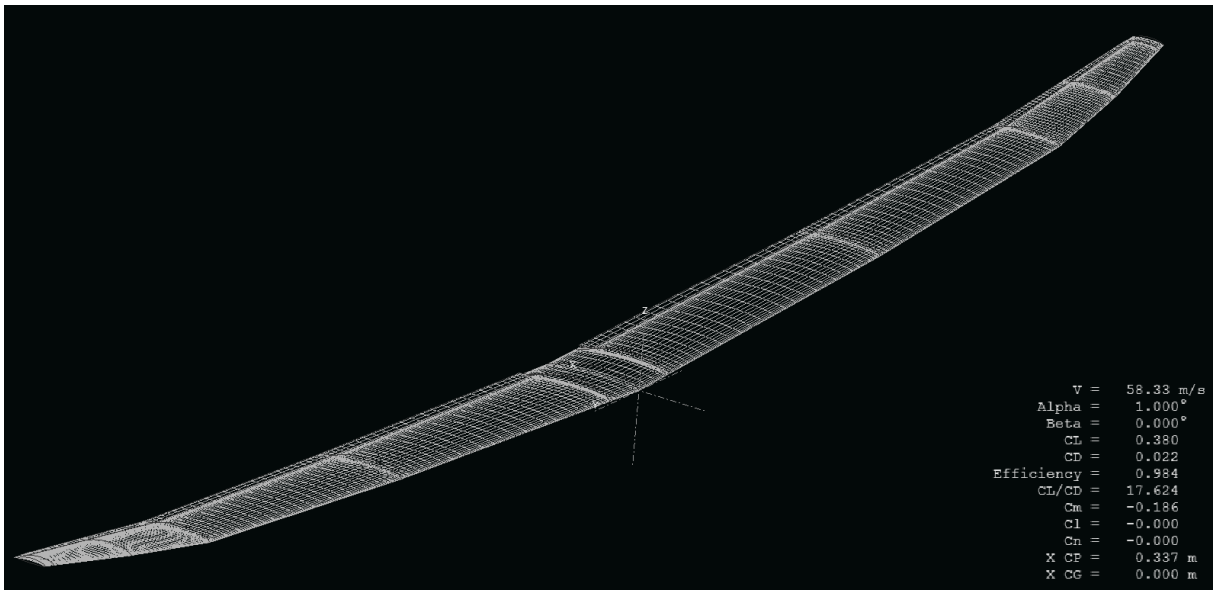

Fig. 9.11 Wing geometry (XFLR5) used for angle of attack determination

Turbulence intensity was set to the value of 0.1 %. Turbulence intensity I is defined as the root mean square of the velocity fluctuations u' to the mean flow velocity u_{avg}. [18]

$$I = \frac{u'}{u_{avg}} \qquad \text{[18] (9.13)}$$

As the measure, turbulence intensity of 0.05% should be expected in modern low-turbulence wind tunnels. [-] Value of turbulence intensity of 0.1% was chosen with respect to [8].

Turbulence length scale value was set to value 0.02. Turbulent length scale is a physical quantity related to the size of the large eddies that contain the energy in the turbulent flow. [18]

9.6 Mesh dependency study

To determine optimal number of elements of the mesh, mesh dependency study was performed. Mesh dependency study was done only for the low speed case with positive flap deflection. In total, five different meshes was created with different element sizes and then evaluated for the lift and drag coefficient values. Dependency of the coefficient values on the number of mesh elements was evaluated and optimal meshing parameters was determined.

Mesh parameters for five different meshes are mentioned in the table 9.17 below.

	Mesh designation	A	B	C	D	E
Surface number	Description	Max size	Max size	Max size	Max size	Max size
1	Wing upper and lower surface	25	31	37,5	43,75	50
2	Flaps upper and lower surface	15	18,5	22,5	26,25	30
3	Surfaces of dihedral angle change	10	12,5	15	17,5	20
4	Wing to flap transition surfaces	6	7,5	9	10,5	12
5	Wing to winglet junction	5	6,25	7,5	8,75	10
6	Winglet upper and lower surface	10	12,5	15	17,5	20
7	Tip surface of the winglet	2	2,5	3	3,5	4
-	Winglet trailing edge	1	1	1	1	1
-	Wing trailing edge	2	2	2	2	2
-	End surfaces of the flaps	2	2	2	2	2
-	Additional geom. elements	0,5	0,5	0,5	0,5	0,5

Tab. 9.17 Surface elements sizes used for mesh dependency study meshes

Leading edge densities has also different values. Values of leading edge densities settings are mentioned below.

Mesh	Region	Size	Ratio	Width
A	Wing leading edge	0.2	0	1
	Winglet leading edge	0.4	0	1
B	Wing leading edge	0.25	0	1
	Winglet leading edge	0.5	0	1
C	Wing leading edge	0.3	0	1
	Winglet leading edge	0.6	0	1
D	Wing leading edge	0.35	0	1
	Winglet leading edge	0.7	0	1
E	Wing leading edge	0.4	0	1
	Winglet leading edge	0.8	0	1

Tab. 9.18 Leading edge densities settings

Global element size was set to 4096 and scaling factor was used to make different global mesh. Scaling factors was set to following values.

Mesh designation	A	B	C	D	E
Scaling factor	1.00	1.25	1.50	1.75	2.00

Tab. 9.19 Scaling factor settings

After individual meshes was created, simulations were performed with solver settings for the low speed flight case with +2 flap deflection. All meshes converged with oscillations lower than 0.01% in lift and drag coefficients after 10 000 iterations. Convergence of lift coefficient and drag coefficient for mesh designated by letter C is shown in figure 9.12 and 9.13 respectively.

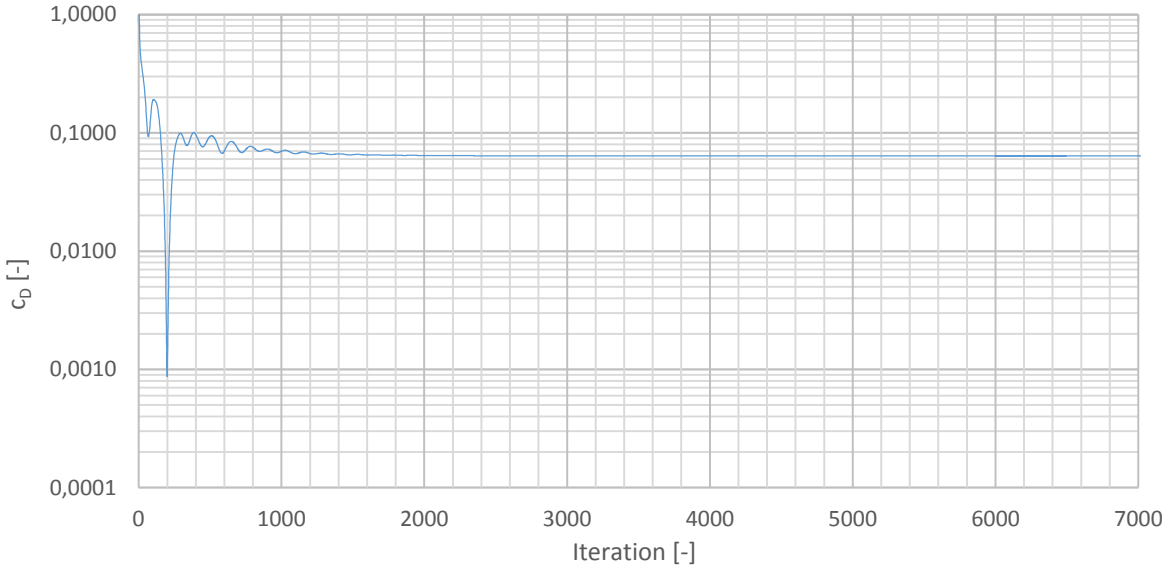

Fig. 9.12 Drag coefficient convergence for mesh C

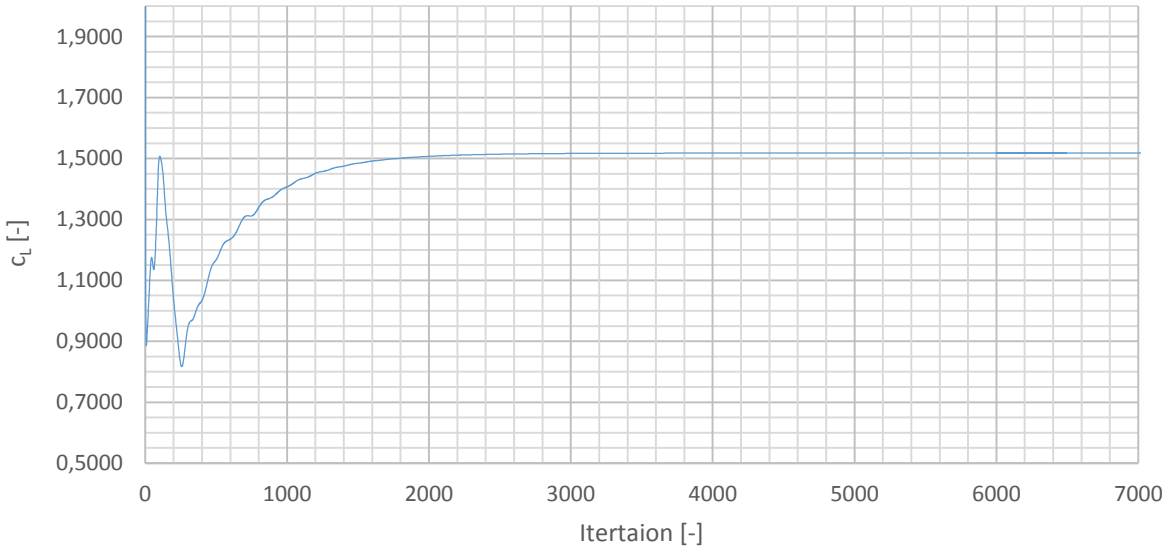

Fig. 9.12 Lift coefficient convergence for mesh C

After simulations was post-processed, lift and drag coefficient data for individual meshes were extracted and evaluated. All data are written in the table 9.20.

Lift coefficient			
Mesh	Elements	Value	Slope
A	21 269 200	1,53435	
B	16 157 993	1,52282	2,25526 E-09
C	14 437 767	1,51785	2,88863 E-09
D	13 272 981	1,51145	5,49682 E-90
E	7 704 673	1,48698	4,39427 E-09
Drag coefficient			
Mesh	Elements	Value	Slope
A	21 269 200	0,0634139	
B	16 157 993	0,0635795	-3,24034 E-11
C	14 437 767	0,0637081	-7,47231 E-11
D	13 272 981	0,0638855	-15,23250 E-11
E	7 704 673	0,0654761	-28,56511 E-11
Lift to Drag ratio			
Mesh	Elements	Value	Slope
A	21 269 200	24,196	
B	16 157 993	23,951	4,78029 E-08
C	14 437 767	23,852	7,34343 E-08
D	13 272 981	23,659	14,28489 E-08
E	7 704 673	22,710	17,03278 E-08

Tab. 9.20 Mesh dependency study evaluation

Results mentioned in the table 9.20 is graphically expressed in the figures 9.13 through 9.15 below.

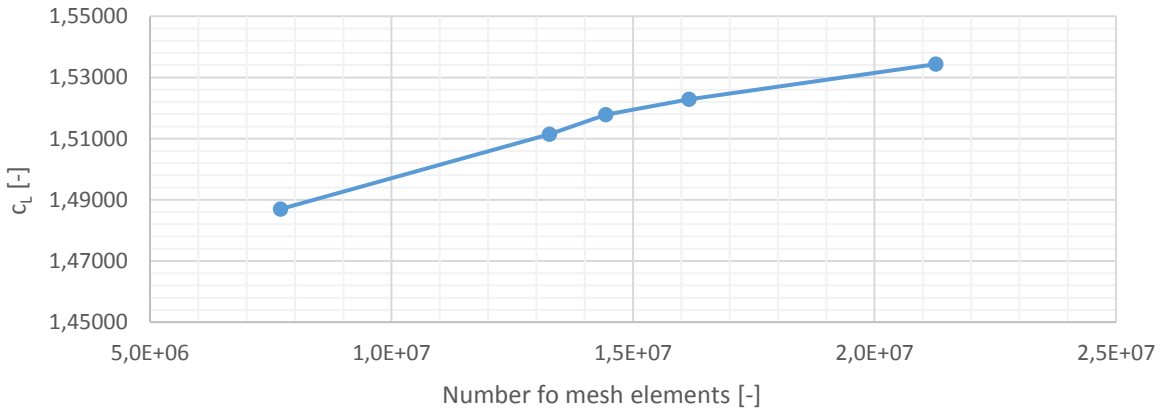

Fig. 9.13 Lift coefficient dependency on number of mesh elements

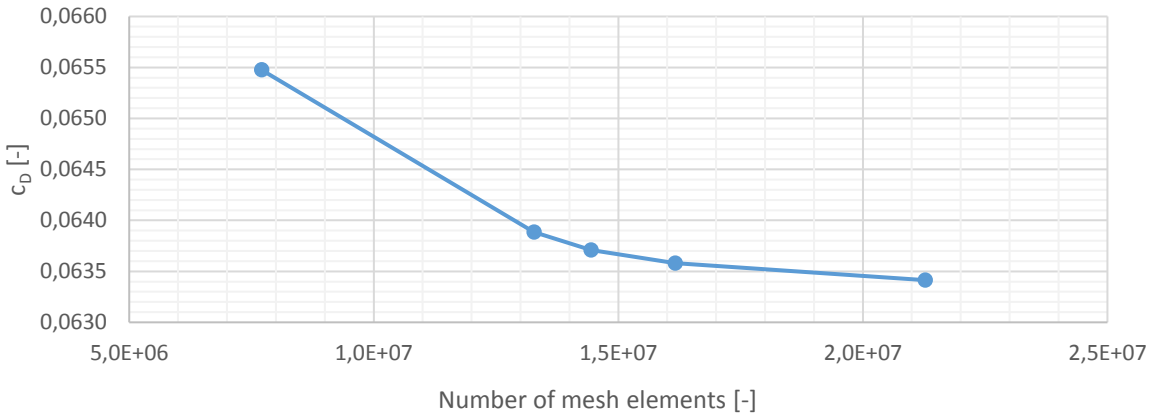

Fig. 9.14 Drag coefficient dependency on number of mesh elements

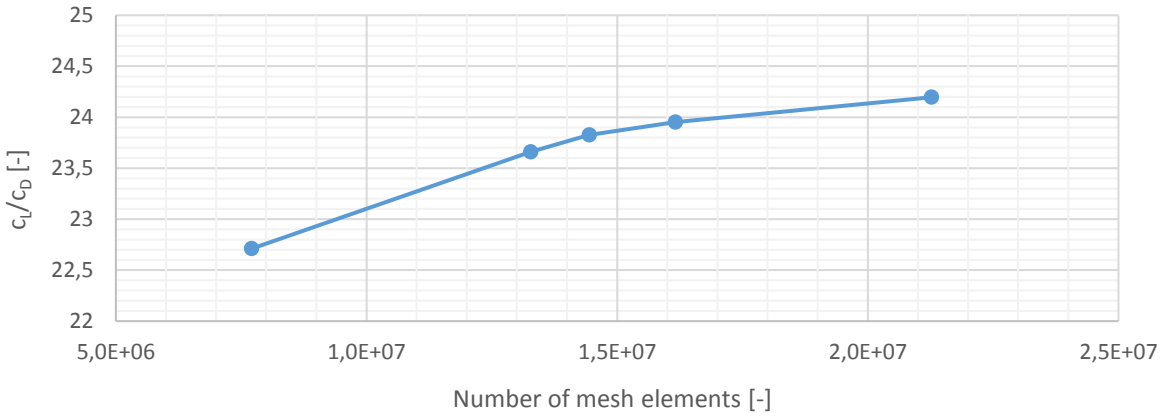

Fig. 9.15 Glide ratio dependency on number of mesh elements

The slope parameter mentioned in table 9.20 was calculated using following equation:

$$slope = \frac{value_{i+1} - value_i}{elements_{i+1} - elements_i} \tag{9.14}$$

Where $value$ stands for the value of aerodynamic characteristic as lift coefficient, drag coefficient or glide ratio and $elements$ stand for the number of mesh elements.

It is apparent from the figures 9.13 through 9.15, that slope of the parameter dependency on number of mesh elements is lower for number of elements above 15 to 16 million. Values still changing, but to the lesser extent. It will be beneficious to use more than 16 million elements in the final meshes used for optimisation, but due to large number of cases, which were studied, the computational effort would be enormous. Due to this fact and fact, that cases were evaluated compared to the reference one, mesh chosen for further use on all cases was mesh designated by letter C. It was of the major interest to achieve meshes with least possible deviation from the reference one in the number of cells point of view. However, final chosen mesh C was slightly modified and some of the parameters of finer mesh B were incorporated. Final settings of the mesh are mentioned in the chapter 9.3.

9.7 Reference cases evaluation

After all pre-processing mentioned above, reference cases simulations taken place. ICEM CFD meshing settings and process for all cases used for optimisation including reference one and ANSYS Fluent settings are mentioned in chapters 9.3 through 9.6. Reference cases are characterised by neutral winglet geometry. Geometry settings of the winglet for both reference cases are following.

Parameter	Cant angle	Toe-in angle	Tip-in angle
Designation	ϕ	γ_{wr}	γ_{wt}
Value	8,22354	-3	-1
Unit	°	°	°

Tab. 9.21 Reference case winglet geometry settings

Description of the toe-in and tip-in angles are shown in figure 3.2. Cant angle is described in figure 3.1. All other geometry parameters of the winglet are shown in figure 8.5.

After solution converged and oscillations of the monitored parameters, which are drag and lift coefficients, are low (max. 0.01% measured), the solving process was stopped and data was postprocessed.

First part of postprocessing was extraction of the aerodynamic coefficients data. During evaluation process, coefficients of lift and drag was evaluated for the whole wing and winglet assembly and for the winglet alone. Drag force of the winglet was also evaluated. For the purpose of gathering full information about the winglet geometry influence on the aerodynamic parameters of the wing with winglet, moment coefficient of the assembly was also evaluated with reference point chosen as quarter chord point of the mean aerodynamic chord and moment axis parallel with Y axis of the wing. Another parameter, which were evaluated was pressure drag coefficient and viscous drag coefficient. From above mentioned coefficients, lift to drag ratio and third power of lift squared to the drag ratio was evaluated. All parameters are mentioned in the table below.

Wing and winglet			
Lift coefficient	c_L	1,51968	-
Drag coefficient	c_D	0,06311	-
Moment coefficient	c_M	-0,16500	-
Pressure drag coefficient	c_{Dp}	0,05399	-
Viscous drag coefficient	c_{Dv}	0,00912	-
Lift to Drag ratio	c_L / c_D	24,07937	-
Ratio of pressure drag to total drag	$(c_{Dp} / c_D) \cdot 100$	85,55024	%
Ratio of viscous drag to total drag	$(c_{Dv} / c_D) \cdot 100$	14,44976	%
Winglet			
Lift coefficient	c_{Lw}	0,00674	-
Drag coefficient	c_{Dw}	-0,00093	-
Drag	D_w	-1,53237	N

Tab. 9.22 Values of aerodynamic characteristics for low speed flight case (85 km/h ; +2)

Wing and winglet			
Lift coefficient	c_L	0,25038	-
Drag coefficient	c_D	0,00017	-
Moment coefficient	c_M	-0,04647	-
Pressure drag coefficient	c_{Dp}	0,00560	-
Viscous drag coefficient	c_{Dv}	0,00843	-
Lift to Drag ratio	c_L / c_D	17,84844	-
Ratio of pressure drag to total drag	$(c_{Dp} / c_D) \cdot 100$	39,92474	%
Ratio of viscous drag to total drag	$(c_{Dv} / c_D) \cdot 100$	60,07526	%
Winglet			
Lift coefficient	c_{Lw}	0,00017	-
Drag coefficient	c_{Dw}	0,00156	-
Drag	D_w	1,72732	N

Tab. 9.23 Values of aerodynamic characteristics for high speed flight case (210 km/h ; -2)

From the above-mentioned tables 9.22 and 9.23, aerodynamic characteristics of reference cases for low speed case and for high speed case are apparent. One significant parameter should be mentioned. It is obvious, that with increasing speed of flight, ratio of the pressure drag to the overall drag is decreasing and winglet drag force increasing. Pressure drag decreases due to the lower angle of attack of the wing and incorporated redistribution of pressure coefficient values along the wing airfoil surfaces while the winglet drag increases due to lower intensity of the wing tip vortices which is connected to the decrease in the winglet airfoils angle of attack.

Important aspect to be noticed, is low values of lift to drag ratio in both flight regimes. This aspect could be explained by the spalart-allmaras turbulent model use in solving the case sensitive to the laminar to turbulent boundary layer transition, which the glider wing CFD simulation is. Consideration of the transition model use instead of the fully turbulent should be recommended if the more detailed simulation model will be created based on the results of this thesis. However, for the optimisation from the comparative point of view, spalart-allmaras fully turbulent model is sufficient and improvements of wing and winglet assembly performance should be revealed. Underestimation of the performance in case of fully turbulent model usage instead of transition model is well described by the following figure 9.16, which describes speed polar of Standard Cirrus sailplane.

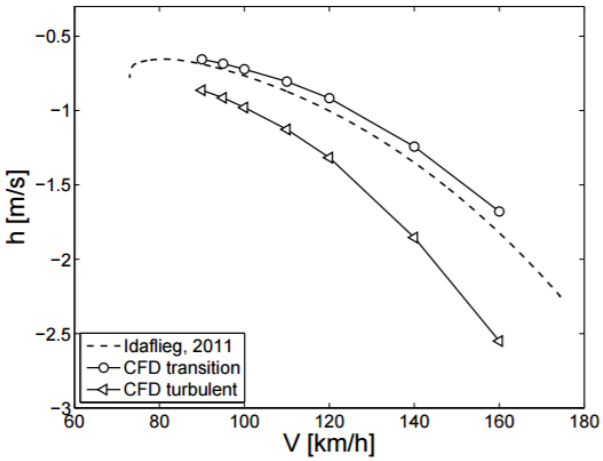

Fig. 9.16 Speed polar of Std. Cirrus sailplane (measured, CFD turbulent, CFD transition)

For the visualisation of the flow in the wing and winglet vicinity, the modified turbulent viscosity of the flow 0.005m above surface and pressure coefficients over the surfaces were used. Modified turbulent viscosity pathlines for the low speed case is showed in the figures 9.17 through 9.19 below. Other visualisations are part of the appendices.

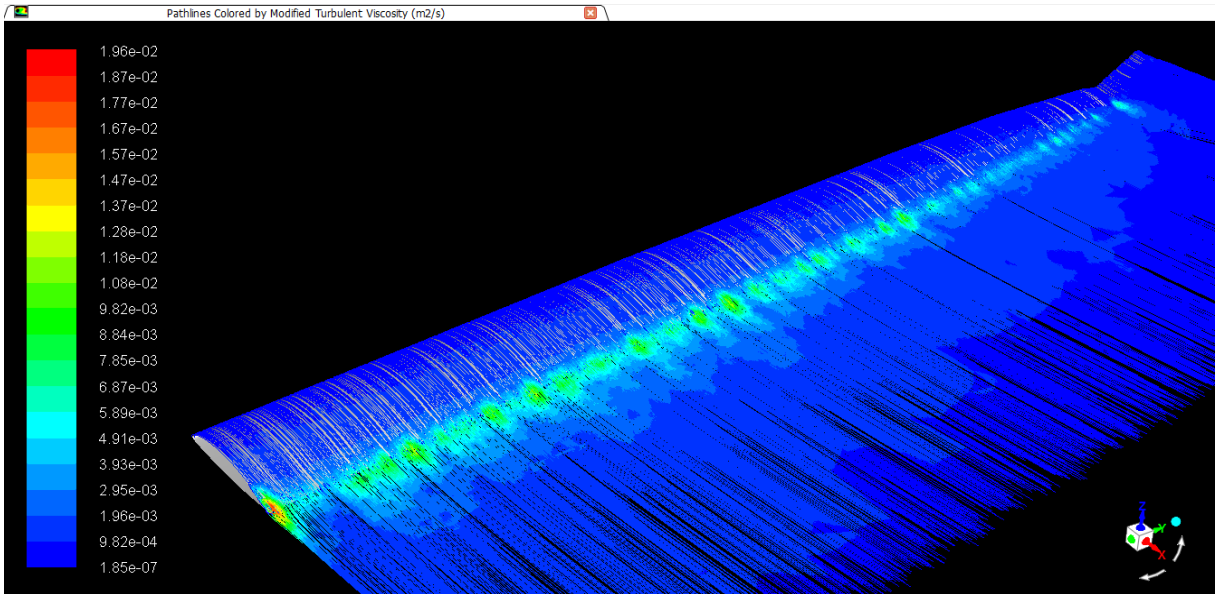

Fig. 9.17 Modified turbulent viscosity pathlines in the wing vicinity (low speed case)

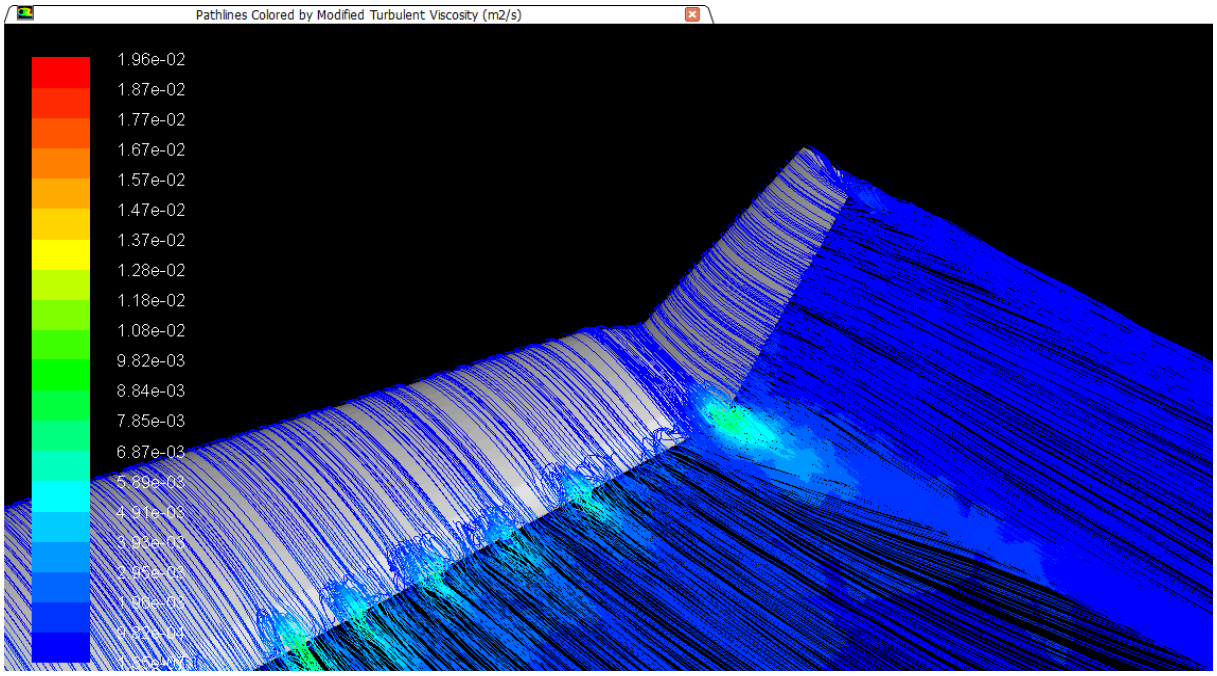

Fig. 9.18 Modified turbulent viscosity pathlines detail of the wing and winglet (low speed case)

Investigation of the modified turbulent viscosity pathlines in the case of low speed flight with flap deflected to +2 position revealed, that flow at the upper side of flap is strongly turbulent, which could lead to the conclusion, that wing is near the critical angle of attack. At the speed of 85 km/h and lift coefficient 1,51968, the aircraft actual weight was computed from the lift force and gravity force of the aircraft. Actual weight of the aircraft evaluated from the reference case is 510,840 kg, which is close to the maximum gross weight. It is obvious, that this flight regime is really the low extreme of the flight speed with the flap setting +2.

Another significant characteristic of the reference low speed case is large region with high turbulence near the upper surface of the wing to winglet junction trailing edge. Situation in this region should be explained by the assuming of the pressure field characteristic. At the high angle of attack of 9 degrees, the pressure gradient over the top surface of the wing is adverse and flow has tendency to decelerate, and air flow is in the direction of the increasing pressure.

$$\frac{\partial p}{\partial x} > 0 \tag{9.15}$$

When this aspect is taken to account together with reality, that situation is same at the upper side of the winglet, the flow deceleration is stronger than in case of the normal wingtip without winglet. This phenomenon could be also explained by the increased boundary layer thickness in the wing to winglet junction upper side region.

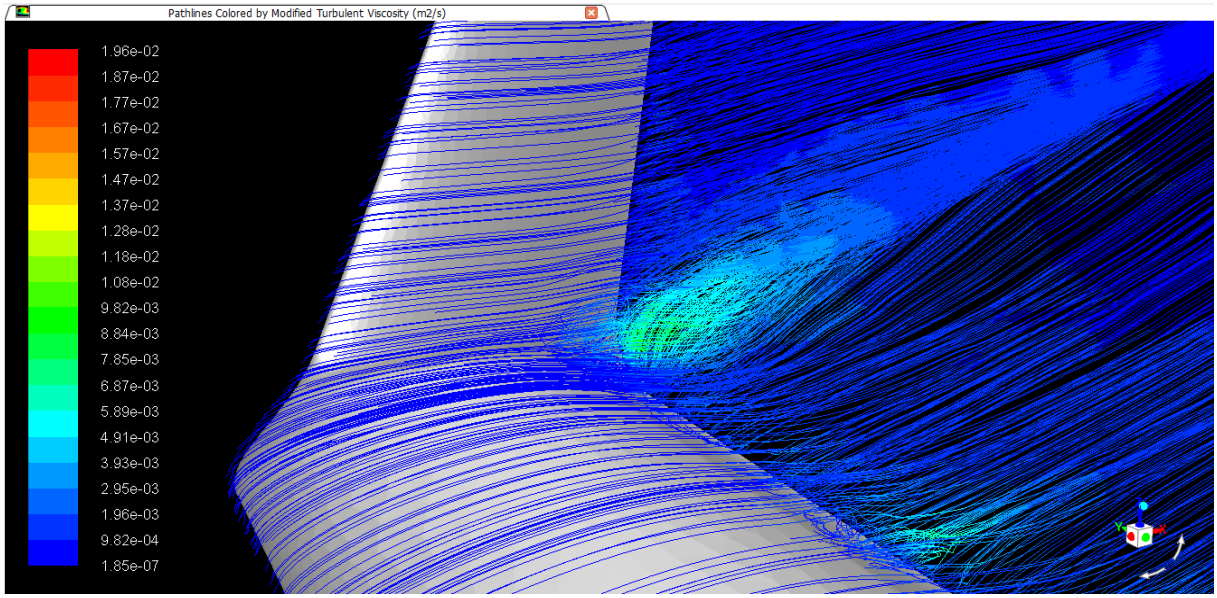

Fig. 9.19 Modified turbulent viscosity pathlines detail of wing to winglet junction (low speed case)

Visualisations of the high speed case with flap settings -2 is mentioned below.

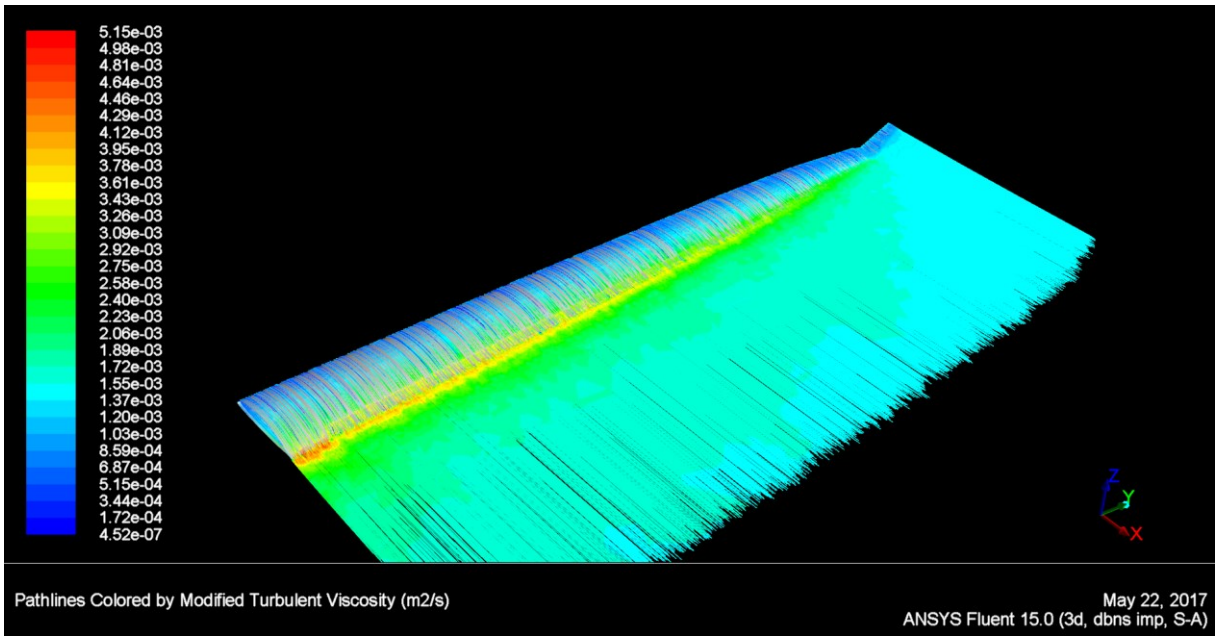

Fig. 9.20 Modified turbulent viscosity pathlines in the wing vicinity (high speed case)

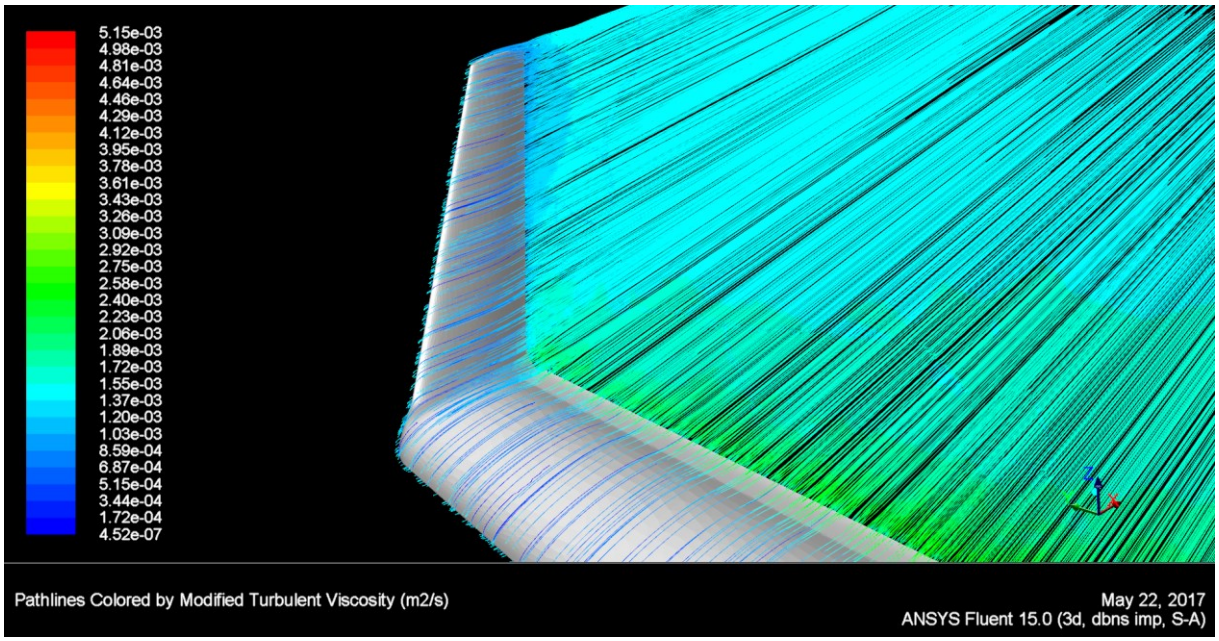

Fig. 9.21 Modified turbulent viscosity pathlines detail of the wing and winglet (high speed case)

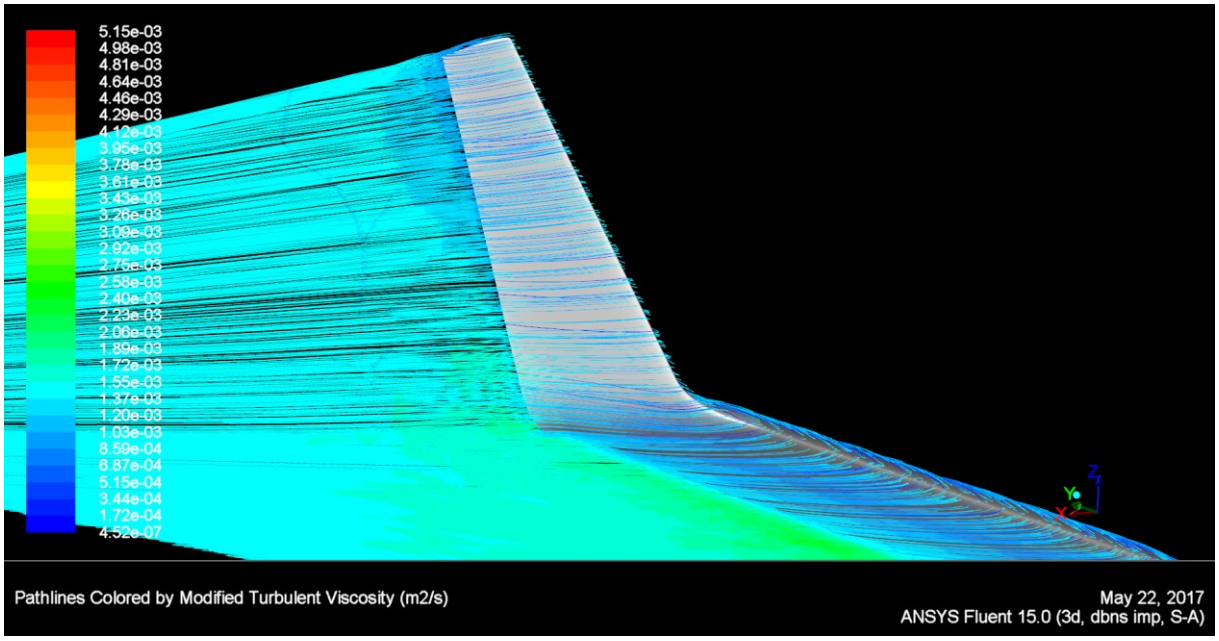

Fig. 9.22 Modified turbulent viscosity pathlines detail of wing to winglet junction (high speed case)

From the figures 9.20 through 9.22, characteristics of the flow in the vicinity of the wing and winglet for the high-speed flight case are obvious. Modified turbulence viscosity peaks are lower than in the low speed case which indicates, that the flow is not separated and turbulence level is lower. Turbulent viscosity peaks are present right behind the trailing edge of the flap on most of the wingspan. Higher turbulent viscosity is observed near the symmetry plane of the wing. Another characteristic aspect of high speed case is attached flow without the high turbulent viscosity values in the wing to winglet junction region which is caused by the higher flight speed and thus the lower angle of attack and lower values of adverse pressure gradient in the area.

Above mentioned results of the reference cases simulations were used as the comparative basis for the cases which were simulated during optimisation, which will be described in the next chapter.

10 OPTIMISATION PROCESS

Searching for the optimal geometry of the winglet for low and high speed cases was done using Response Surface Method (RSM) optimisation process. Key steps of the process are mentioned in the chapter. 4.1 and good description of the process is provided by figure 4.1.

10.1 Design of experiments

First step of the process is definition of the cases to be evaluated to build database of the solutions needed for Response Surface creation. Definition of the cases should not be random. Methodologies exists for the systematic generation of the cases for the databases creation. In case of winglet shape optimisation, the Central Composite Design method was used.

Principle of Central Composite Design lays in the creation of the design cases based on the reference design, but with modifications. Number of modified designs depends on the number of parameters, that should be optimised. For number of parameters less than 5, the full factorial design should be used. Even before, the full factorial design process for deriving of modified cases will be performed, parameters and their range should be defined.

Parameters chosen for optimisation are cant angle, toe-in and tip-in angles of the winglet. The reference case was taken as the middle position and the low and high positions are symmetrical to the reference one. Toe-in angle and tip-in angle values are taken as the absolute, but cant angle parameter is transformed and only deviation from the neutral position is subjected to optimisation. Values ranges of each parameter are shown in the table below.

Designation in CCD	Parameter	Designation	Low value	Reference value	High value
ξ_1	Delta cant	$\Delta\phi$	-10	0	10
ξ_2	Toe-in	γ_{wr}	-6	-3	0
ξ_3	Tip-in	γ_{wt}	-4	-1	2

Tab. 10.1 Ranges of deign parameters

Delta cant value is positive, when winglet cant angle increases, or in other words when the tip of winglet moves outwards.

When design parameters range are set, next step is to define values of parameters for each case derived from the reference one. For this purpose, the Full Factorial Central Composite Design was used. Each parameter (ξ_1 to ξ_3) which will be further called natural variable, is coded to the coded variable (X_1 to X_3). Low value of natural variable is coded to the coded variable value -1 and opposite to that, the high value of natural variable is transferred to the +1 value of coded variable. Reference value of natural variable has value 0 when coded.

Combinations of coded variables values are defined by the type of Central Composite Design used. Three types of Central Composite Designs are mentioned in the table 10.2.

Graphic expression	Description
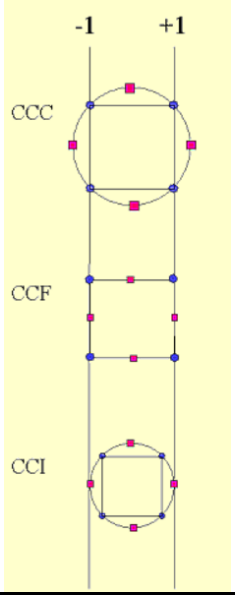	CCC (Circumscribed) is the form of central composite design in which the star points (red points) are at distance from the centre point (reference value) equal as the corner of the high and low values (blue points). On the left, the situation of two parameters CCC design is displayed. Distance from centre point to star points is equal to the $\sqrt{2}$.
	CCF (Face Centered) has star point at the center of each face of the factorial space.
	CCI (Inscribed) This design is useful when the low and high values are real limits of the parameters which may not be exceeded. 3 levels of each factor are required. CCI design is in fact CCC scaled down by the factor α which was mentioned above as $\sqrt{2}$ for the 2 parameters CCC.

Tab. 10.2 Types of Central Composite Designs [14]

CCC design was chosen for optimisation of winglet geometry for both, high and low speed, cases. For 3 parameters, the design space has form of the cube at which corners, high and low value points are placed. This cube is surrounded by the spherical surface at which, the star points lays. As this is defined, the full factorial design table could be created. For 3 parameters, number of design points are 8 corner points, 6 star points and finally 1 center point which belongs to the reference case.

RUN	Natural variables			Coded variables		
	Delta cant	Toe-in	Tip-in			
	ξ_1 [°]	ξ_2 [°]	ξ_3 [°]	X1 [−]	X2 [−]	X3 [−]
1	10	0	2	1	1	1
2	10	0	-4	1	1	-1
3	10	-6	2	1	-1	1
4	10	-6	-4	1	-1	-1
5	-10	0	2	-1	1	1
6	-10	0	-4	-1	1	-1
7	-10	-6	2	-1	-1	1
8	-10	-6	-4	-1	-1	-1
9	0	-3	-1	0	0	0
10	17,32051	0	0	1,73205	0	0
11	-17,32051	0	0	-1,73205	0	0
12	0	2,19615	0	0	1,73205	0
13	0	-8,19615	0	0	-1,73205	0
14	0	0	4,19615	0	0	1,73205
15	0	0	-6,19615	0	0	-1,73205

Tab. 10.3 Natural and design variables table

Relation between design and natural variables are defined by following equation.

$$x_i = \frac{\xi_i - \left(\frac{\xi_{imax} + \xi_{imin}}{2}\right)}{\left(\frac{\xi_{imax} - \xi_{imin}}{2}\right)}; i = 1,2,3 \dots k \tag{10.1}$$

Where x_i is the coded variable and ξ_i is natural variable.

10.2 Evaluation of CFD results

When the design of experiments was finished, all design variants were transformed to the form of CAD model and then the meshing was done within ICEM CFD. After, meshes were imported to the ANSYS Fluent, all design cases were subjected to the simulations. Visualisations of flow was investigated and aerodynamic characteristics were evaluated. For clarity, the results are presented in tabular form.

RUN	Aerodynamic characteristics of wing and winglet assembly – low speed case								
	c_D	c_L	$\frac{c_L}{c_D}$	c_m	$\frac{c_L^{3/2}}{c_D}$	c_{Dv}	c_{Dp}	c_{Dw}	D_w
	[-]	[-]	[-]	[-]	[-]	[-]	[-]	[-]	[N]
1	0,06317	1,52756	24,18203	-0,16763	29,88767	0,00910	0,05406	-0,00062	-1,02059
2	0,06298	1,52594	24,22833	-0,16710	29,92898	0,00912	0,05386	-0,00075	-1,22852
3	0,06299	1,52450	24,20246	-0,16683	29,88295	0,00913	0,05386	-0,00094	-1,54705
4	0,06288	1,52341	24,22645	-0,16624	29,90182	0,00912	0,05376	-0,00099	-1,63230
5	0,06356	1,52091	23,92883	-0,16366	29,51032	0,00913	0,05443	-0,00074	-1,22582
6	0,06346	1,51898	23,93731	-0,16359	29,50204	0,00913	0,05433	-0,00082	-1,35543
7	0,06329	1,51057	23,86567	-0,16231	29,33217	0,00909	0,05420	-0,00106	-1,75094
8	0,06339	1,50913	23,80786	-0,16216	29,24714	0,00910	0,05429	-0,00104	-1,71787
9	0,06311	1,51968	24,07937	-0,16500	29,68387	0,00912	0,05399	-0,00093	-1,53237
10	0,06281	1,52647	24,30187	-0,16801	30,02506	0,00911	0,05371	-0,00079	-1,30756
11	0,06348	1,50903	23,77097	-0,16095	29,20091	0,00910	0,05438	-0,00093	-1,53708
12	0,06339	1,52444	24,04911	-0,16531	29,69302	0,00912	0,05427	-0,00056	-0,92658
13	0,06310	1,52087	24,10240	-0,16470	29,72399	0,00915	0,05395	-0,00105	-1,73584
14	0,06324	1,52323	24,08571	-0,16565	29,72641	0,00913	0,05411	-0,00086	-1,41360
15	0,06324	1,52220	24,07037	-0,16527	29,69738	0,00914	0,05410	-0,00096	-1,58655

Tab. 10.4 Aerodynamic characteristics for low speed cases (flap +2)

Aerodynamic characteristics mentioned above are base for the comparison of individual cases relative to the reference case (RUN 9). Comparison of the individual cases to the reference case are shown in the graphical from in the figure 10.1 through 10.3. Numerical values are mentioned in appendix 2, table A2.1.

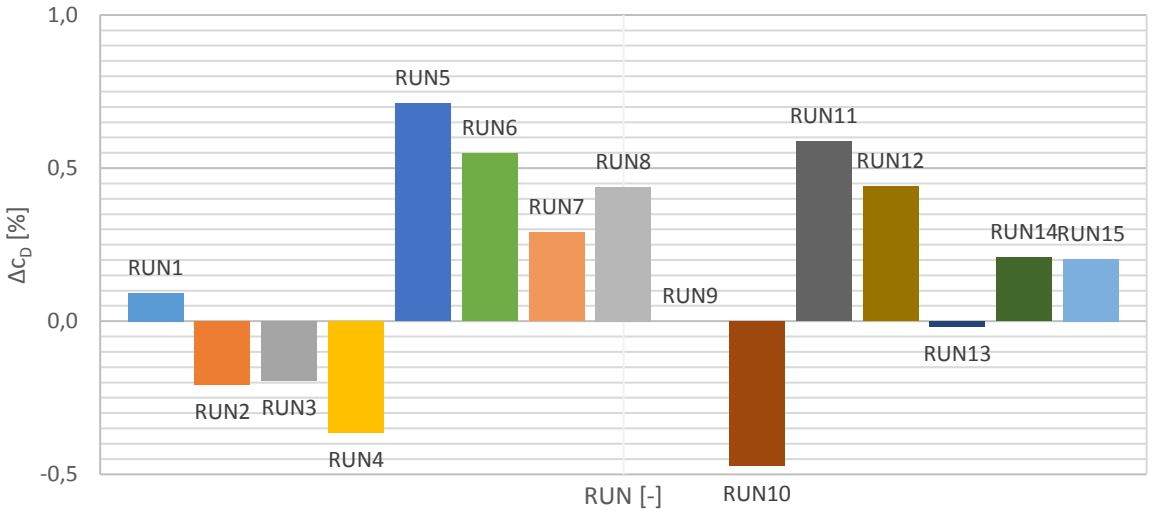

Fig. 10.1 Comparison of drag coefficient of individual cases to reference case (+2)

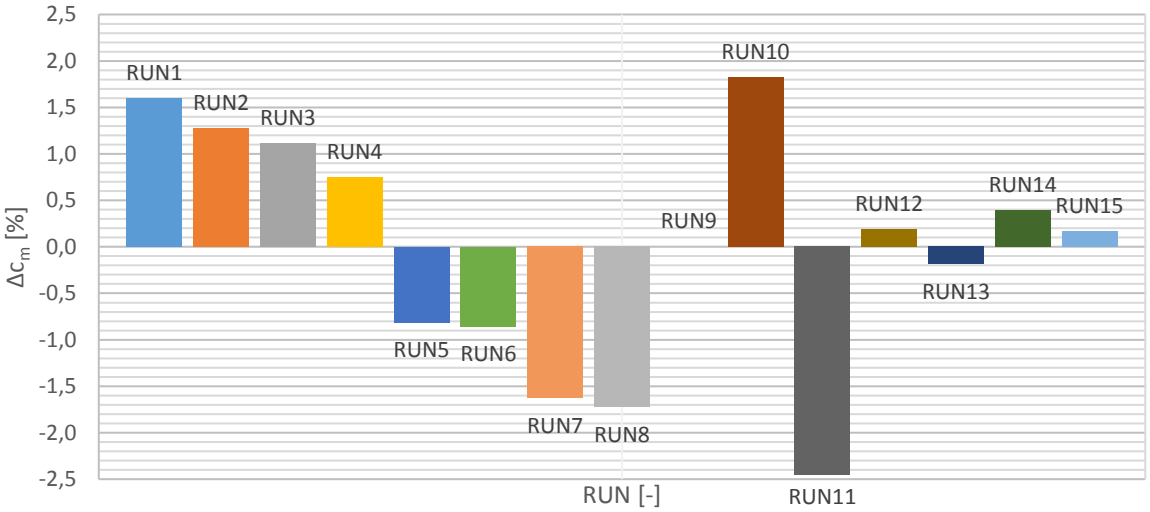

Fig. 10.2 Comparison of moment coefficient of individual cases to reference case (+2)

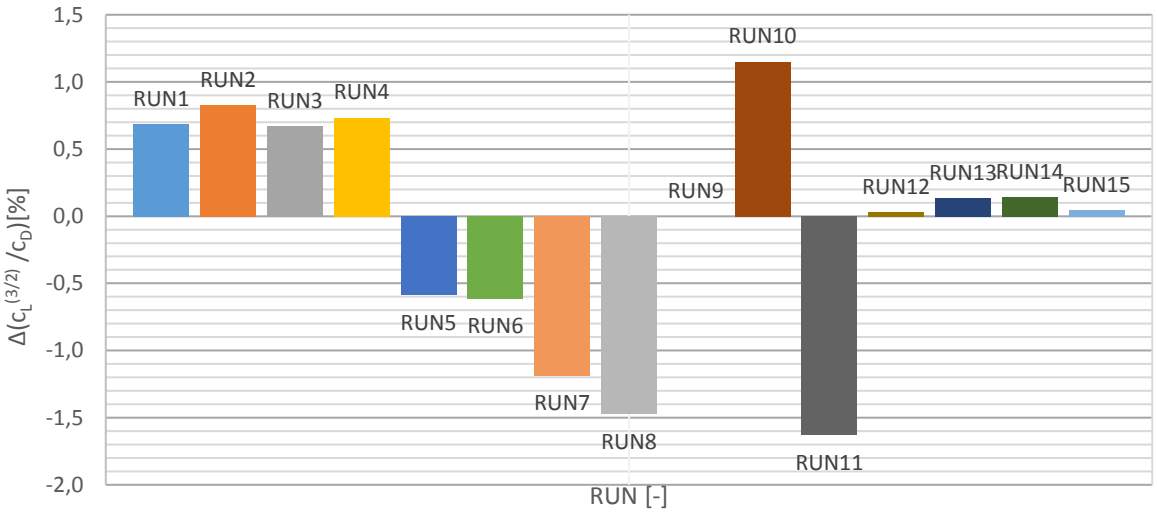

Fig. 10.3 Comparison of $c_L^{(3/2)}/c_D$ of individual cases to reference case (+2)

From above mentioned figures, it is obvious, that cases with higher cant angles (run 1 to 4 and run 10) has significantly higher $c_L^{(3/2)}/c_D$ ratio, however also the moment coefficient of the wing is higher which is undesirable effect. In case of the low cant angle cases, moment coefficient is lower in comparison to reference case, however also the $c_L^{(3/2)}/c_D$ ratio is significantly lower. When cant angle is not changed and only the toe-in and tip-in angles are changed, gain on the side of $c_L^{(3/2)}/c_D$ is not as high as in the cases with increased cant angle, but in one case, reduction of the moment coefficient is observed.

All results of simulations of the low speed flight regime were used during the particular parts of optimisation as will be described in the chapter 10.4.

After low speed case was evaluated, same process was used for the evaluation of the aerodynamic characteristics in the high speed flight with flap position -2. Tabular data of aerodynamic characteristics for high speed flight case are in the following table 10.5.

RUN / M	Aerodynamic characteristics of wing and winglet assembly – high speed case								
	c_D	c_L	$\frac{c_L}{c_D}$	c_m	$\frac{c_L^{3/2}}{c_D}$	c_{Dv}	c_{Dp}	c_{Dw}	D_w
	[-]	[-]	[-]	[-]	[-]	[-]	[-]	[-]	[N]
1	0,01418	0,25403	17,91739	-0,04772	9,03057	0,00844	0,00574	0,00032	3,22670
2	0,01410	0,25275	17,92740	-0,04732	9,01294	0,00844	0,00566	0,00024	2,43131
3	0,01403	0,24965	17,79830	-0,04642	8,89297	0,00843	0,00560	0,00017	1,67799
4	0,01402	0,24840	17,71333	-0,04595	8,82832	0,00842	0,00561	0,00016	1,61912
5	0,01420	0,25183	17,73082	-0,04649	8,89774	0,00844	0,00576	0,00030	2,98878
6	0,01421	0,25040	17,61913	-0,04640	8,81659	0,00840	0,00581	0,00023	2,27915
7	0,01404	0,24852	17,69943	-0,04577	8,82351	0,00842	0,00562	0,00014	1,45677
8	0,01403	0,24790	17,67331	-0,04558	8,79954	0,00841	0,00561	0,00015	1,50701
9	0,01403	0,25038	17,84844	-0,04647	8,93102	0,00843	0,00560	0,00017	1,72732
10	0,01402	0,25174	17,95123	-0,04716	9,00675	0,00843	0,00560	0,00019	1,88828
11	0,01407	0,24925	17,71655	-0,04578	8,84496	0,00844	0,00563	0,00015	1,53461
12	0,01439	0,25544	17,74941	-0,04773	8,97071	0,00849	0,00590	0,00038	3,83387
13	0,01404	0,24719	17,60578	-0,04550	8,75329	0,00841	0,00563	0,00017	1,70471
14	0,01426	0,25304	17,74907	-0,04711	8,92840	0,00849	0,00577	0,00024	2,45001
15	0,01417	0,25114	17,72096	-0,04657	8,88073	0,00848	0,00570	0,00017	1,72261

Tab. 10.5 Aerodynamic characteristics for high speed cases (flap -2)

Comparison of the individual cases to the reference case are shown in the figure 10.4 through 10.6. Numerical values are mentioned in appendix 2, table A2.1.

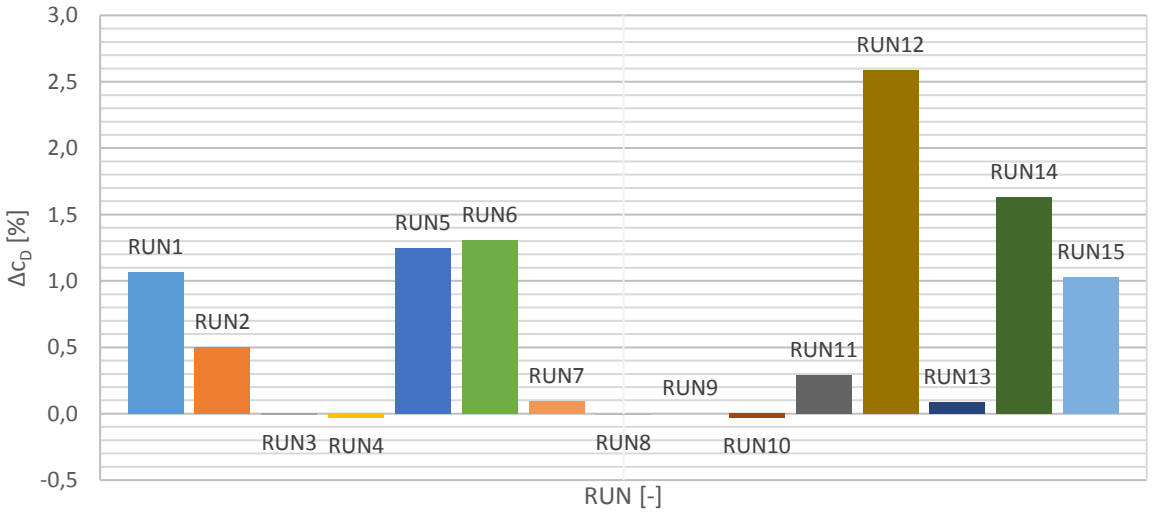

Fig. 10.4 Comparison of drag coefficient of individual cases to reference case (-2)

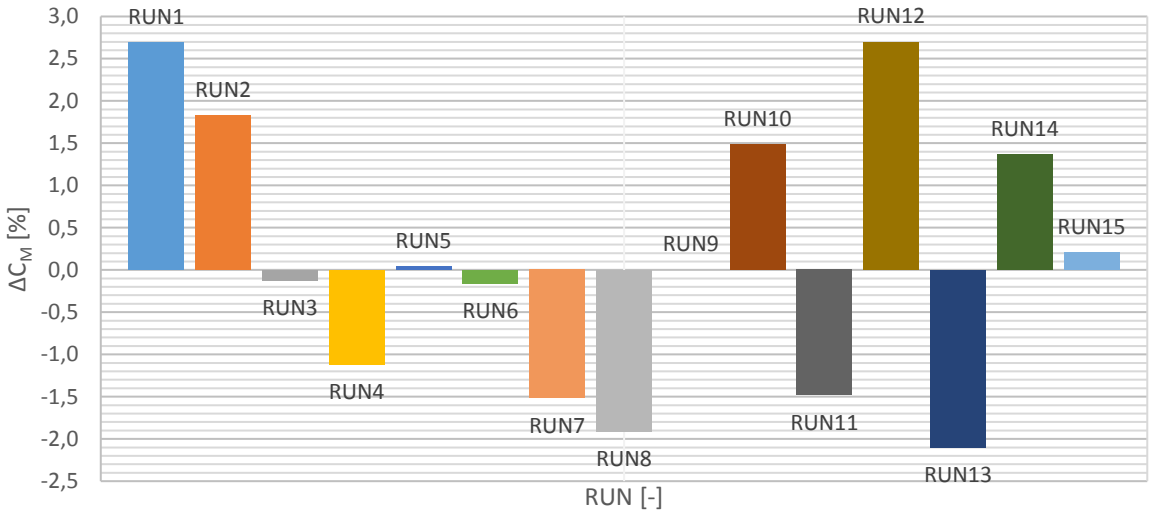

Fig. 10.5 Comparison of moment coefficient of individual cases to reference case (-2)

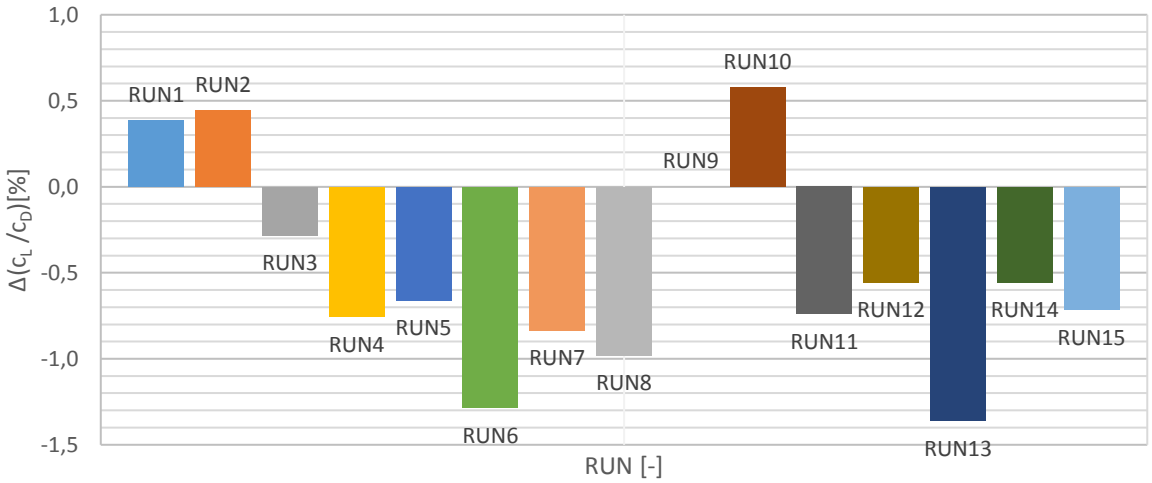

Fig. 10.6 Comparison of glide ratio of individual cases to reference case (-2)

Figures 10.5 and 10.6 shows, that there is only little space for the improvement of the lift to drag ratio and reduction of the moment coefficient of the wing. If the lift to drag ratio has to be improved, then cant angle must be increased significantly, which may unfortunately lead to the increased moment coefficient. From the table 10.5, it is obvious, that winglet is operating in the region beyond breaking point and in all of the cases the winglet causes additional drag. However, the optimisation process should lead to the improved variant, even when the space for improvement is little.

10.3 Cost function design

When all design variants based on the central composite design were evaluated, next step was to create functions, which will express the quality of each case from the aerodynamical point of view. Totally two cost functions were created. First for the low speed flight case and one for the high speed one. Two cost functions are necessary, as the target criteria for the low speed case optimisation are not the same as that of the high speed case.

Criteria, chosen for the low speed flight case are:

1) Maximizing value of $\frac{c_L^{3/2}}{c_D}$ ratio
2) Minimizing value of c_m

Criteria, chosen for the low speed flight case are:

1) Maximizing value of $\frac{c_L}{c_D}$ ratio
2) Minimizing value of c_m

Reasons for the above mentioned criteria choice are following. Maximizing of the $\frac{c_L^{3/2}}{c_D}$ ratio is based on the effort to achieve maximum possible performance when sailplane is gaining height in the thermals. Maximum climb speed is achieved, when $\frac{c_L^{3/2}}{c_D}$ ratio is maximized. This is documented by equation 10.2.

$$w_{min} = -\left(\frac{c_D}{c_L^{3/2}}\right)_{min} \cdot \sqrt{\frac{2}{\rho} \cdot \left(\frac{G}{S}\right)} \qquad [1] (10.2)$$

Where w_{min} stands for minimum speed of descent.

Minimization of the moment coefficient value c_m is desirable from the aspect of additional drag caused by the need of the aircraft trimming. When the moment coefficient of the wing is high, high downforce has to be generated at the horizontal tail, which increases the total drag of sailplane. Minimising of the moment coefficient is beneficious also from the structural point of view. High values of the moment coefficient of the high aspect ratio wing lead to the need of the increase of the wing stiffness, which could be projected to the higher wing mass and thus for example to the possibility of reduction of the water ballast carrying capability.

Finally, maximizing of the $\frac{c_L}{c_D}$ ratio was chosen for the reason of the maximal effort of increasing glide ratio of the sailplane during interthermal phase of flight. Increasing of the glide ratio at the high speed leads to the increase of the distance flown per unit of altitude lost. Increasing of the $\frac{c_L}{c_D}$ at high speeds could be virtually understood as moving the speed polar points toward the higher speeds. Maximizing of the glide ratio leads to the minimizing of the glide slope value which is documented by following equation.

$$\bar{\gamma}_{min} = \text{arctg}\left(\frac{c_D}{c_L}\right)_{min} \qquad [1] (10.3)$$

General form of cost functions is based on the following equation.

$$F = \sum w_i \cdot f_i \qquad [7] (10.4)$$

Where w_i is weight of the parameter f_i. Value of parameter weight is defined by the following equation.

$$w_i = \frac{z_i}{\sum z_i} \qquad [7] (10.5)$$

Where z_i is the percental importance of the parameter *i* and $\sum z_i$ is 100%.

Optimisation parameters are not used directly in the cost function. Instead of that, substitution parameter f_i is used. Parameter f_i is calculated using following equations.

$$f_i = \frac{f_N}{f_{REF}} \qquad \text{[7] (10.6)}$$

Where f_N is the value of parameter *N* and f_{REF} is the value of parameter in the reference case. Equation 10.6 is used in case, that parameter *N* value should be maximized. Higher the value of parameter N is, higher is the value of substitution parameter f_i. In case the parameter *N* value should be minimized, than equation 10.7 must be used.

$$f_i = \frac{f_{REF}}{f_N} \qquad \text{[7] (10.7)}$$

From the above mentioned, it is obvious, that cost function value in reference case is 1. During optimisation process described below, cost function value should be maximized and thus values of cost function above 1 designates solutions with higher performance than reference case.

Percental importance of parameters for low speed and high speed case is defined in the table 10.6.

Low speed		High speed	
Parameter 1	$\frac{c_L^{3/2}}{c_D}$	Parameter 3	$\frac{c_L}{c_D}$
Importance 1	$z_1 = 90\%$	Importance 3	$z_3 = 90\%$
Parameter 2	c_m	Parameter 4	c_m
Importance 2	$z_2 = 10\%$	Importance 4	$z_4 = 10\%$

Tab. 10.6 Parameters importance settings

Importance of individual parameters was set with high emphasis on the increasing of values which directly affects the performance of wing. Importance of the moment coefficient was set to 10% as it affects sailplane performance indirectly and influence of the trim drag on the overall drag of the sailplane is low. This should be seen on the example of ASW-27 sailplane speed polar subdivided to the individual parts contribution to the overall sink rate. However, further investigation of the moment coefficient influence on the sailplane performance would be beneficious and should be recommended at this place, if any further investigations will be done in the future.

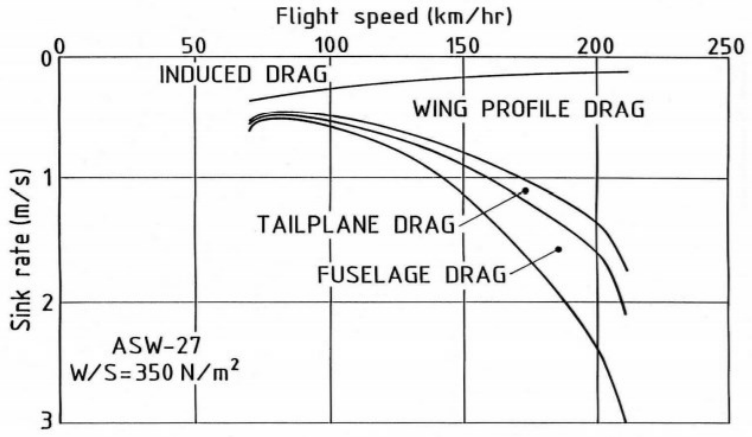

Fig. 10.7 Subdivided ASW-27 speed polar

When all above mentioned aspects are considered, final form of cost functions is following. For the low speed flight case, cost function is defined by equation 10.8.

$$F_{+2} = f_1 \cdot w_1 + f_2 \cdot w_2 \tag{10.8}$$

Where:

$$w_1 = 0{,}9 \tag{10.9}$$

And:

$$w_2 = 0{,}1 \tag{10.10}$$

For the high speed flight case, cost function is defined by equation 10.11.

$$F_{-2} = f_3 \cdot w_3 + f_4 \cdot w_4 \tag{10.11}$$

Where:

$$w_3 = 0{,}9 \tag{10.12}$$

And:

$$w_4 = 0{,}1 \tag{10.13}$$

10.4 Optimums search

For the optimal solution search in case of low speed and high speed flight regimes, firstly the cost function values must be determined for all runs defined in the chapter 10.1. All values of the f_N and f_{REF} are mentioned in the chapter 10.2, tables 10.4 and 10.5. In the following tables, values of cost function for all design cases are mentioned.

RUN	Low speed regime			High speed regime		
	f_1	f_2	F_{+2}	f_3	f_4	F_{-2}
	[-]	[-]	[-]	[-]	[-]	[-]
1	1,00687	0,98429	1,00461	1,00386	0,97375	1,00085
2	1,00826	0,98743	1,00617	1,00442	0,98200	1,00218
3	1,00671	0,98903	1,00494	0,99719	1,00123	0,99759
4	1,00734	0,99255	1,00586	0,99243	1,01127	0,99431
5	0,99415	1,00821	0,99556	0,99341	0,99958	0,99403
6	0,99387	1,00862	0,99535	0,98715	1,00158	0,98860
7	0,98815	1,01654	0,99099	0,99165	1,01537	0,99402
8	0,98529	1,01750	0,98851	0,99019	1,01950	0,99312
9	1,00000	1,00000	1,00000	1,00000	1,00000	1,00000
10	1,01149	0,98209	1,00855	1,00576	0,98533	1,00372
11	0,98373	1,02517	0,98787	0,99261	1,01502	0,99485
12	1,00031	0,99814	1,00009	0,99445	0,97371	0,99238
13	1,00135	1,00184	1,00140	0,98640	1,02143	0,98991
14	1,00143	0,99606	1,00090	0,99443	0,98655	0,99364
15	1,00045	0,99837	1,00025	0,99286	0,99794	0,99337

Tab. 10.6 Cost function values for low and high speed flight regime

When the cost function values were determined, appropriate regression model must be used to estimate the response surface shape. Linear regression model was chosen and process of its applying to the optimisation process will be described below.

Quadratic polynomial used for the response surface function is described by the equation 10.14.

$$y = \beta_0 + \sum_{j=1}^{k} \beta_j X_j + \sum_{j=1}^{k} \beta_{jj} {X_j}^2 + \sum_{i<j}^{k} \beta_{ij} X_i X_j \qquad [10]\ (10.14)$$

When substitution is done, equation 10.14 transforms to 10.15.

$$y = \beta_0 + \beta_1 X_1 + \beta_2 X_2 + \beta_3 X_3 + \beta_{11} X_1^2 + \beta_{22} X_1^2 + \beta_{33} X_3^2 + \\ + \beta_{12} X_1 X_2 + \beta_{13} X_1 X_3 + \beta_{23} X_2 X_3 \qquad [10]\ (10.15)$$

Second degree terms were replaced with single variables. [10]

$$\begin{aligned} X_1^2 &= X_7 \\ X_2^2 &= X_8 \\ X_3^2 &= X_9 \\ X_1 X_2 &= X_4 \\ X_1 X_3 &= X_5 \\ X_2 X_3 &= X_6 \end{aligned} \qquad [10]\ (10.16)$$

By this linearization of the equation 10.15, linear regression model could be applied. Regression model is defined by following equation.

$$y = X\beta + \varepsilon \qquad \text{[10] (10.17)}$$

$$y = \begin{Bmatrix} y_1 \\ y_2 \\ y_3 \\ \vdots \\ y_n \end{Bmatrix} \quad X = \begin{Bmatrix} 1\ X_{11}\ X_{12}\ \ldots X_{1k} \\ 1\ X_{11}\ X_{12}\ \ldots X_{1k} \\ \vdots\ \vdots\ \vdots\ \ddots\ \vdots \\ 1\ X_{n1}\ X_{n2}\ \ldots X_{nk} \end{Bmatrix} \quad \beta = \begin{Bmatrix} \beta_1 \\ \beta_2 \\ \vdots \\ \beta_n \end{Bmatrix} \quad \varepsilon = \begin{Bmatrix} \varepsilon_1 \\ \varepsilon_2 \\ \vdots \\ \varepsilon_n \end{Bmatrix}$$

Where k stands for number of coded variables and n for the number of cases evaluated.

When method of sum of least squares is used, unbiased estimator b of the coefficient β could be determined by equation 10.18. [10]

$$b = (X^T X)^{-1} X^T y \qquad \text{[10] (10.18)}$$

When regression model is fitted to the database of the design points defined by full factorial central composite design, some measurement of the fit quality should be made. For the basic evaluation of the quality of regression model, the coefficient of determination R^2 is used. R^2 value of 1 means exact match of design points. When residuals values increasing, R^2 value decreasing. R^2 value is in the range from 0 to 1. When number of observations is increased, residuals value decreases and R^2 value increases. Because of this, for more precision inspection of the regression model, or response surface approximation, the coefficient of determination adjusted R^2_{adj} for the degrees of freedom should be used. R^2_{adj} gives the percentage of variation explained by those independent variables, that actually affects the dependent variable. [10]

Totally four optimal cases should be found. Even when the flight regimes are two, it was decided to find four optimal values. Two for the sailplane of FAI 15m class, so the wingspan of 15m mustn´t be exceeded and two optimal variants should be found without span restrictions to investigate maximum possible gain from the geometry change in the design space defined by design of experiments.

For optimisation with restriction of wingspan, only cases with no cant angle change were used. Namely, the runs 9 and 12 through 15. However, the multicollinearity problem occurs when regression was done. This problem may be solved by addition of four more data points which will have coded variables values mentioned in table 10.6. This step wasn't made, as the time requirements for computations of another four simulations in the +2 case and four in -2 case should not be met, as 39 simulations had to be done during complete process of optimisation.

Additional point. no.	X1	X2	X3
1	1	1	0
2	1	-1	0
3	-1	1	0
4	-1	-1	0

Tab. 10.7 Additional data points for solving multicollinearity problem

However, despite the fact of multicollinearity, effort was made to evaluate the cases for low speed 15m case and high speed 15m case. Simulations may provide better solutions than the reference case is, as the regression model fits the data points, which are in literally one plane in DOE and dependency may be well predicted.

For optimisation without span restriction all cases were used. Table with unbiased estimators b and coefficients of determination R^2 and R^2_{adj} are mentioned in the following table.

Coefficient	Low speed, 15m	High speed, 15m	Low speed	High speed
b_0	1,00000E+00	1,00000E+00	1,00000E+00	1,00000E+00
b_1	0,00000E+00	0,00000E+00	6,21411E-03	2,89521E-03
b_2	-3,77640E-04	7,13106E-04	6,51606E-04	7,77380E-04
b_3	1,87406E-04	8,05013E-05	9,46957E-05	6,26418E-04
b_{12}	0,00000E+00	0,00000E+00	-1,42845E-03	1,95548E-03
b_{13}	0,00000E+00	0,00000E+00	-6,47832E-04	-5,48145E-04
b_{23}	0,00000E+00	0,00000E+00	-3,64290E-04	-1,02279E-05
b_{11}	0,00000E+00	0,00000E+00	-7,56370E-04	-5,88534E-05
b_{22}	2,48658E-04	-2,95252E-03	8,78111E-05	-2,77258E-03
b_{33}	1,90408E-04	-2,16496E-03	2,95611E-05	-1,98503E-03
R^2	1	1	0,97524	0,93483
R^2_{adj}	1	1	0,93068	0,81753

Tab. 10.8 Coefficients values used for optimum search

When coefficients of fitted response function is determined, optimal setting of parameters could be found. For the optimum setting of parameters search, the MATLAB software was used. Principle of optimum searching will be described now.

Design space discretization were done, by dividing the coded variables range to finite number of subranges. This is described by following equations.

$$X_{ji} = X_{j,min} + (i-1)\frac{X_{j,max} - X_{j,min}}{n-1} \quad j = \{1,2 \dots k\} \tag{10.19}$$

Where n is target count of discretized coded variables. In this case n is set to value:

$$n = 250 \tag{10.20}$$

Where i is target index of discretized coded variable.

$$i = \{1,2 \dots n\} \tag{10.21}$$

After discretization of the design space, values of cost function at all points defined by variations of the coded variables must be determined. Variations were determined using MATLAB software and matrix of all variations is be described by equation 10.22.

$$\boldsymbol{V} = \begin{Bmatrix} 1 & \cdots & n & n+1 & \cdots & 2n & \cdots & \cdots & \cdots & \cdots & v \\ X_{11} & \cdots & X_{1n} & X_{11} & \cdots & X_{1n} & \cdots & X_{11} & \cdots & X_{1n} & \cdots & X_{1n} \\ X_{21} & \cdots & X_{21} & X_{22} & \cdots & X_{22} & \cdots & X_{21} & \cdots & X_{2n} & \cdots & X_{2n} \\ X_{31} & \cdots & X_{31} & X_{31} & \cdots & X_{31} & \cdots & X_{32} & \cdots & X_{3n} & \cdots & X_{3n} \end{Bmatrix} \tag{10.22}$$

Where v is number of variations given by.

$$v = V'(n,k) = n^k \tag{10.23}$$

After computation:

$$v = 15\,625\,000 \tag{10.24}$$

Values of response function was determined in all 15 625 000 points of design space. Values determined using coefficients b determined by method of least squares are designated B.

$$B = \mathrm{b}_0 + \mathrm{b}_1\mathrm{X}_1 + \mathrm{b}_2\mathrm{X}_2 + \mathrm{b}_3\mathrm{X}_3 + \mathrm{b}_{11}X_1^2 + \mathrm{b}_{22}X_1^2 + \mathrm{b}_{33}X_3^2 + \\ +\mathrm{b}_{12}X_1X_2 + \mathrm{b}_{13}X_1X_3 + \mathrm{b}_{23}X_2X_3 \tag{10.25}$$

After all variations were determined and values of function B was determined in all discretized design space points, maximum value was found using MATLAB and combination of X_1 through X_3 which is relevant to the maximum value was determined. Coded variables determined by above mentioned process was decoded and appropriate CAD model was created, pre-processed within ICEM CFD, simulation was done within ANSYS Fluent solver and results were evaluated. Values of the coded and natural variables of the optimum cases is mentioned in the table 10.9.

Case	$\mathrm{X}_{1\mathrm{opt}}$ [−]	$\mathrm{X}_{2\mathrm{opt}}$ [−]	$\mathrm{X}_{3\mathrm{opt}}$ [−]	$\xi_{1\mathrm{opt}}$ [°]	$\xi_{2\mathrm{opt}}$ [°]	$\xi_{3\mathrm{opt}}$ [°]	$\mathrm{B}_{\mathrm{opt}}$ [−]
LS, 15m	0,00000	-1,73205	1,73205	0,00000	-8,19615	4,19615	1,00230
HS, 15m	0,00000	0,11825	0,02087	0,00000	-2,64524	-0,93740	1,00004
LS	1,73205	-1,73205	-1,73205	17,32051	-8,19615	-6,19615	1,01269
HS	1,73205	0,74429	-0,07652	17,32051	-0,76712	-1,22955	1,00642

Tab. 10.9 Optimal values of coded and natural variables

To maximize the effect of winglets at the 15m wingspan restricted configurations designated LS, 15m and HS, 15m in the table 10.8, the values of $\mathrm{X}_{1\mathrm{opt}}$ and $\xi_{1\mathrm{opt}}$ respectively, was adjusted to obtain exactly 15m wingspan. This means, that optimal parameters of these two cases has finally, after adjustment of cant angle within CATIA CAD system, following values.

Case	$\mathrm{X}_{1\mathrm{opt,15m}}$ [°]	$\mathrm{X}_{2\mathrm{opt,15m}}$ [°]	$\mathrm{X}_{3\mathrm{opt,15m}}$ [°]	$\xi_{1\mathrm{opt,15m}}$ [°]	$\xi_{2\mathrm{opt,15m}}$ [°]	$\xi_{3\mathrm{opt,15m}}$ [°]
LS, 15m	-0,04250	-1,73205	1,73205	-0,42500	-8,19615	4,19615
HS, 15m	0,02030	0,11825	0,02087	0,20300	-2,64524	-0,93740

Tab. 10.10 Optimal values of coded and natural variables for 15m class

Evaluation of four optimal geometries descripted above is described in the chapter 11.

11 OPTIMAL WINGLET SHAPES EVALUATION

Winglets with design parameters which were determined in the chapter 10 were subjected to the CFD simulations within ANSYS Fluent. Results will be evaluated within this chapter with description of each case individually.

11.1 Restricted wingspan low speed optimum

As was mentioned above, winglet optimised with wingspan restricted to 15m was subjected to analysis and evaluated during postprocessing in the Fluent software. Geometrical configuration of winglet evaluated in this case are mentioned in the following table.

Parameter	Cant angle	Toe-in angle	Tip-in angle
Designation	ϕ	γ_{wr}	γ_{wt}
Value	8,18104	-8,19615	4,19615
Unit	°	°	°

Tab. 11.1 Low speed 15m case winglet settings

Values subjected to investigation were same as in the reference cases. Table with individual aerodynamic parameters values follows.

Wing and winglet			
Lift coefficient	c_L	1,52134	-
Drag coefficient	c_D	0,06299	-
Moment coefficient	c_m	-0,16477	-
Pressure drag coefficient	c_{Dp}	0,05384	-
Viscous drag coefficient	c_{Dv}	0,00914	-
Lift to Drag ratio	c_L / c_D	24,15323	-
Third power of lift coefficient squared to drag coefficient ratio	$c_L^{3/2} / c_D$	29,79117	
Ratio of pressure drag to total drag	$(c_{Dp} / c_D) \cdot 100$	85,48508	%
Ratio of viscous drag to total drag	$(c_{Dv} / c_D) \cdot 100$	14,51492	%
Winglet			
Lift coefficient	c_{Lw}	0,00621	-
Drag coefficient	c_{Dw}	-0,00103	-
Drag	D_w	-1,69701	N

Tab. 11.2 Low speed 15m case aerodynamic parameters evaluation

For comparison of the optimized case to the reference one, key values differences were estimated in the relative form. Table 11.3 gives good overview of the changes in the performance.

Parameter	Designation	Value	Unit
Drag coefficient change	Δc_D	-0,19690	%
Lift coefficient change	Δc_L	0,10921	%
Moment coefficient change	Δc_m	-0,14027	%
Glide ratio change	$\Delta c_L/c_D$	0,30671	%
Third power of lift coefficient squared to drag coefficient ratio change	$\Delta c_L^{3/2}/c_D$	0,36147	%

Tab. 11.3 Low speed 15m case and low speed reference case comparison

Graphical form of the selected parameters results mentioned in the table 11.3 are in the appendix 3, figure A3.1.

However, above mentioned data are not sufficient for decision if the case is optimal, or not. For this decision, the evaluation of cost function must be done. Values for individual parameters f_1, which belongs to the third power of lift coefficient squared to drag coefficient ratio and f_2 which belongs to the moment coefficient are mentioned in the table 10.4 together with the reference case cost function value, highest value of cost function within runs 9, 12, 13, 14, 15, which belongs to the low speed flight investigation and finally with the value of 15m restricted wingspan low speed case cost function value.

Parameter	Designation	Value
Parameter 1	f_1	1,003615
Parameter 2	f_2	1,001405
Reference run cost function value	$F_{reference}$	1,000000
Highest value of cost function in database	$F_{max,(9,12,13,14,15)}$	1,001400
Value of cost function (LS, 15m)	$F_{LS,15m}$	1,003394

Tab. 11.4 Low speed 15m case cost function evaluation

From values in the table 11.4, it is obvious, that value of cost function is highest of all cases with no cant angle change and can be considered as optimum.

Significant feature of this case is achievement of higher lift to drag ratio and third power of lift coefficient squared to drag coefficient ratio and at the same time achievement of significant reduction of the moment coefficient. What should be noted further is, that winglet shape is unusual with high negative toe-in angle and high positive tip-in angle. It shall be considered, that position of thrust force resultant of winglet lays in the lower position relative to the wing than in the reference case. Winglet rear view and front view are shown in the figure 11.1.

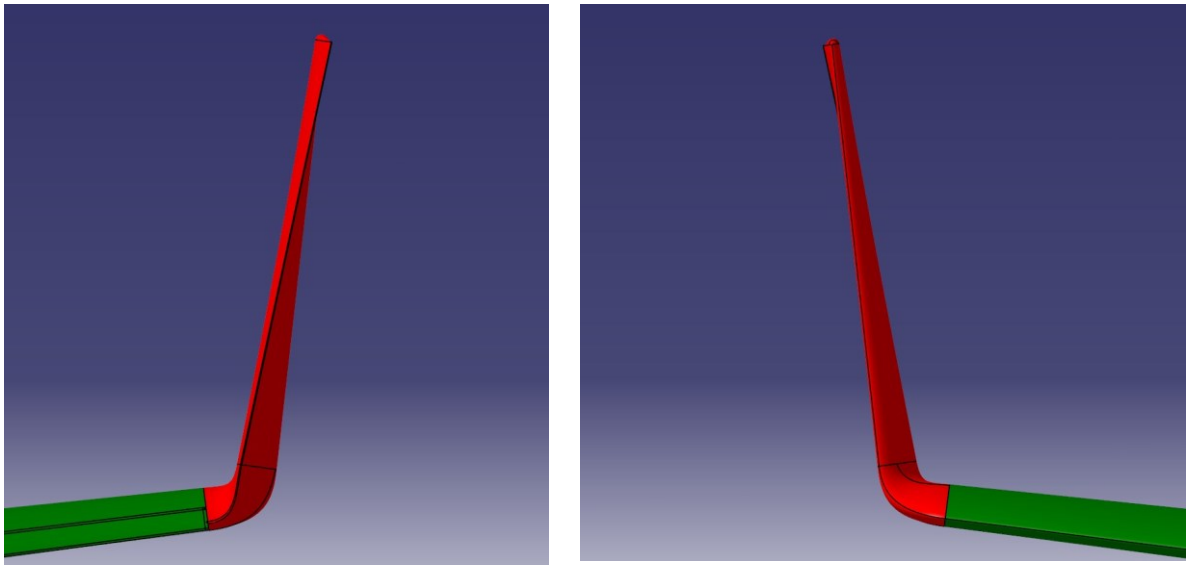

Fig. 11.1 Rear (left) and front (right) views on the winglet geometry

Significant reduction on the side of drag coefficient was achieved by elimination of the turbulent flow near the trailing edge of the winglet to wing junction upper side, which could be seen in the figure 11.2. For comparison, it is recommended to view the figure 9.19.

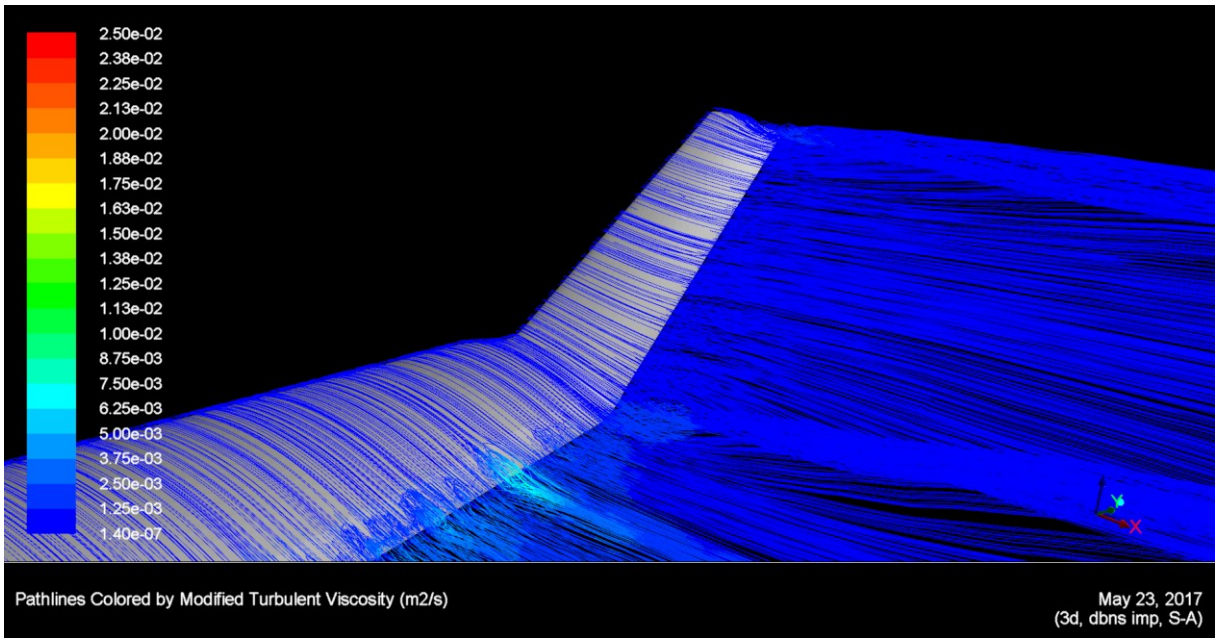

Fig. 11.2 Flow visualisation of wing to winglet junction region of LS 15m optimized case

It should be mentioned at this place, that methodology of evaluation of other optimized cases will be equal to the evaluation in this chapter.

11.2 Unrestricted wingspan low speed optimum

Winglet geometry which was defined by the optimisation process has following parameters.

Parameter	Cant angle	Toe-in angle	Tip-in angle
Designation	ϕ	γ_{wr}	γ_{wt}
Value	25,54404	-8,19615	-6,19615
Unit	°	°	°

Tab. 11.5 Low speed no wingspan restricted case winglet settings

Values subjected to investigation were same as in the reference cases. Table with individual aerodynamic parameters values follows.

Wing and winglet			
Lift coefficient	c_L	1,52338	-
Drag coefficient	c_D	0,06303	-
Moment coefficient	c_m	-0,16664	-
Pressure drag coefficient	c_{Dp}	0,05389	-
Viscous drag coefficient	c_{Dv}	0,00914	-
Lift to Drag ratio	c_L / c_D	24,16946	-
Third power of lift coefficient squared to drag coefficient ratio	$c_L^{3/2} / c_D$	29,83121	
Ratio of pressure drag to total drag	$(c_{Dp} / c_D) \cdot 100$	85,49978	%
Ratio of viscous drag to total drag	$(c_{Dv} / c_D) \cdot 100$	14,50022	%
Winglet			
Lift coefficient	c_{Lw}	0,00919	-
Drag coefficient	c_{Dw}	-0,00099	-
Drag	D_w	-1,62735	N

Tab. 11.6 Low speed no wingspan restricted case aerodynamic parameters evaluation

For comparison of the optimized case to the reference one follows in the table 11.7.

Parameter	Designation	Value	Unit
Drag coefficient change	Δc_D	-0,13000	%
Lift coefficient change	Δc_L	0,24366	%
Moment coefficient change	Δc_m	0,99661	%
Glide ratio change	$\Delta c_L/c_D$	0,37414	%
Third power of lift coefficient squared to drag coefficient ratio change	$\Delta {c_L}^{3/2}/c_D$	0,49635	%

Tab. 11.7 Low speed no wingspan restricted case and low speed reference case comparison

Graphical form of the selected parameters results mentioned in the table 11.7 are in the appendix 3, figure A3.2.

Evaluation of above mentioned data from the cost function values point of view follows. This time, for the highest value of cost function in database, all database points for low speed case were taken.

Parameter	Designation	Value
Parameter 1	f_1	1,004964
Parameter 2	f_2	0,990132
Reference run cost function value	$F_{reference}$	1,000000
Highest value of cost function in database	F_{max}	1,008554
Value of cost function (LS)	F_{LS}	1,003480

Tab. 11.8 Low speed no wingspan restricted case cost function evaluation

From values in the table 11.4, it is obvious, that value of cost function in the defined optimal geometry case is lower than the highest value of cost function in the database. This means, that optimisation in this case failed. It is absolutely necessary to clarify reasons of optimisation failure. The cause of the low performance in this case could be assumed to the strong underprediction of the negative values of the toe-in and tip-in angle in the case of winglet cant angle increase. Geometry of the winglet, when "twisted" to negative values, acts in the similar manner as when wing twist is applied. In this case, the negative values of toe-in and tip-in angle are clearly overpredicted. From the optimisation RSM model point of view, failure could be assumed to low number of the database elements. It is of the interest to increase number of observations for the low speed case, as the prediction based on the linear regression is obviously not well fitted to the real response surface shape. The multiple linear regression problem could be documented by comparison of values of cost functions determined directly from aerodynamic parameters obtained after evaluation of CFD results and values of cost function determined by regression model. Values of cost function are designated F_i and values of regression model are designated by B_i.

RUN	CFD cost function value	Regression model cost function value
1	1,004608	1,0038808
2	1,006175	1,0057157
3	1,004939	1,0061631
4	1,005863	1,0065408
5	0,995559	0,9956052
6	0,995349	0,9948487
7	0,990991	0,9921737
8	0,988509	0,9899600
9	1,000000	1,0000000
10	1,008554	1,0084940
11	0,987873	0,9869677
12	1,000092	1,0013920
13	1,001400	0,9991348
14	1,000896	1,0002527
15	1,000247	0,9999247

Tab. 11.9 Cost function F_i and B_i values comparison

From the table 11.9 is obvious, that values differences are not negligible and that order of the values of cost function determined directly from CFD evaluation and determined by regression model, when ordered by magnitude, is not the same.

Decision was taken at this place to evaluate low speed case RUN 10 instead of the above mentioned no wingspan restricted optimum. This decision is based on the values of cost function achieved during postprocessing of CFD results. RUN 10 has obviously the highest cost function value of all cases in the database. This decision is based also on the consideration of the time, which would be needed to enlarge the database. Time of each CFD simulation run was 13 hours in average, when only the time when simulation iterations were running is considered. Increasing of the database design cases number would take hundreds of hours of CFD pre-processing, simulations and postprocessing, which could not be done within the time frame of this thesis. However, increasing of the design cases database should be recommended as the countermeasures of problem which was faced during work on this thesis.

Further description in this sub-chapter belongs to the RUN 10 design case of the winglet, which was evaluated as the variant with highest cost function value.

Winglet geometry is defined by following geometrical parameters.

Parameter	Cant angle	Toe-in angle	Tip-in angle
Designation	ϕ	γ_{wr}	γ_{wt}
Value	25,54404	-3	-1
Unit	°	°	°

Tab. 11.10 Low speed RUN 10 case winglet settings

Aerodynamic parameters values of RUN 10 is mentioned in table 11.11 on the next page. Values doesn´t belong to the optimum winglet configuration. It is probable that higher performance could be obtained, if regression function is improved by adding more design points to design database.

Wing and winglet			
Lift coefficient	c_L	1,52647	-
Drag coefficient	c_D	0,06281	-
Moment coefficient	c_m	-0,16801	-
Pressure drag coefficient	c_{Dp}	0,05371	-
Viscous drag coefficient	c_{Dv}	0,00911	-
Lift to Drag ratio	c_L / c_D	24,30187	-
Third power of lift coefficient squared to drag coefficient ratio	$c_L^{3/2} / c_D$	30,02506	
Ratio of pressure drag to total drag	$(c_{Dp} / c_D) \cdot 100$	85,50025	%
Ratio of viscous drag to total drag	$(c_{Dv} / c_D) \cdot 100$	14,49975	%
Winglet			
Lift coefficient	c_{Lw}	0,01162	-
Drag coefficient	c_{Dw}	-0,00079	-
Drag	D_w	-1,30756	N

Tab. 11.12 Low speed RUN 10 case aerodynamic parameters evaluation

Comparison of the RUN 10 to the reference case is described in the table 11.13. From the comparison of RUN 10 versus reference case the conclusion follows, that the increase of the third power of lift coefficient squared to drag coefficient ratio is approximately 2,3 times higher than in case of span restricted optimal variant. However, the increment of moment coefficient is considerably high.

Parameter	Designation	Value	Unit
Drag coefficient change	Δc_D	-0,47247	%
Lift coefficient change	Δc_L	0,44716	%
Moment coefficient change	Δc_m	1,82354	%
Glide ratio change	$\Delta c_L / c_D$	0,92400	%
Third power of lift coefficient squared to drag coefficient ratio change	$\Delta c_L^{3/2} / c_D$	1,14939	%

Tab. 11.13 Low speed RUN 10 case and low speed reference case comparison

As the RUN 10 case is the case, with highest cost function value, comparison of this case to the reference case will not be mentioned. Graphical form of the selected parameters results mentioned in the table 11.13 are in the appendix 3, figure A3.3.

Comparison of winglet geometry determined as optimal in the beginning of this subchapter and geometry of RUN 10 is shown in the figure 11.3.

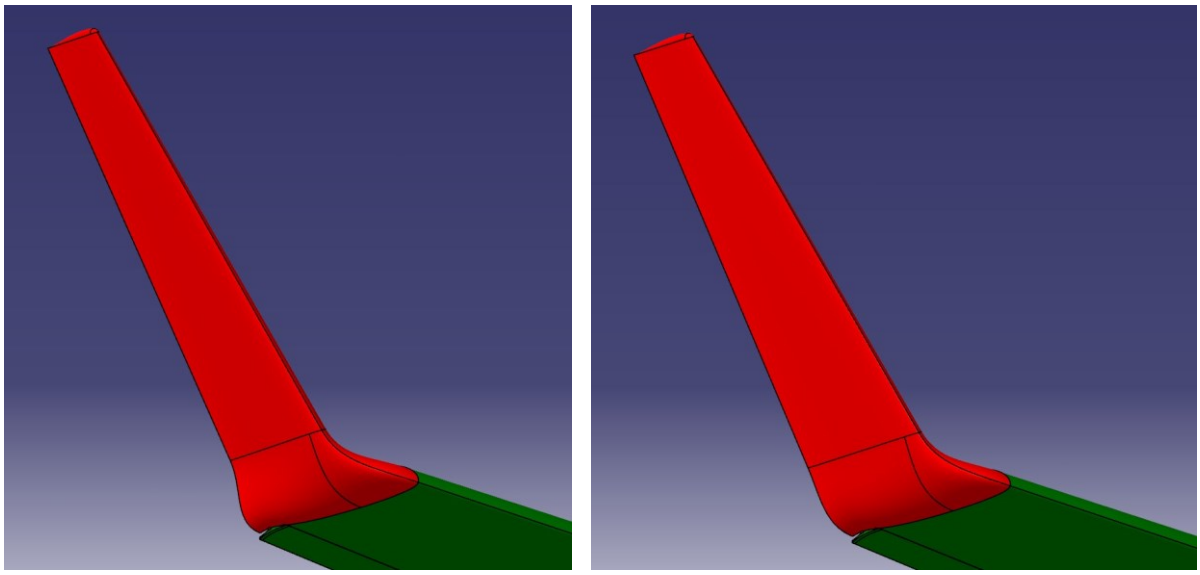

Fig. 11.3 Geometry determined as optimal (left) and geometry of RUN 10 design case

Form the values of cost functions of both above mentioned winglet geometries is obvious, that regression model overestimates the values of toe-in and tip-in angles. Flow visualisation in the problematic region on the upper side of the wing to winglet junction trailing edge is shown in the figure 11.4.

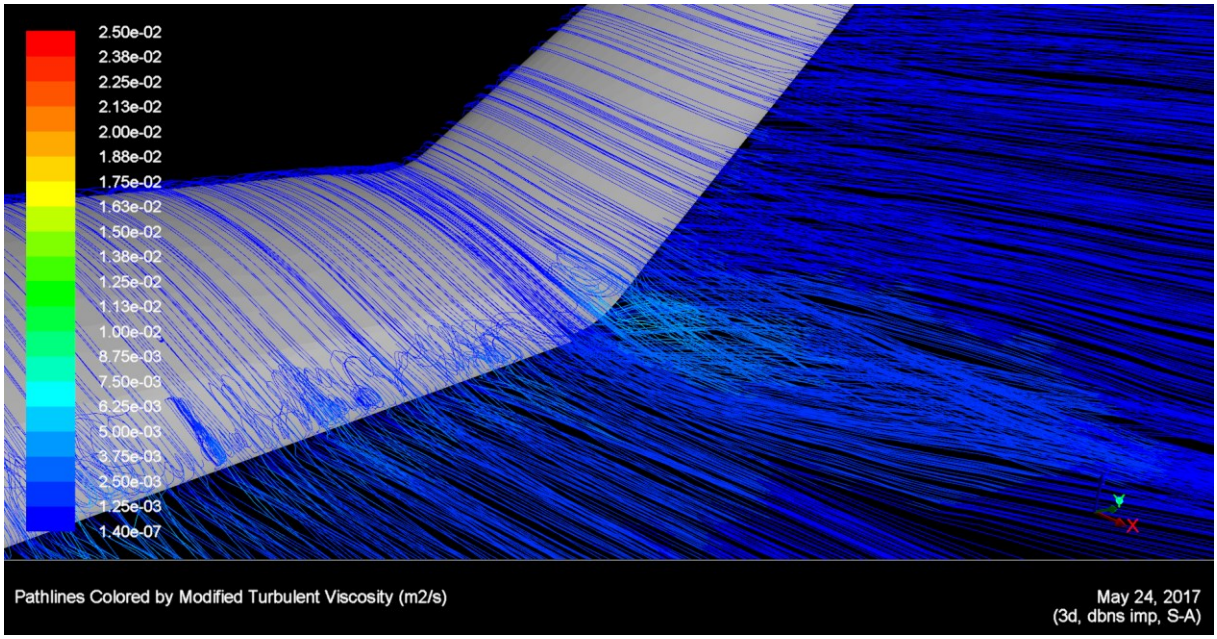

Fig. 11.4 Flow visualisation in the region of wing to winglet junction for RUN 10 case

There is apparent region if increased turbulence near the trailing edge. Lowering of the toe-in angle may lead to the elimination of the problem. Problem with this region is apparent also on the velocity magnitude contour map. Contour map describes velocity magnitude at isosurface 5 mm above wing and winglet surface.

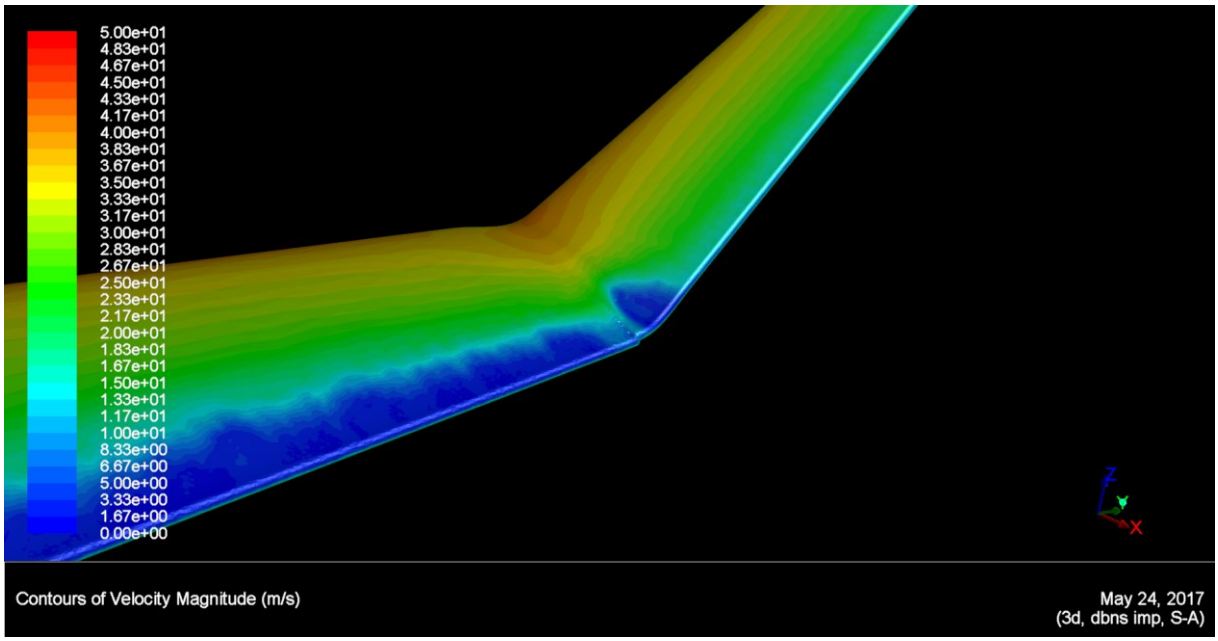

Fig. 11.5 Velocity magnitude in the region of wing to winglet junction for RUN 10 case

11.3 Restricted wingspan high speed optimum

Restricted wingspan variant for high speed case was evaluated in the same manner as the low speed one. Geometry parameters of the winglet is described in the table 11.14.

Parameter	Cant angle	Toe-in angle	Tip-in angle
Designation	ϕ	γ_{wr}	γ_{wt}
Value	8,42654	-2,64524	-0,93740
Unit	°	°	°

Tab. 11.14 High speed 15m case winglet settings

After evaluation of the CFD simulations performed, aerodynamic coefficients and values dependent on them were determined. Values are mentioned in the following table 11.15.

Wing and winglet			
Lift coefficient	c_L	0,25079	-
Drag coefficient	c_D	0,01404	-
Moment coefficient	c_m	-0,04656	-
Pressure drag coefficient	c_{Dp}	0,00561	-
Viscous drag coefficient	c_{Dv}	0,00825	-
Lift to Drag ratio	c_L / c_D	17,86469	-
Third power of lift coefficient squared to drag coefficient ratio	$c_L^{3/2} / c_D$	8,94646	
Ratio of pressure drag to total drag	$(c_{Dp} / c_D) \cdot 100$	39,94179	%
Ratio of viscous drag to total drag	$(c_{Dv} / c_D) \cdot 100$	58,77415	%
Winglet			
Lift coefficient	c_{Lw}	0,00165	-
Drag coefficient	c_{Dw}	0,00018	-
Drag	D_w	1,81229	N

Tab. 11.15 High speed 15m case aerodynamic parameters evaluation

Comparison of the high speed 15m restricted wingspan case and reference case follows.

Parameter	Designation	Value	Unit
Drag coefficient change	Δc_D	0,07259	%
Lift coefficient change	Δc_L	0,16370	%
Moment coefficient change	Δc_m	0,18738	%
Glide ratio change	$\Delta c_L/c_D$	0,09104	%
Third power of lift coefficient squared to drag coefficient ratio change	$\Delta c_L{}^{3/2}/c_D$	0,17293	%

Tab. 11.16 Low speed 15m case and low speed reference case comparison

To decide whether or not, the case is the optimal one, cost functions evaluation has to be done as in the predeceasing cases. Evaluation of cost functions follows.

Parameter	Designation	Value
Parameter 1	f_1	1,000910
Parameter 2	f_2	0,99813
Reference run cost function value	$F_{reference}$	1,000000
Highest value of cost function in database	$F_{max,(9,12,13,14,15)}$	1,000000
Value of cost function (HS, 15m)	$F_{HS,15m}$	1,000632

Tab. 11.17 High speed 15m case cost function evaluation

Highest value of cost function in database $F_{max,(9,12,13,14,15)}$ is of course taken from the high speed database.

From the above table 11.17, the conclusion can be made, that reference case is the case with highest cost function value within the limited database and also, that multicollinearity doesn't make much problems in the optimum value searching as the tendency of winglet to achieve optimum shape is satisfied. Tendency to reducing toe-in and tip-in angles is apparent from the table 10.6, where cost function value F_{-2} of run 12 is higher than that of run 13, and cost function value of run 14 is higher, than that of run 15. Both, run 12 and run 14 has toe-in and tip-in angle respectively, set to the high values, which in fact is the positions with reduced negative twist of the winglet. This documenting the tendency of winglet to achieve shape with reduced toe-in and tip-in which is described in the table 11.14.

Shape of the winglet can be considered as the optimum one as the cost function value of this optimized shape has higher cost function value than other cases within the limited database.

As the differences between the reference case and optimised case are really small, consideration can be made, that original winglet geometry was set to the shape to create lower possible drag to the airplane at the high speeds, but the gains at the low speeds are lower than it is possible. However this is the limitation of fixed geometry winglets, which are designed to the multi-regime optimum.

An interesting, but predictable fact is the location of the maximum flow speed in the wing to winglet junction upper side, which is documented by the figure 11.6.

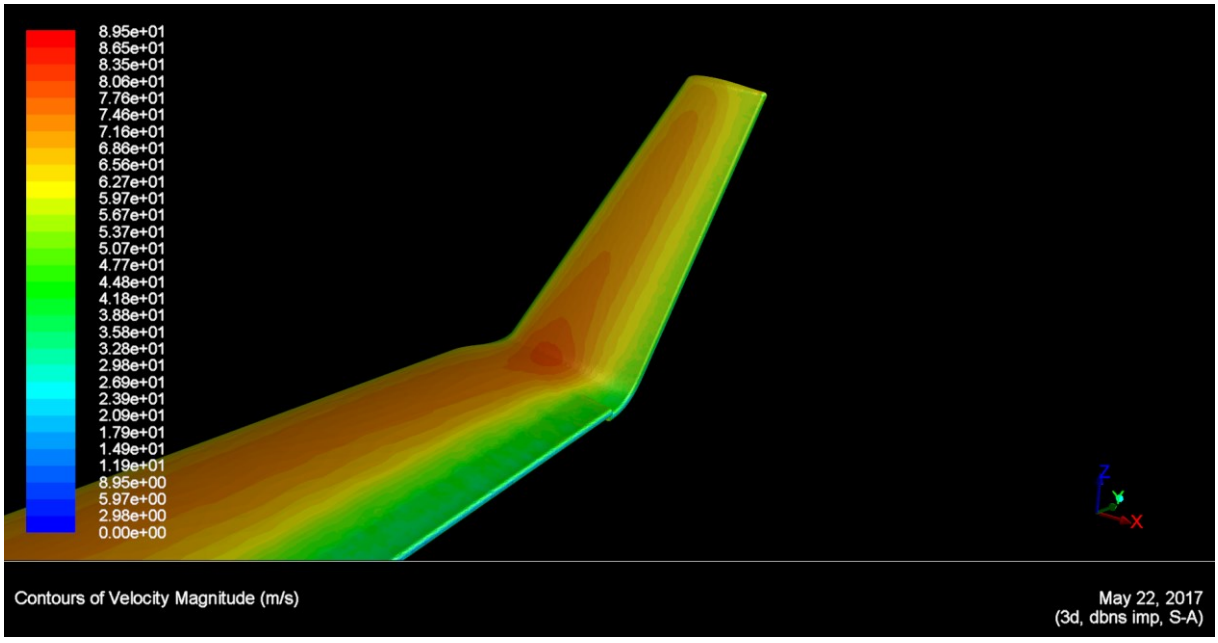

Fig. 11.6 Velocity magnitude in the region of wing to winglet junction for HS,15m case

Velocity magnitude 5mm above the wing surface is nearly 90 meters per second, which is approximately 1,5 times the free stream speed of the flow for the high speed case. And this high speed region exists despite the fact, that angle of attack is only 0,92 degrees. Speed gradually decreasing on the small length towards the trailing edge.

11.4 Unrestricted wingspan high speed optimum

High speed case without wingspan restriction optimum winglet shape were evaluated for the possibilities of the performance improvement. Geometry settings of the optimal winglet for this case are described in the table 11.18.

Parameter	Cant angle	Toe-in angle	Tip-in angle
Designation	ϕ	γ_{wr}	γ_{wt}
Value	25,54404	-0,76712	-1,22955
Unit	°	°	°

Tab. 11.18 High speed no wingspan restricted case winglet settings

Same aerodynamic parameters of the wing and winglet assembly were evaluated as in the sub chapters 11.1 to 11.3. Aerodynamic parameters evaluation table follows.

Wing and winglet			
Lift coefficient	c_L	0,25341	-
Drag coefficient	c_D	0,01408	-
Moment coefficient	c_m	-0,04769	-
Pressure drag coefficient	c_{Dp}	0,00565	-
Viscous drag coefficient	c_{Dv}	0,00844	-
Lift to Drag ratio	c_L / c_D	17,99570	-
Third power of lift coefficient squared to drag coefficient ratio	$c_L^{3/2} / c_D$	9,05901	
Ratio of pressure drag to total drag	$(c_{Dp} / c_D) \cdot 100$	40,09622	%
Ratio of viscous drag to total drag	$(c_{Dv} / c_D) \cdot 100$	59,90379	%
Winglet			
Lift coefficient	c_{Lw}	0,00353	-
Drag coefficient	c_{Dw}	0,00025	-
Drag	D_w	2,48415	N

Tab. 11.19 High speed no wingspan restricted case aerodynamic parameters evaluation

Comparison of the high speed no wingspan restricted case and reference case follows.

Parameter	Designation	Value	Unit
Drag coefficient change	Δc_D	0,38159	%
Lift coefficient change	Δc_L	1,20983	%
Moment coefficient change	Δc_m	2,61233	%
Glide ratio change	$\Delta c_L/c_D$	0,82509	%
Third power of lift coefficient squared to drag coefficient ratio change	$\Delta c_L^{3/2}/c_D$	1,43316	%

Tab. 11.20 Low speed no wingspan restricted case and low speed reference case comparison

As in the sub chapters before, the important step of the cost function value determination follows.

Parameter	Designation	Value
Parameter 1	f_1	1,008251
Parameter 2	f_2	0,974542
Reference run cost function value	$F_{reference}$	1,000000
Highest value of cost function in database	F_{max}	1,003716
Value of cost function (HS)	F_{HS}	1,004880

Tab. 11.21 High speed no wingspan restricted case cost function evaluation

Highest value of cost function F_{max} is determined from the full database of the high speed design cases. Cost function of the high speed omptimized case without span restriction is evidently higher than highest value of cost function in the full database of high speed design cases. Thus, the high speed optimum shape of the winglet in case without wingspan restriction can be considered as the optimum one.

Significant sign of this optimal shape of winglet is lower value of the tip-in angle, than that of toe-in angle, so the winglet is twisted oppositely as usual. Another significant sign is difference between the velocity magnitude at the winglet upper surface. Region with velocity peak mentioned in the subchapter 11.3 is smaller, but region with higher velocity has wider in the sense of the winglet span. This could be seen in the figure 11.7. This may be caused by the higher angle of attack of the winglet airfoils than in case of restricted wingspan high speed case.

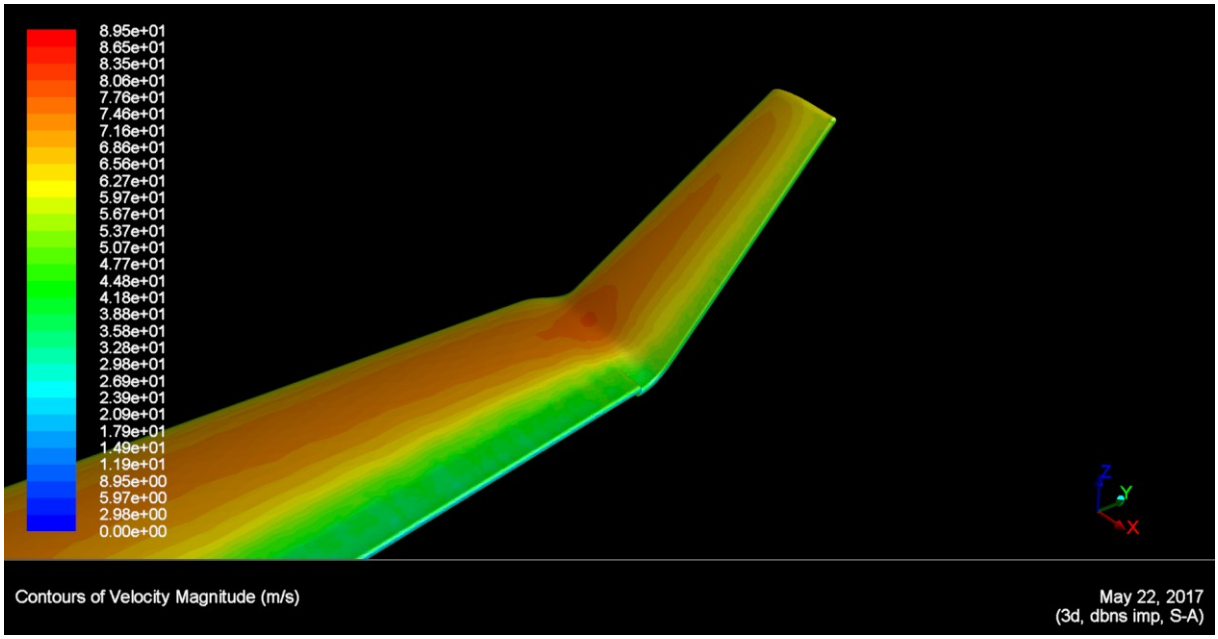

Fig. 11.7 Velocity magnitude in the region of wing to winglet junction for HS case

11.5 Overall evaluation

Detailed evaluations of each optimal design case are in the subchapter 11.1 through 11.4. However overall evaluation of the design cases from the performance point of view will clearly declare the improvements obtained by the optimisation. For this reason, lift to drag ratio and

third power of lift coefficient squared to the drag coefficient ratio parameters comparison to the reference case will be mentioned in the following table.

Flight regime	Design case	c_L/c_D [-]	$\Delta c_L/c_D$[-]	${c_L}^{3/2}/c_D$ [-]	$\Delta {c_L}^{3/2}/c_D$ [-]
Low speed	Reference	24,07937	-	29,68387	-
	LS, 15m	24,15323	0,07385	29,79117	0,10730
	LS (RUN 10)	24,30187	0,22249	30,02506	0,34118
High speed	Reference	17,84844	-	8,93102	-
	HS, 15m	17,86469	0,01625	8,94646	0,01544
	HS	17,99570	0,14727	9,05901	0,12800

Tab. 11.22 Overall comparison of aerodynamic performance parameters

From the table 11.12, picture of the performance gains of optimised cases against the reference ones can be clearly seen.

In the low speed flight regime, case optimised with wingspan restriction to 15m has glide ratio higher by 0,074. In the sailplane competitions, each tenth of the glide ratio improvement counts. Improvement in the field of effort to obtain minimum possible sink speed in LS,15m case, which is determined by ${c_L}^{3/2}/c_D$ is 0,107. Conclusion can be made, that target of optimisation process was met as the overall performance in the low speed flight was improved.

When LS no wingspan restricted case is considered, improvements is much higher, as the wingspan was increased. Gains are approximately three times higher than in case of restricted wingspan. However, when the competition flying is considered, the FAI 15m class sailplanes must not increase wingspan over the 15m during the competition. Despite that, results of the optimisation could be considered as the base for the investigations in the other aircraft segments. Large cant angles changes can be beneficious in the business jet segment, and also in the regional transport aircraft segment, where the benefits should be even higher.

In HS,15m case, the improvement of the winglet performance against the reference case is not high. However, improvement in the field of glide ratio with value 0,016 was obtained and the glide ratio at high speeds is crucial when it comes to high speed interthermal flight.

Case designed HS, which has no span restrictions, shows higher improvements. This time, the improvement in glide ratio is approximately 9 times higher than in case with restricted span. However, all conclusions made in the paragraph describing LS no wingspan restricted case is applicable also to the HS case.

12 CONCLUSION

Optimisation of Ventus 2ax sailplane winglet in multiple flight regimes and with multiple different design constrains was done during work on this master´s thesis.

Form the beginning, the work was focused on the study of feasibility of the winglet with ability to change its shape during the flight. Smooth winglet geometry change was considered. Because of that, winglet is not fitted with any flaps, or hinges which could worsen aerodynamic performance. Also wing to winglet junction region is considered of elastic material which change its shape as the winglet geometry changes.

Sailplane winglet was optimised for two different flight regimes separately, which means, that optimum shape for each regime was obtained. First flight regime considered was low speed flight regime in which the sailplane fly when gaining altitude. Characteristics of this flight regime were flight speed of 85 km/h and wing flap deflection to position +2 which corresponds to the flap angular deflection 7,172 degrees. Second flight regime was defined as high speed regime in which sailplane flies when performing interthermal glide. Characteristics of this regime was chosen as follows. Flight speed was defined to 210 km/h and flap deflection position was defined as -2 which corresponds to the angular value of deflection -8,609 degrees.

Winglet was optimised in each flight regime two times. First optimisation was done for the geometry constrain of maximum allowed wingspan including winglet of 15m. Second optimisation was done for wing with no wingspan restrictions, so the winglet cant angle may be considerably changed even to the high positive cant angle values.

For optimisation process, the Response Surface Method was chosen, as it allows to perform the optimisation with lesser number of CFD simulations of different design cases to obtain optimum solution, than some other methods like the genetic algorithm method for example.

Optimisation was done with all data obtained from CFD simulations and no in-flight measurements were made. CFD simulations were performed using fully turbulent model. because of its relatively low computational requirements. Decision to use fully turbulent Spallarat-Almaras model was taken also because of the number of CFD simulations, which had to be done to obtain sufficiently large database of design points for appropriate approximation of the response surface shape. Totally 30 design variants were simulated during CFD processing, another five CFD simulations were done during mesh dependency study. And finally, four simulations were performed during evaluation of the optimised shapes of winglets. Total count of simulations was 39. Simulation computation time was 13 hours in average when simulations were performed using 7 nodes of Chronos computational cluster of Institute of Aerospace Engineering at Brno University of Technology. Each node consists of 12 processors. Total CFD simulations computation time was approximately 500 hours.

After evaluation of the optimised winglet geometries, three of four was considered as the optimums, but in one optimisation, the process failed due to insufficient fit of the response surface model determined by multiple linear regression. Causes of the process failure are described in the chapter 11.2. Best performing design was substituted for the optimal in this case. Namely, failure occurs in the low speed flight regime case optimisation with no wingspan restrictions.

When the improvements gained by the winglet shape changes should be considered, reference winglet performance was overcame in all four optimisation cases. Gains in the low speed flight regime with span restriction are much higher than in case of high speed one. This is caused by higher intensity of the tip flow in high angle of attack low speed flight. During the

low speed flight, absolute values of toe-in and tip-in angles are higher than in the high speed flight regime, when the optimal winglet geometries are considered. In the high speed flight, the winglet has tendency to minimise its drag by lowering the toe-in and tip-in angles in absolute values. All above mentioned is documented in chapter 11.

Considering the absolute values, the increase of the flight performance in low speed flight regime is small, but not negligible as the sailplane type of aircraft is high performance sport aircraft type for competition use. Increase of flight performance in the high speed flight regime is also small, but useful in the competition flying.

The conclusion can be made, that morphing winglet application on the high performance sailplane will be beneficious. But only in case, that sufficient advantage would be made to the materials which could be applied to the morphing winglet structure and in case of invention of simple, relatively cheap and efficient system of winglet shape control during the flight. First consideration points towards some type of electric distributed control system consisting of control unit and small electric servomotors, which allows the winglet to change its shape depending on the wing flap position.

BIBLIOGRAPHY

[1] DANĚK, Vladimír. *Mechanika letu I: letové výkony.* Vydání první. Brno: Akademické nakladatelství CERM, 2009. 293 p. ISBN 978-80-7204-659-1.

[2] FREESTONE, M. *IHS ESDU 98013: Aerodynamic principles of winglet.* 2003. 61 p. ISBN 978-1-86246-050-8.

[3] HOUGHTON, E.L., CARPENTER, P.W. *Aerodynamics for Engineering Students.* 5th edition. Oxford: Buttenrworth-Heinemann, 2003. 614 p. ISBN 0-7506-5111-3.

[4] KEANE, Andy J., NAIR, Prashant B. *Computational Approaches for Aerospace Design: The Pursuit of Excellence.* Chichester: John Wiley & Sons Ltd. 2005. 582 p. ISBN-13-978-0-470-85540-9.

[5] THOMAS, Fred. *Fundamentals of Sailplane Design.* 3rd edition. Collage Park: Collage Park Press, 1999. 286 p. ISBN 987-0966955309.

[6] POPELA, Robert, ZIKMUND, Pavel. *LU44-2007-001.AD: Aerodynamický návrh wingletu pro letoun VUT 001 Marabu.* Brno: Vysoké Učení Technické v Brně, Fakulta Strojního Inženýrství, Letecký Ústav, 2007. 23 p.

[7] POPELKA, L. *Disertační Práce: Aerodynamická optimalizace leteckých profilů pro větroně.* Praha: České Vysoké Učení Technické v Praze, 2006. 166 p.

[8] HANSESN, Thomas. Modeling the Performance of Standard Cirrus Glider using Navier-Stokes CFD. *Technical Soaring: Vol 38, No.1* [online]. Published: 2014, [cit. 2015-04-18]. Available from WWW: <http://journals.sfu.ca/ts/index.php/ts/article/view/502>

[9] MAUGHMER, Mark D.*, The Design Of Winglets for Low-Speed Aircraft* [online]. 2012-08-30 [cit. 2017-05-24]. 18 p. (PDF). Available from WWW: <http://www.mandhsoaring.com/why%20winglets/wl-it.pdf>.

[10] TATSYUKI, Amago. *Sizing Optimization Using Response Surface Method in FOA* [online]. 2012-08-30 [cit. 2017-05-24]. 7 p. (PDF). Available from WWW: <http://www.tytlabs.com/english/review/rev371epdf/e371_031amago.pdf>.

[11] *Certification Specification for Sailplanes and Powered Sailplanes: CS-22* [online]. 2009-05-30 [cit. 2017-05-24]. 121 p. (PDF). Available from WWW: https://www.easa.europa.eu/system/files/dfu/Consolidated%20version%20CS-22%20Amdt%202.pdf>.

[12] *Create Mesh Density* [online]. 2017 [cit. 2017-05-24]. Available from WWW: < https://www.sharcnet.ca/Software/Ansys/15.0.7/en-us/help/icm_help/imesh_createdensity.html>.

[13] *Dimensionless wall distance (y plus) -- CFD-Wiki, the free CFD reference* [online]. 2017 [cit. 2014-03-28]. Available from WWW: < https://www.cfd-online.com/Wiki/Dimensionless_wall_distance_(y_plus)>.

[14] *Engineering Statistic Handbook: 5.3.3.6.1. Central Composite Designs (CCD)* [online]. 2013-10-30 [cit. 2017-05-24]. Available from WWW: <http://www.itl.nist.gov/div898/handbook/pri/section3/pri3361.htm>.

[15] *European Patent Application EP 2 881 322 A2* [online]. 2014-12-04 [cit. 2017-05-24]. 27 p. (PDF). Available from WWW: < https://patentimages.storage.googleapis.com/pdfs/2607c5ce9b7e73f79b34/DOCUMENT.PDF>.

[16] *European Patent Application EP 2 233 395 A1* [online]. 2009-03-24 [cit. 2017-05-24]. 27 p. (PDF). Available from WWW: < https://docs.google.com/viewer?url=patentimages.storage.googleapis.com/pdfs/7d609855814f829b5c3d/EP2233395A1.pdf>.

[17] *FACC presents latest winglet technology - News & Press Archive - News - FACC* [online]. 2015-10-02 [cit. 2017-05-24]. Available from WWW: < http://www.facc.com/en/News/News-Press-Archive/FACC-presents-latest-winglet-technology>.

[18] *FLUENT 6.3 User's Guide - 7.2.2 Determining Turbulence Parameters* [online]. 2006-09-20 [cit. 2017-04-25]. Available from WWW: < https://www.sharcnet.ca/Software/Fluent6/html/ug/node217.htm>.

[19] *FLUENT 6.3 User's Guide - 8.14.2 Operating Pressure, Gauge Pressure, and Absolute Pressure* [online]. 2006-09-20 [cit. 2017-05-20]. Available from WWW: < https://www.sharcnet.ca/Software/Fluent6/html/ug/node373.htm>.

[20] *Friction velocity -- CFD-Wiki, the free CFD reference* [online]. 2008-12-19 [cit. 2017-09-20]. Available from WWW: <https://www.cfd-online.com/Wiki/Friction_velocity>.

[21] *SCHEMPP-HIRTH Flugzeugbau GmbH: Ventus-2ax/2bx* [online]. 2017 [cit. 2017-05-24]. Available from WWW: < https://www.schempp-hirth.com/en/sailplanes/ventus-2/ventus-2ax2bx.html>.

[22] *United States Patent US 7,744,038 B2* [online]. 2010-06-29 [cit. 2017-05-24]. 14 p. (PDF). Available from WWW: < https://www.google.si/patents/US7744038>.

[23] *Y+ Calculator - Compute Wall Spacing for CFD* [online]. 2017 [cit. 2017-05-24]. Available from WWW: < http://www.pointwise.com/yplus/>.

LIST OF FIGURES

LIST OF TABLES

LIST OF SYMBOLS AND ACRONYMS

Symbol	Description	Unit
a	Speed of sound	$m \cdot s^{-1}$
AR_W	Wing aspect ratio	-
a_w	Winglet lift curve slope	rad^{-1}
b	Wingspan without winglets	m
b_a	Wingspan with winglets	m
b_s	Structural wingspan	m
b_i	Coefficient of regression function	-
CCC	Circumscribed	-
CCF	Face centered	-
CCI	Inscribed	-
c_{Dp}	Pressure drag coefficient	-
c_{Dv}	Viscous drag coefficient	-
C_{Lmax}	Maximum lift coefficient of winglet profile	-
c_{MAC}	Mean aerodynamic chord length	mm
c_t	Wing tip chord	mm
c_{wr}	Winglet root chord	mm
c_{wt}	Winglet tip chord	mm
D_{oa}	Trailing vortex drag (with winglet)	N
D_{ob}	Trailing vortex drag (without winglet)	N
DoE	Design of experiments	-
D_{TV}	Trailing vortex drag	N
D_w	Winglet drag	N
F	Cost function value	-
f_i	Parameter i function value	-
g	Acceleration of gravity	$m \cdot s^{-2}$
G	Actual aircraft weight	kg
h_w	Winglet height	mm
I	Turbulence intensity	-
k	Gust alleviation factor	-
K	Glide ratio	-
L	Wing lift	N
l_w	Winglet span	mm
L_w	Winglet lift	N
L_{Wm}	Loft of winglet due to sideslip at V_A	N

M	Mach number	-
MAC	Mean aerodynamic chord	-
M_r	Bending moment in symmetry plane of wing	Nm
p_{abs}	Absolute pressure	Pa
p_{gauge}	Gauge pressure	Pa
p_{op}	Operating pressure	Pa
q	Dynamic pressure	Pa
R_{domain}	Domain radius	Mm
Re	Reynolds number	-
R^2	Coefficient of determination	-
R^2_{adj}	Adjusted coefficient of determination	-
RSM	Response surface method	-
s	Semi span without winglet	m
s_a	Semi span with winglet	m
SMA	Shape memory alloy	-
S_W	Wing area	m^2
S_{WL}	Winglet area	m^2
T	Winglet thrust force	N
U	Lateral gust speed	$m \cdot s^{-1}$
u'	Fluctuations velocity	$m \cdot s^{-1}$
u_*	Friction velocity	$m \cdot s^{-1}$
u_{avg}	Mean flow velocity	$m \cdot s^{-1}$
V	Speed	$m \cdot s^{-1}$
V_A	Design manoeuvring speed	$m \cdot s^{-1}$
V_B	Design gust speed	$m \cdot s^{-1}$
V_D	Design dive speed	$m \cdot s^{-1}$
V_{sc}	Speed of descent	$m \cdot s^{-1}$
V_w	Velocity of winglet oncoming flow	$m \cdot s^{-1}$
W/S	Wing loading	$kg \cdot m^{-2}$
W_E	Empty weight	kg
w_i	Weight of parameter i	-
w_{min}	Minimum speed of descent	$m \cdot s^{-1}$
W_{TO}	Maximum take-off weight	kg
W_{WB}	Max water ballast weight	kg
Xi	Coded variable	-
x_{MAC}	Mean aerodynamic chord L.E. x coordinate	mm

Y^+	Dimensionless wall distance	-
y_b	Effective bending moment arm	m
y_{MAC}	Mean aerodynamic chord L.E. y coordinate	mm
z_{MAC}	Mean aerodynamic chord L.E. z coordinate	mm
α	Angle of attack	°
β_i	Response surface function coefficient	-
γ_{wlt}	Winglet twist	°
γ_{wr}	Toe-in angle	°
γ_{wt}	Tip-in angle	°
$\bar{\gamma}_{min}$	Minimum glide angle	°
ε	Residual value	-
η_b	Non-dimensional bending moment arm	-
Λ_{TE}	Sweep angle (at T.E.)	°
ρ_0	Air density at sea level (ISA)	$kg \cdot m^{-3}$
Φ	Cant angle	°
ξ_i	Natural variable	°
τ_w	Wall shear stress	Pa
$\mathbf{V}$	Matrix of variations	-
v	Number of variations	-
ν	Kinematic viscosity	Pa·s

LIST OF APPENDICES

APPENDICES

A.1 3 view drawing of Ventus 2ax sailplane

Fig. A1.1 Ventus 2ax sailplane 3 view drawing (next page)

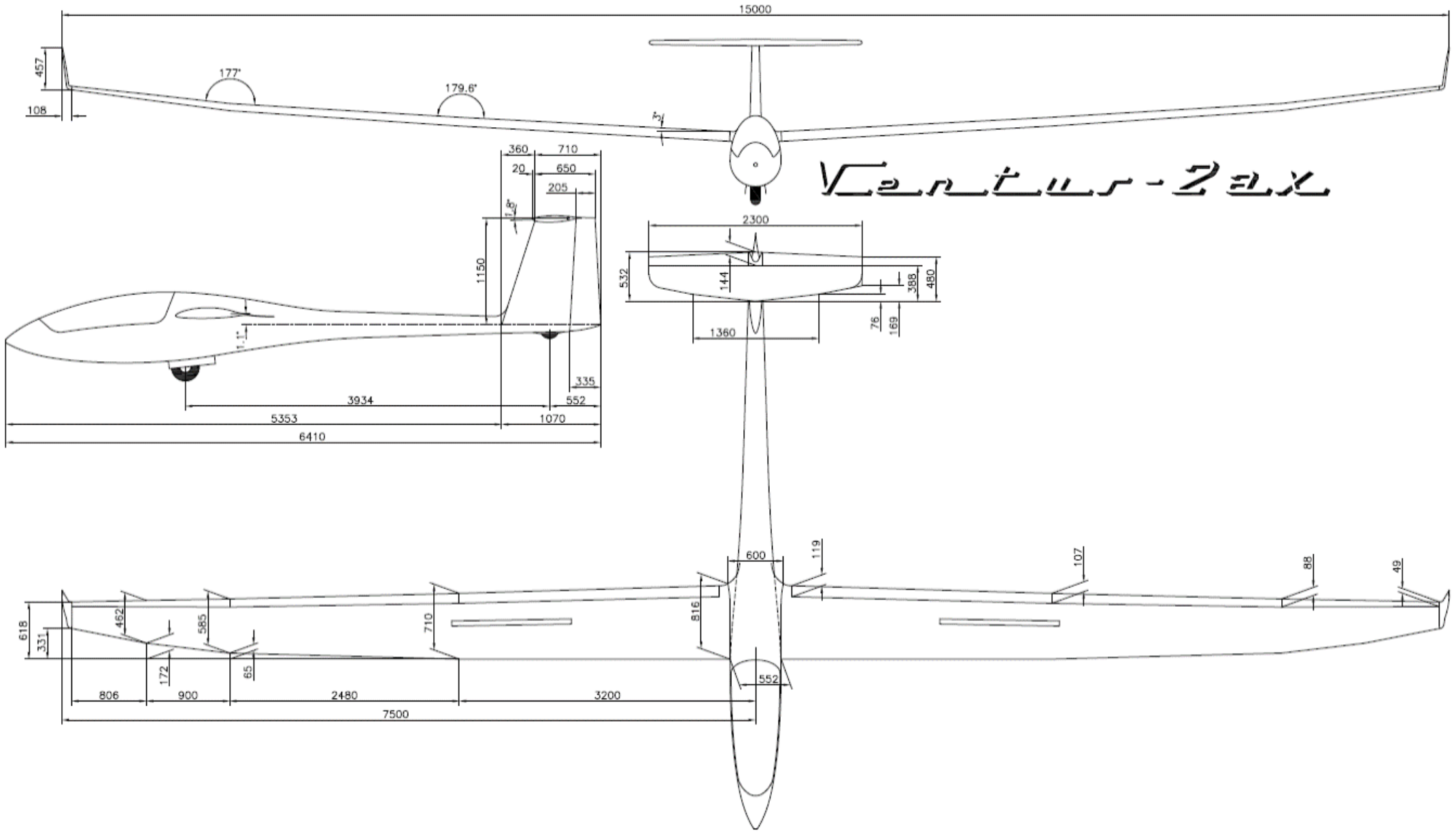
15000
457
108
177°
179,6°
Ventus-2ax
360
710
20
650
205
1150
335
3934
552
5353
1070
6410
2300
532
144
388
480
76
169
1360
600
119
107
88
49
816
618
331
462
585
710
172
65
552
806
900
2480
3200
7500

A.2 Comparison of individual DoE cases to the reference case

LOW SPEED FLIGHT CASES (85 km/h, FLAP +2)					
RUN	ΔC_D	ΔC_L	ΔC_m	$\Delta C_L/C_D$	$\Delta {C_L}^{3/2}/C_D$
	[%]	[%]	[%]	[%]	[%]
1	0,09217	0,51889	1,59568	0,42633	0,68655
2	-0,20522	0,41210	1,27278	0,61859	0,82570
3	-0,19257	0,31762	1,10915	0,51117	0,67067
4	-0,36307	0,24551	0,75015	0,61080	0,73423
5	0,71117	0,08154	-0,81413	-0,62518	-0,58468
6	0,54779	-0,04544	-0,85488	-0,59000	-0,61259
7	0,29104	-0,59906	-1,62751	-0,88751	-1,18483
8	0,43840	-0,69410	-1,72031	-1,12756	-1,47130
9	0,00000	0,00000	0,00000	0,00000	0,00000
10	-0,47247	0,44716	1,82354	0,92400	1,14939
11	0,58802	-0,70028	-2,45473	-1,28077	-1,62703
12	0,43987	0,31364	0,18589	-0,12568	0,03082
13	-0,01671	0,07892	-0,18350	0,09565	0,13514
14	0,20773	0,23408	0,39549	0,02630	0,14331
15	0,20339	0,16592	0,16313	-0,03739	0,04550
HIGH SPEED FLIGHT CASES (210 km/h, FLAP -2)					
RUN	ΔC_D	ΔC_L	ΔC_m	$\Delta C_L/C_D$	$\Delta {C_L}^{3/2}/C_D$
	[%]	[%]	[%]	[%]	[%]
1	1,06602	1,45644	2,69549	0,38631	1,11470
2	0,50320	0,94783	1,83321	0,44240	0,91729
3	-0,00996	-0,29084	-0,12278	-0,28091	-0,42603
4	-0,03361	-0,79035	-1,11482	-0,75699	-1,14995
5	1,24454	0,57736	0,04210	-0,65897	-0,37261
6	1,30873	0,00717	-0,15773	-1,28475	-1,28121
7	0,09291	-0,74271	-1,51337	-0,83484	-1,20378
8	-0,00811	-0,98926	-1,91266	-0,98122	-1,47222
9	0,00000	0,00000	0,00000	0,00000	0,00000
10	-0,03405	0,54165	1,48871	0,57590	0,84792
11	0,28895	-0,45213	-1,47937	-0,73894	-0,96359
12	2,58893	2,01976	2,70018	-0,55480	0,44446
13	0,08643	-1,27429	-2,09824	-1,35954	-1,99004
14	1,62927	1,06348	1,36334	-0,55672	-0,02933
15	1,02638	0,30482	0,20661	-0,71424	-0,56303

Tab.A2.1 Comparison of individual DoE cases to the reference one

A.3 Graphic form of optimised cases to the reference case comparison

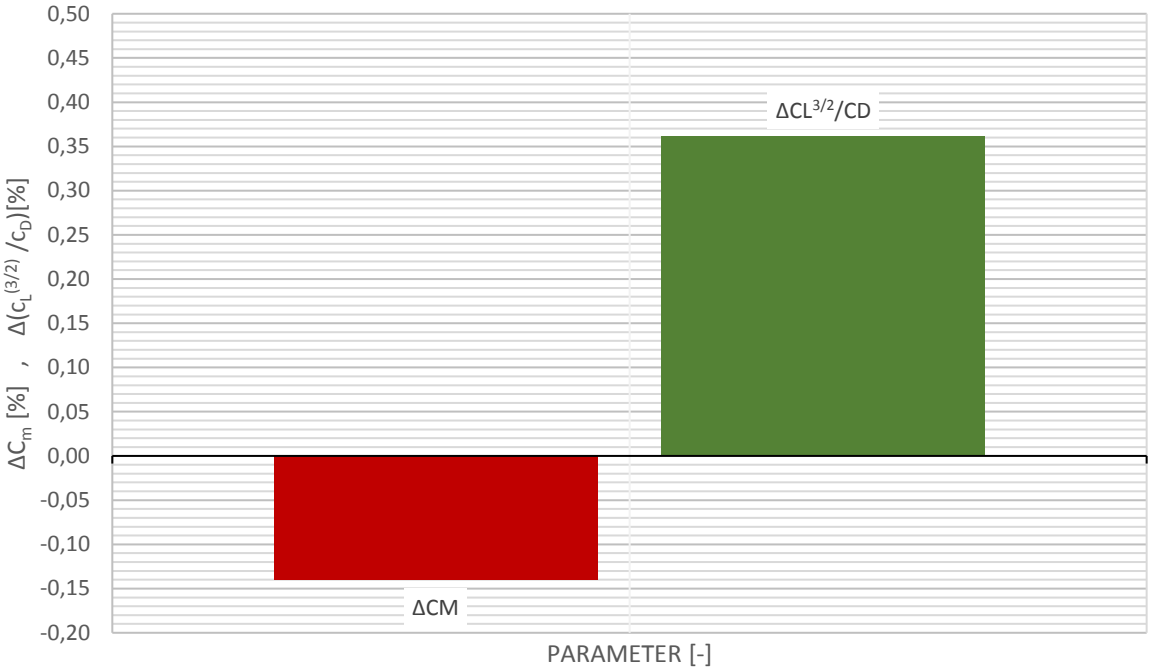

Fig. A3.1 Gains of the LS,15m optimal case

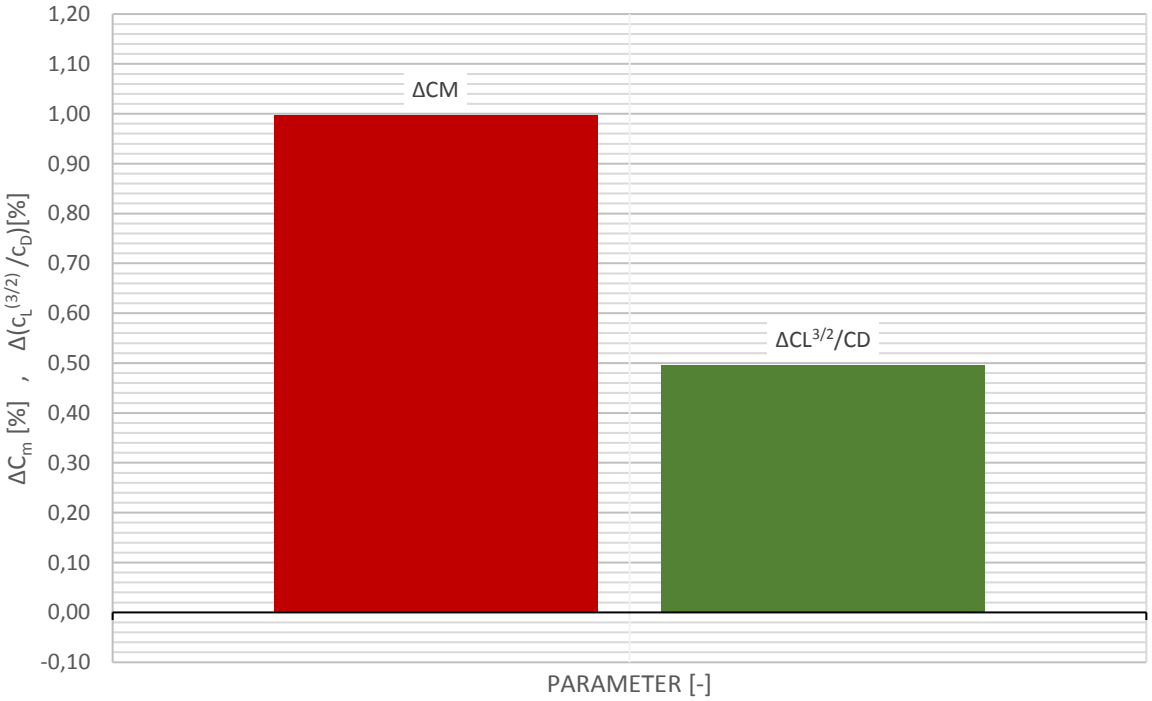

Fig. A3.2 Gains of the LS optimal case

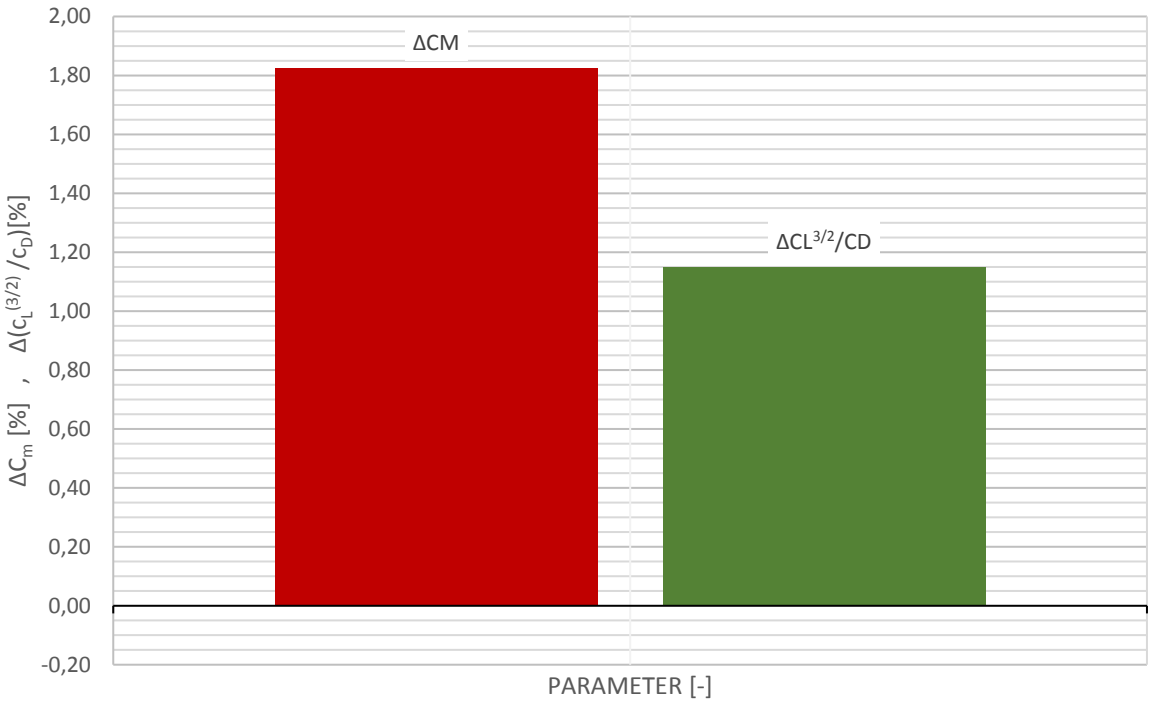

Fig. A3.3 Gains of the RUN 10 low speed case

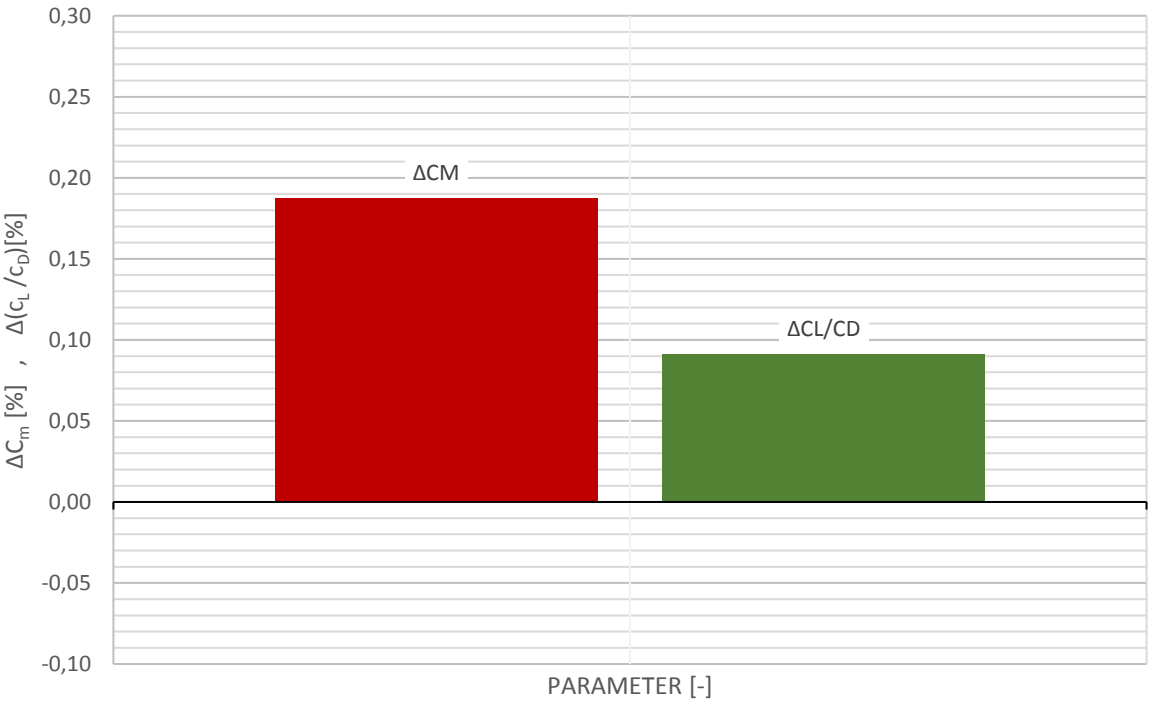

Fig. A3.4 Gains of the HS,15m case

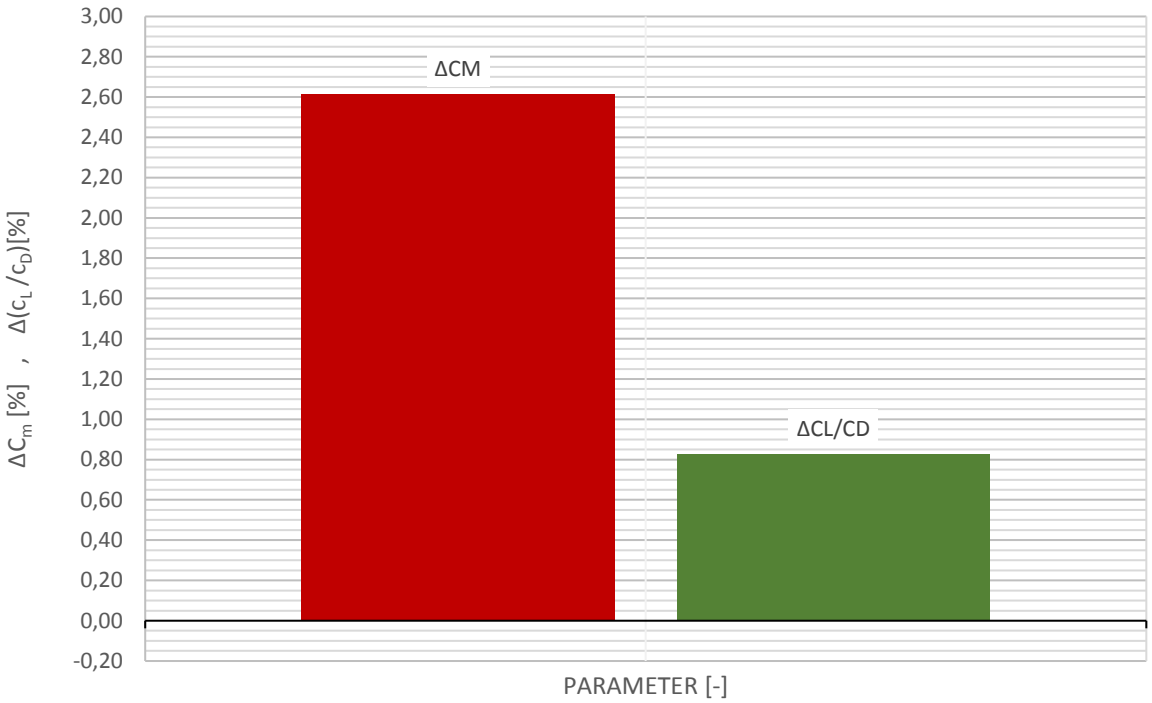

Fig. A3.5 Gains of the HS case

A.4 CFD simulations visualisations

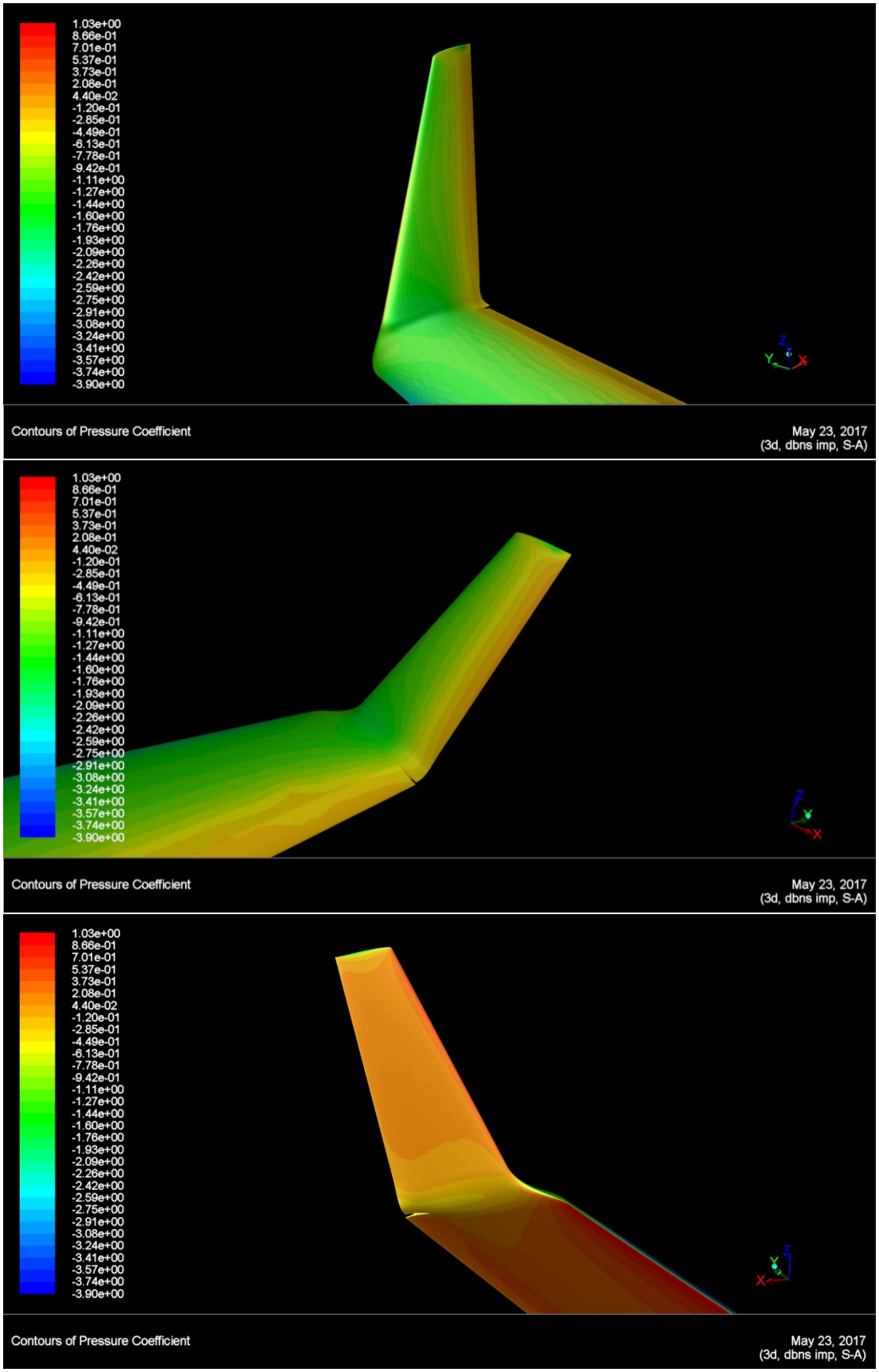

Fig. A4.1 Pressure coefficient contour plots for LS,15m case

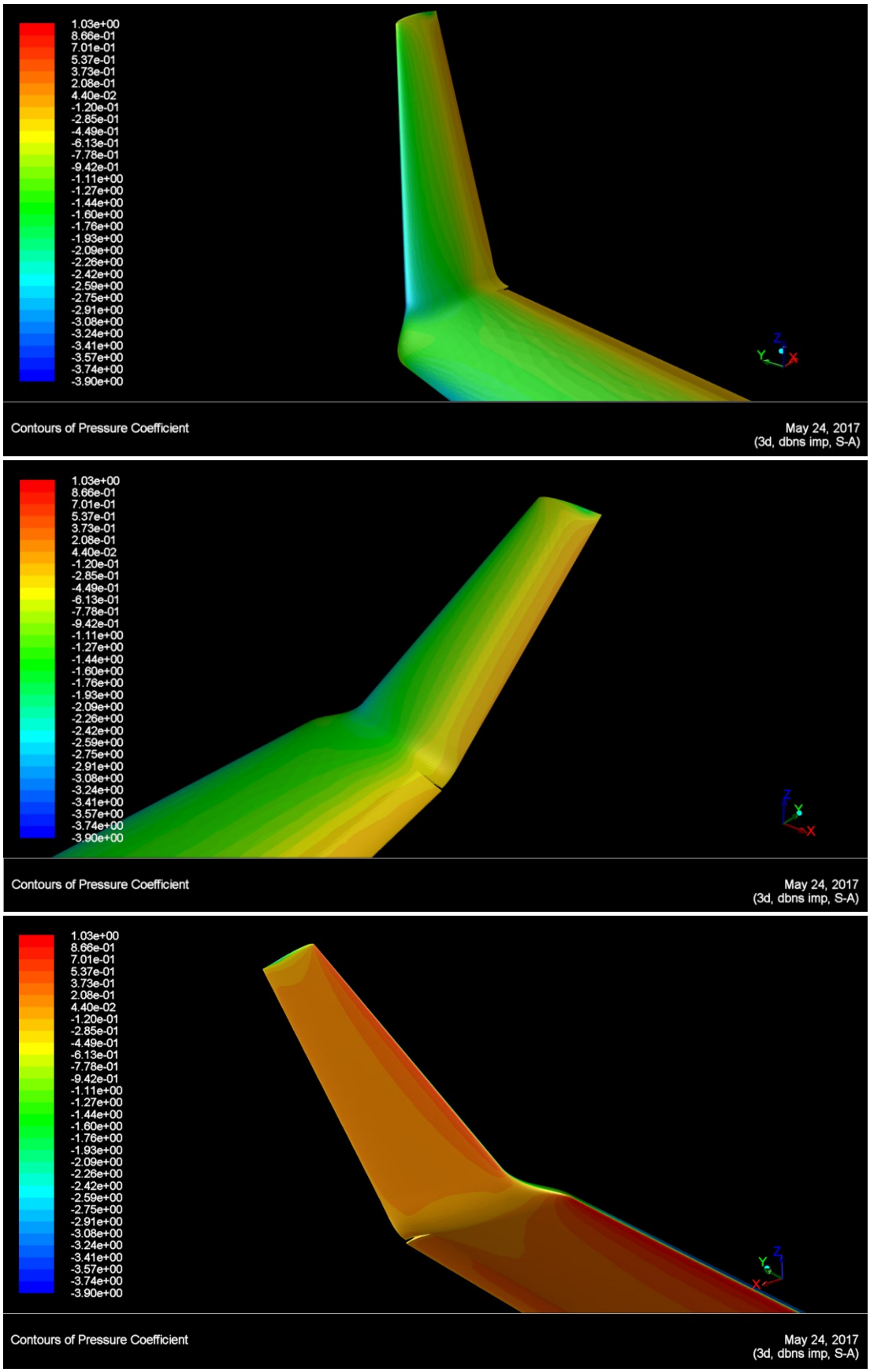

Fig. A4.2 Pressure coefficient contour plots for LS, RUN 10 case

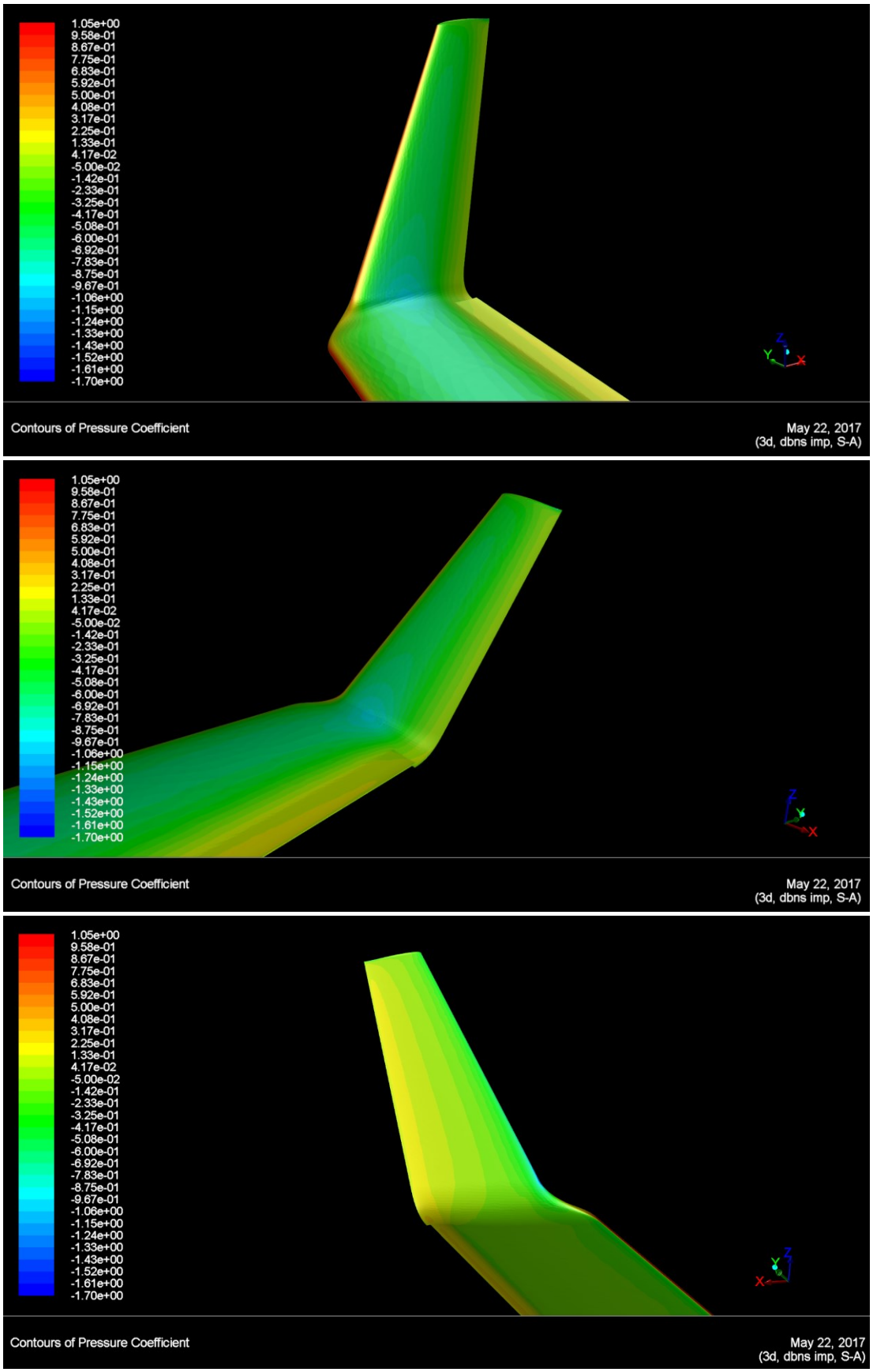

Fig. A4.3 Pressure coefficient contour plots for HS,15m case

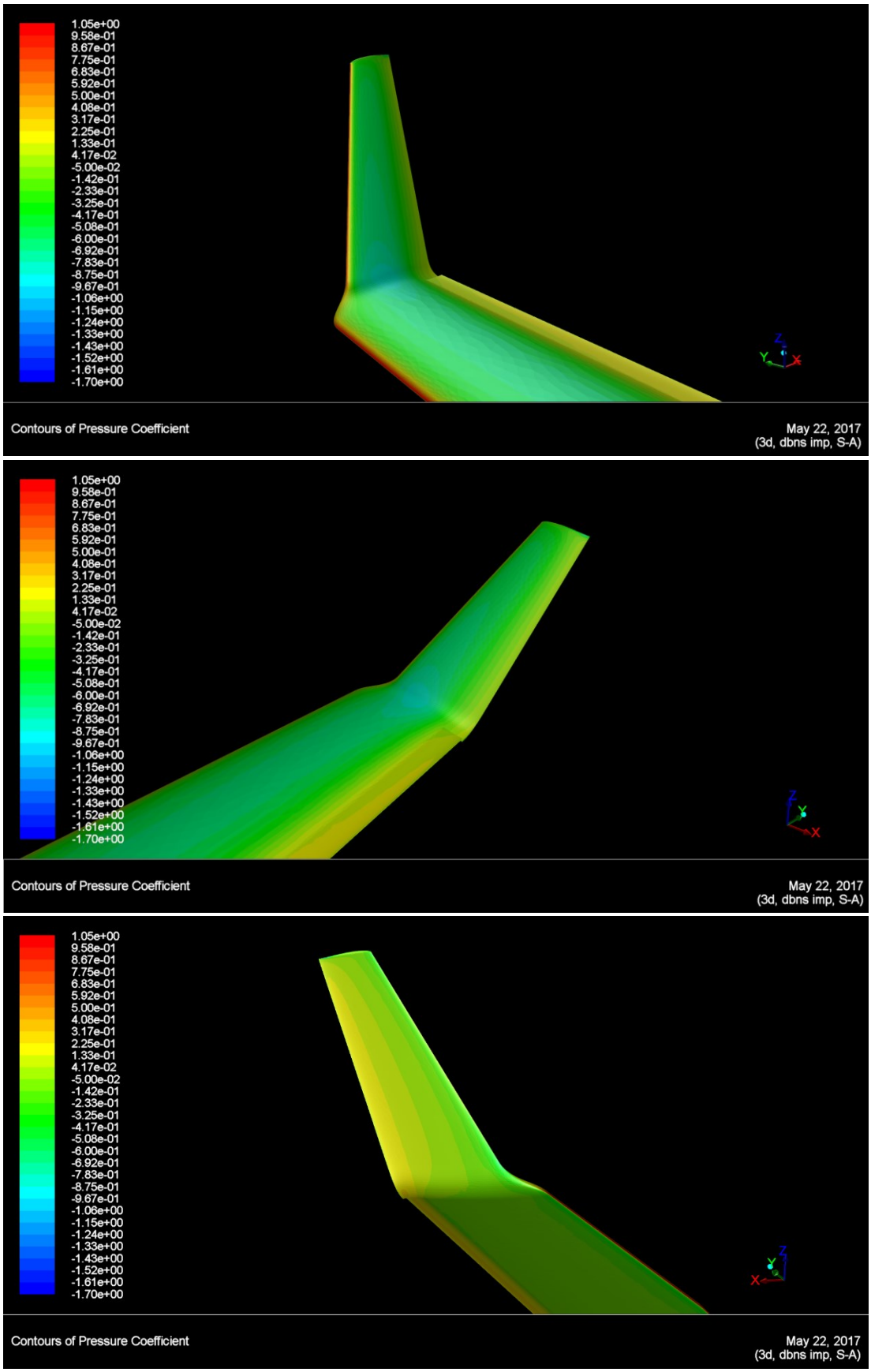

Fig. A4.4 Pressure coefficient contour plots for HS case

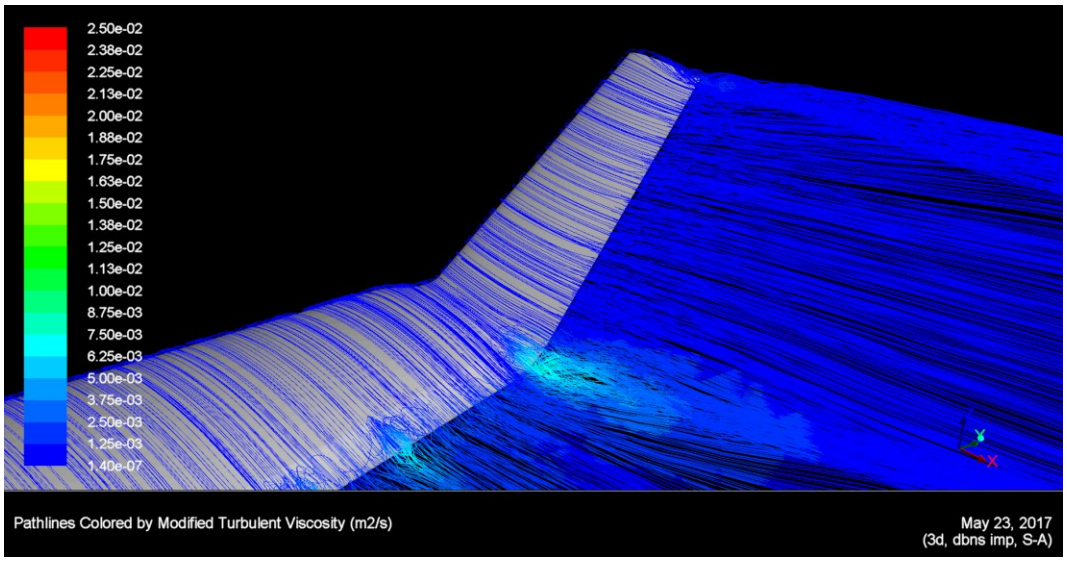

Fig. A4.5 Flow visualisation of LS reference case

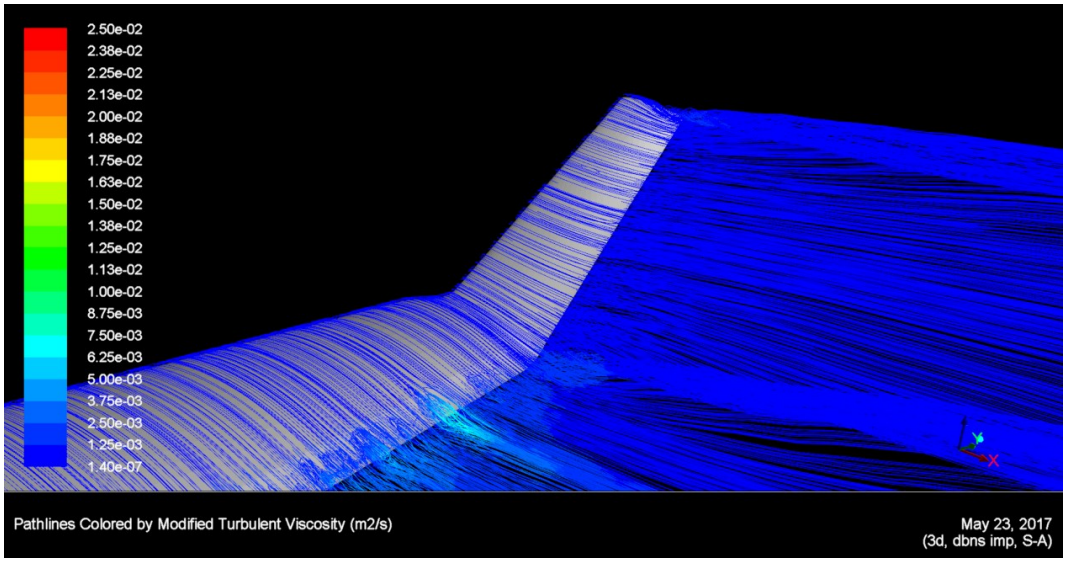

Fig. A4.6 Flow visualisation of LS, 15m case

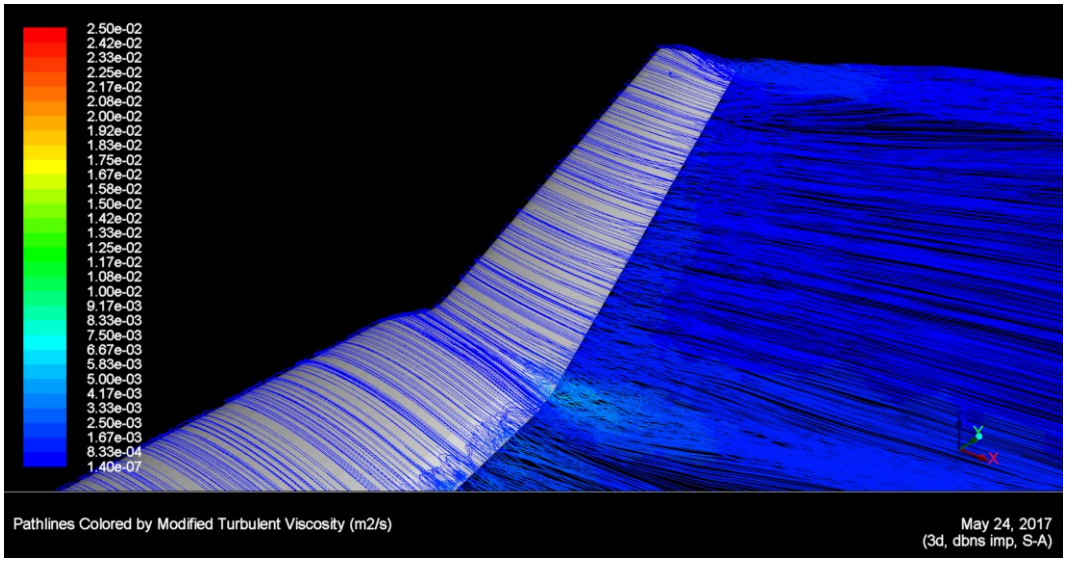

Fig. A4.7 Flow visualisation of LS, RUN 10 case

A.5 Contents of CD with electronic form of master's thesis

1) PDF version of master's thesis

2) CAD models of individual winglet designs

3) XLS file containing results of simulations

4) MATLAB script files